1. Report No. ATC-173	2. Government Accession No. DOT/FAA/NR-90/3	3. Recipient's Catalog No.

4. Title and Subtitle	5. Report Date
Contributions to the American Meteorological Society 16th Conference on Severe Local Storms	15 August 1990
	6. Performing Organization Code

7. Author(s)	8. Performing Organization Report No.
Lincoln Laboratory Weather Sensing Group	ATC-173

9. Performing Organization Name and Address	10. Work Unit No. (TRAIS)
Lincoln Laboratory, MIT P.O. Box 73 Lexington, MA 02173-9108	
	11. Contract or Grant No. DTFA-01-L-83-4-10579
	13. Type of Report and Period Covered

12. Sponsoring Agency Name and Address	
Department of Transportation Federal Aviation Administration Systems Research and Development Service Washington, DC 20591	Project Report
	14. Sponsoring Agency Code

16. Abstract

Eight papers contributed by the Lincoln Laboratory Weather Sensing Group to the American Meteorological Society's 16th Conference on Severe Local Storms, to be held October 22-26, 1990 in Kananaskis Provincial Park, Alberta, Canada, are compiled in this volume. The FAA sponsored the summer 1989 field test of the Terminal Doppler Weather Radar (TDWR) system in Kansas City, Missouri to detect wind shear aviation hazards at or near the airport. The papers are based on data collected through the summer 1989 field test and on subsequent analyses and product evaluation.

The staff members of Group 43, Weather Sensing, have documented their studies of the following topics: a severe microburst; a prototype microburst prediction product; average summer microburst threat prediction at an airport; microburst asymmetry; the effect of radar viewing angle on the performance of the gust front detection algorithm; a comparison of Low-Level Wind Shear Alert System (LLWAS) anemometer-measured winds and Doppler-measured winds; and ASR-9 (Airport Surveillance Radar) adjustment of range-dependent storm reflectivity levels. The final paper is an invited paper for the Conference on microbursts. This paper discusses the precipitation-driven downdraft and the downdraft associated with the "vortex," or gust front, at the leading edge of an expanding thunderstorm outflow as two primary forms of low altitude downdraft phenomena in the microburst problem.

17. Key Words		18. Distribution Statement
Terminal Doppler Weather Radar (TDWR) automatic low altitude wind shear detection numerical thunderstorm outflow model Air Surveillance Radar-9 (ASR-9) microburst	fan-beam radar thunderstorm da. gust front LLWAS – TDWR integration vertical reflectivity profiles	Document is available to the public through the National Technical Information Service, Springfield, VA 22161.

19. Security Classif. (of this report)	20. Security Classif. (of this page)	21. No. of Pages	22. Price
Unclassified	Unclassified	56	

FORM DOT F 1700.7 (8-72)   Reproduction of completed page authorized

ABSTRACT

Eight papers contributed by the Lincoln Laboratory Weather Sensing Group to the American Meteorological Society's 16th Conference on Severe Local Storms, to be held October 22-26, 1990 in Kananaskis Provincial Park, Alberta, Canada, are compiled in this volume. The FAA sponsored the summer 1989 field test of the Terminal Doppler Weather Radar (TDWR) system in Kansas City, Missouri to detect wind shear aviation hazards at or near the airport. The papers are based on data collected through the summer 1989 field test and on subsequent analyses and product evaluation.

The staff members of Group 43, Weather Sensing, have documented their studies of the following topics: a severe microburst; a prototype microburst prediction product; average summer microburst threat prediction at an airport; microburst asymmetry; the effect of radar viewing angle on the performance of the gust front detection algorithm; a comparison of Low-Level Wind Shear Alert System (LLWAS) anemometer-measured winds and Doppler-measured winds; and ASR-9 (Airport Surveillance Radar) adjustment of range-dependent storm reflectivity levels. The final paper is an invited paper for the Conference on microbursts. This paper discusses the precipitation-driven downdraft and the downdraft associated with the "vortex," or gust front, at the leading edge of an expanding thunderstorm outflow as two primary forms of low altitude downdraft phenomena in the microburst problem.

CONTENTS

A CASE STUDY OF THE CLAYCOMO, MISSOURI MICROBURST
ON JULY 30, 1989 [*]

Paul J. Biron, Mark A. Isaminger, Kevin J. Flemming
M.I.T. Lincoln Laboratory
Lexington, Massachusetts 02173

Alan A. Borho
University of North Dakota, Center for Aerospace Sciences
Grand Forks, North Dakota 58202

1. INTRODUCTION

The Terminal Doppler Weather Radar (TDWR) testbed collected thunderstorm measurements in the Kansas City area from March 27 through October 6, 1989. Of the 393 microbursts detected by the radar, 21 were classified as severe, with a differential velocity > 24 m/s. None of the severe events impacted terminal operations at Kansas City International Airport (KCI). Nevertheless, there were 42 microbursts within 3 nautical miles of the airport.
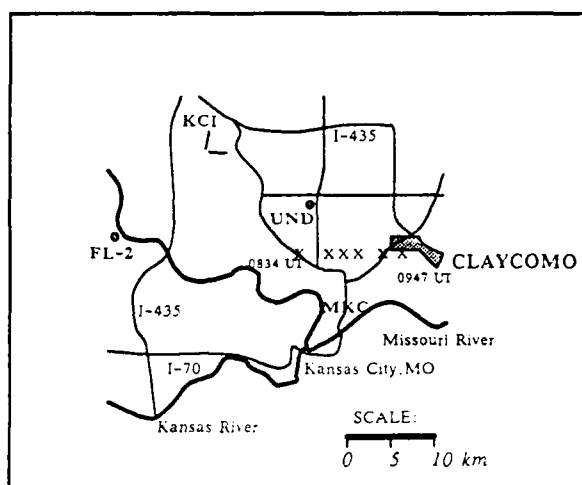

Figure 1. Map of the Kansas City area showing the track (x) of the Claycomo microburst producing cell in 15 minute intervals.

2. CASE STUDY

In this paper, a microburst that occurred on July 30, 1989 near Claycomo, Missouri (see Figure 1) will be examined. The outflow damaged trailers and uprooted trees in the area. Winds in excess of 55 mph, pea-sized hail, and 3 1/2 inches of rain accompanied the storm. This was the strongest microburst observed during the 1989 data collection season in Kansas City.

On July 30, microburst outflows were first detected northwest of the downtown airport (MKC) at 0709 UT and east of the University of North Dakota (UND) radar at

0806 UT. The echo which produced the Claycomo microburst developed at 0820 UT in the vicinity of the earlier outflows. It attained a maximum storm top height in excess of 15 km AGL.

2.1. Radar Data

Figure 2 is a radial velocity plot from FL-2 at the time of the maximum outflow. The wind shear is centered 29 km and 91° azimuth from the radar (A).
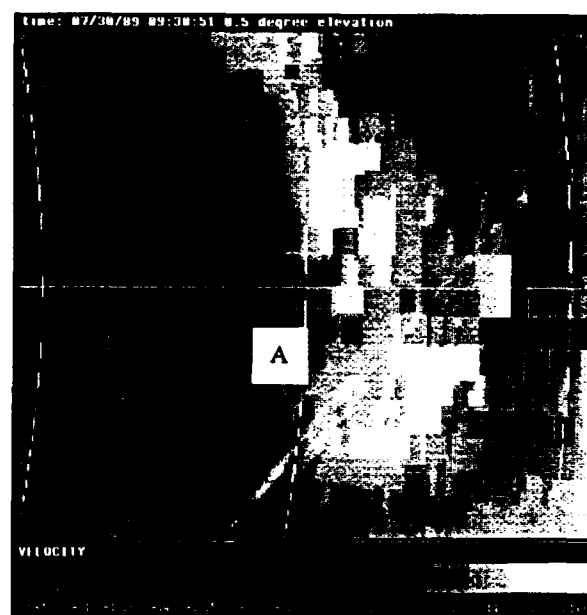
Figure 2. FL-2 radar velocity plot at 09:30:51 UT, the time of maximum outflow strength. Range rings are labelled in km.

Figure 3 is a synthesized vertical cross section plot (RHI) of the storm cell for velocity. This RHI was generated along the 91.5° azimuth and shows the maximum outflow (A in figure 3) and vertical structure of the storm. Convergence can be seen at approximately 2 km above the surface (B in figure 3). The RHI was created from available PPI data using scans ranging from 0.4° to 39.9° elevation. Gaps between consecutive tilts were then filled using a Cressman weighting interpolation technique.

1

Figure 3. FL-2 radar velocity vertical cross section along 91.5 de-
grees at 09:31:57 showing the maximum outflow. Grid lines indi-
cate height and range from FL-2 in km.

The microburst persisted for approximately 1 hour,
with a peak differential velocity observed by FL-2 of 38 m/s
over 4 km at 300 meters above ground level (AGL). A radial
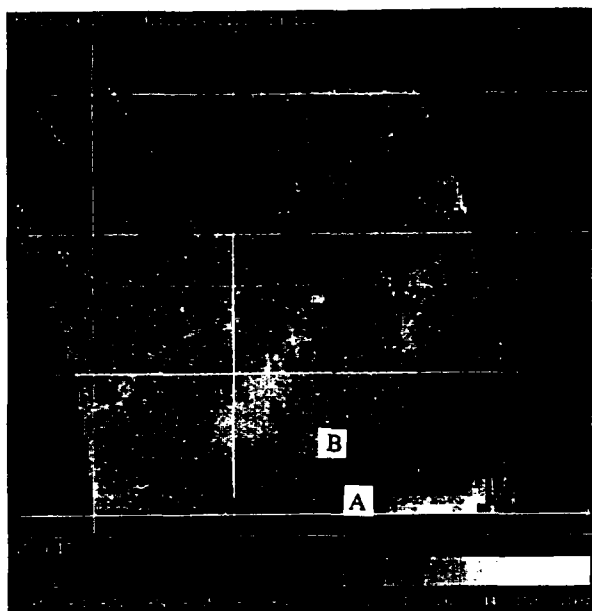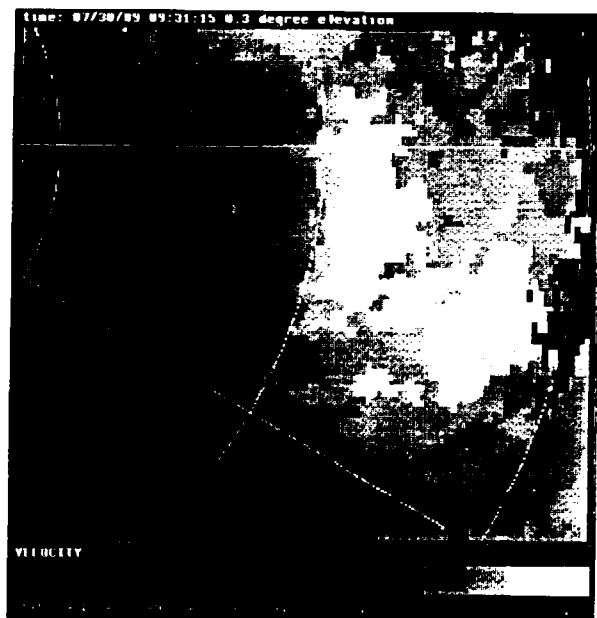velocity plot from UND at 0931 UT (Figure 4) suggests that

Figure 4. UND radar velocity plot showing the maximum outflow
strength at 70 m AGL. Range rings are labelled in km.

the outflow was stronger at lower levels since UND recorded
a peak differential velocity of 45 m s over 3 km at a height
of 70 meters AGL. The peak shear was observed on the firs'
available surface scan from UND

2.2. Microburst Features

Figures 5a and 5b present a summary of the velocity
features aloft and reflectivity features observed by the FL-2
radar throughout the life cycle of the microburst. These
features were manually extracted from the radar data to cor-
respond with those expected as microburst precursors by
the automated TDWR microburst detection algorithm
(Campbell 1989). The initial time of the microburst outflow
is represented by T = 0. The microburst reached its peak
velocity differential of 38 m s at T + 42 minutes (indicated
by the heavy vertical line in each plot). Upper level diver-
gence first occurred at T - 15 minutes and reached a peak
intensity of 25 m s at T + 37.5 minutes. Anticyclonic rota-
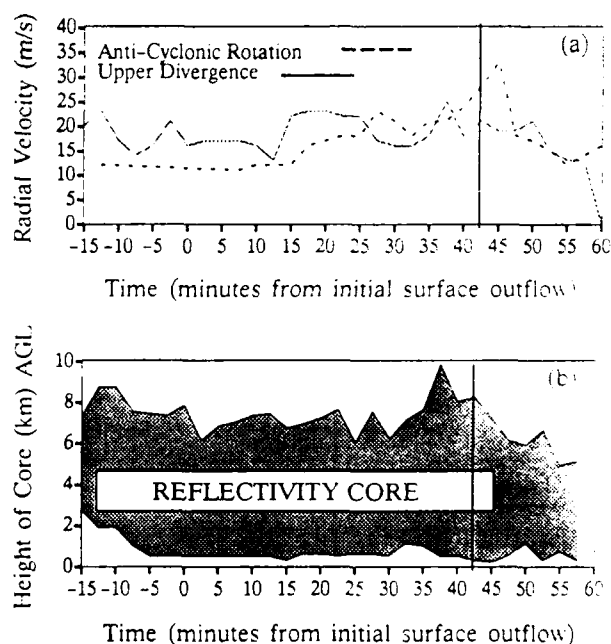
Figure 5. (a) Velocity features aloft observed throughout the life
cycle of the Claycomo microburst. (b) Height of the reflectivity core
throughout the life cycle of the Claycomo microburst.

tion is first observed at T - 13 minutes; however, this feature
is not consistently observed until after the initial microburst
outflow. It reaches a maximum intensity of 32 m/s over 1°
azimuth. At a distance of 30 km, this represents a single-
Doppler vorticity of 61 x 10 $^{-3}$ s^{-1}. The rotation produced
in this downdraft is comparable to the vertical vorticity of
a misocyclonic microburst observed in Colorado (Kessinger
et al. 1984). The severity of this microburst could have been
predicted by the increase in the depth of the reflectivity core

2

and the intensity and trend of mid- and upper-level features such as anticyclonic rotation and upper-level divergence.

2.3. Liquid Water Based Measures

The average vertically integrated liquid water (VIL) was estimated at a 45 dBZ contour using a prototype algorithm based on Greene and Clark (1972). The volume of integration was the three-dimensional structure based on the 45 dBZ storm boundary (Figure 6) which is recognized by the TDWR microburst detection algorithm as described in Merritt et al. (1989). The integration method uses a vol-

Figure 6. An example of a the reflectivity regions found in a cloud, their centroids, and the resulting CGZ.

ume weighted average of estimated liquid water content in the two-dimensional (tilt) regions followed by midpoint integration in elevation. The average VIL (as shown in Figure 7b) is then calculated by dividing the mass by the cell's area.
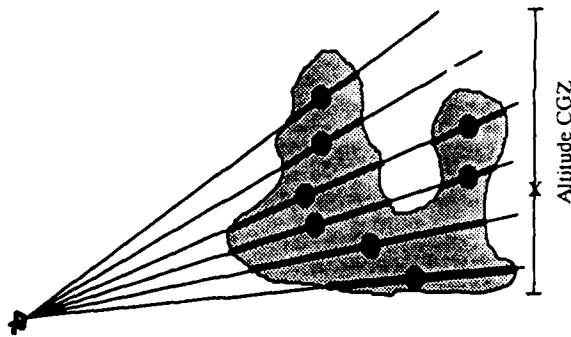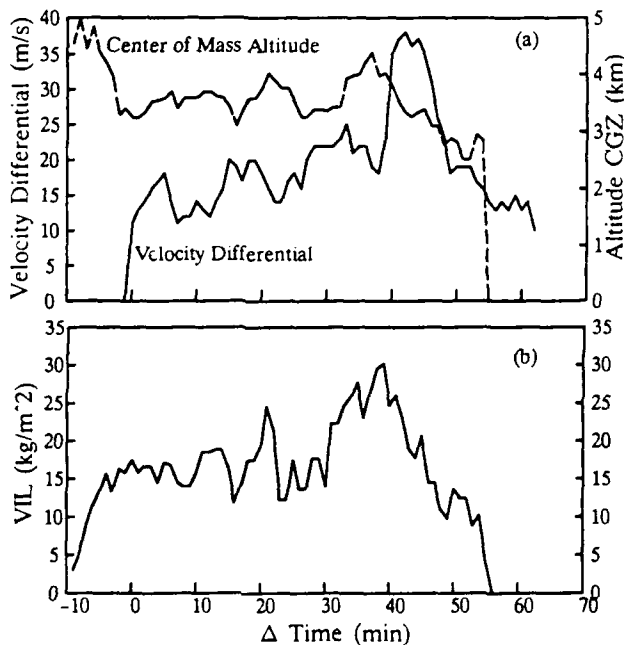
Figure 7. (a) Velocity Differential and Altitude of Center of Mass (CGZ) @ 45dBZ contour vs. ΔTime (b) VIL (@45 dBZ contour) vs ΔTime for Claycomo, Missouri microburst on July 30, 1989. T=0 is 084828 UT.

The altitude of the center of mass (CGZ) shown in Figure 7a was estimated at the 45 dBZ contour. As shown in Figure 6, 45 dBZ regions whch overlap are associated together by the TDWR microburst detection algorithm. The CGZ is calculated as follows:

$$CGZ = \frac{\sum M_i Z_i}{\sum M_i}$$

where M_i are the masses of the individual regions and Z_i are their altitudes, with i denoting the particular region. Because the regions actually represent a wedge shaped section of space, this does not give a true center of gravity (the estimate will always be low), but it is a good first-order estimate.

Figure 8 is a time series of contour plots of this storm's reflectivity. Figure 8a is 11° PPIs which were selected to reveal the storm structure at 5 km AGL. Figures 8b and 8c are time series of synthesized RHIs at two different azimuths in the storm which shift in order to track significant features at different times. Figure 8d is the FL-2 radial velocity differential through the surface outflow plotted to the same time scale.

By examining this figure we can see that this was a complex multicell storm. The pulses in surface velocity differential can be associated with distinct sub-events in the storm evolution. Cell growth appeared on the western flank while cells collapsed to the east. The center of divergence was closely correlated in both time and space to the collapsing cells.

The TDWR microburst detection algorithm associates all of these sub-events into one large event because of the high reflectivity of the cells and their close proximity. The CGZ product was not able to resolve all of these sub-events, but it does show a pulsing behavior before each major pulse in the surface outflow, with descents at times -6, 13, 21, and 37 minutes. These descents preceded the surface velocity differential with mean lead times of 2.5 minutes for pulse onset and 7.5 minutes for pulse peak. We believe the increases in CGZ prior to the descents were caused by 1) formation of new precipitation aloft and 2) a loss of precipitation loading from the bottom of the storm from a previous cell's collapse. The descents of CGZ were made apparent by their preceding increases; it is not clear whether CGZ would be effective in identifying these sub-events, and thus anticipating pulses in velocity, in other multicell storms.

The average VIL reached its peak 3 minutes before the peak outflow. It does not appear to be a good predictor for the timing of the pulses in this microburst. However, it was a good predictor of the strength of these pulses. The VIL values calculated at th. beginning of each core descent (as sensed by CGZ descent) were 12, 19, 25, and 27 kg/m². The peaks of the subsequent divergence pulses were 18, 20,

3
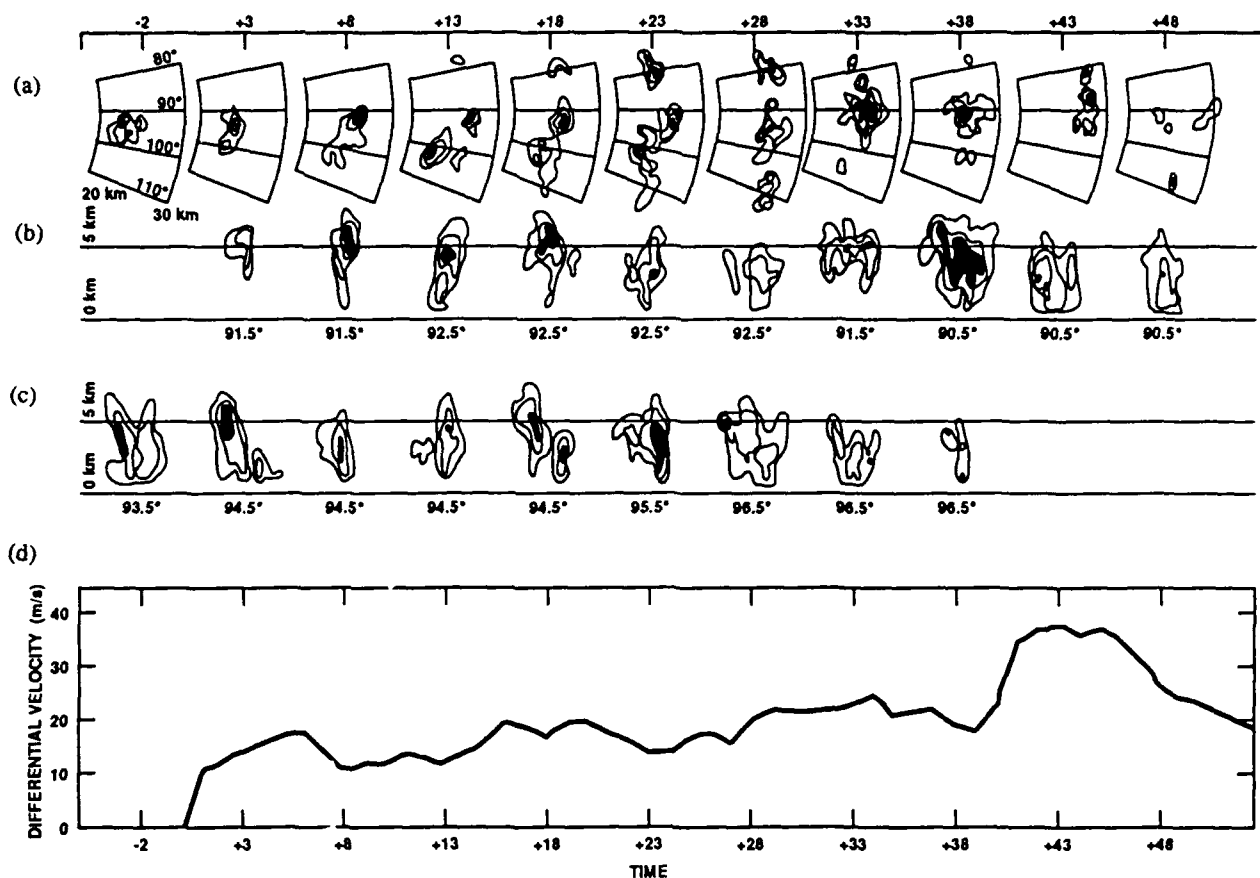
Figure 8. (a) Time series of 11° PPIs with contours at 45 and 50 dBZ. Solid areas are above 55 dBZ.
    (b) and (c) synthetic RHIs at selected azimuths through the storm. The contours and time scale are the same as in the PPIs shown in (a).
    (d) FL-2 surface velocity differential magnitude (m/s) plotted to the same time scale.

25 and 38 m/s. Thus, higher VIL values were associated with greater surface velocity differentials.

2.4. Aircraft Hazard Index

Figure 9 is a plot showing ΔV and $\Delta V/\Delta R$ throughout the life cycle of the microburst. It can be seen from this plot that the maximum $\Delta V/\Delta R$ was not coincident with the time of maximum ΔV. The event pulsed a number of times prior to dissipation. In fact, the ΔV of the outflow was greater with each subsequent pulse.

An assessment of how this microburst would have affected an aircraft's performance can be made by considering the F-factor, a derived quantity which characterizes the effect of a wind shear encounter on the flight performance of an aircraft as a function of $\Delta V/\Delta R$. Targ and Bowles (1988) define the F-factor as:

$$F = \frac{\frac{Dv_x}{Dt}}{g}\cos\gamma + \frac{\frac{Dv_z}{Dt}}{g}\sin\gamma - \frac{W}{TAS}$$
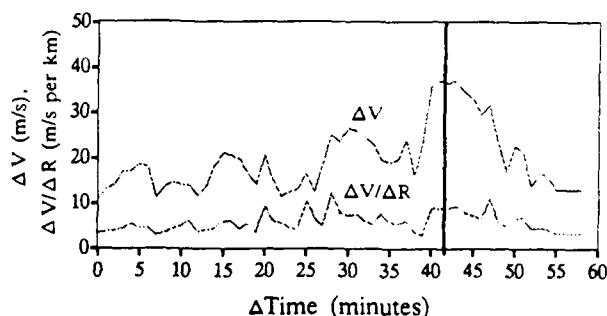
Figure 9. $\Delta V/\Delta R$ (m/s per km) and ΔV (m/s) vs. $\Delta Time$ (min.) (FL-2) for the Claycomo, Missouri microburst on July 30, 1989. T=0 is 084828 UT. The heavy vertical line indicates the time of maximum surface outflow.

where γ is the flight path angle, TAS is the true air speed of the aircraft, g is the gravitational constant of acceleration, and W is the vertical wind velocity. The substantial derivative with respect to time is given by:

4

$$\frac{Dv_x}{Dt} = \frac{\delta v_x}{\delta t} + V_h \frac{\delta v_x}{\delta x} + V_v \frac{\delta v_x}{\delta z}$$

where V_h is the horizontal component of the aircraft velocity, V_v is the vertical component of the aircraft velocity, and $\delta v_x/dx$ and $\delta v_x/dz$ are the horizontal and vertical components of the wind, respectively, along the flight path of the aircraft. Assuming a "frozen" wind field in time, stable flight ($\gamma = 0$), and $V_h = TAS$, the F-factor is approximated by:

$$F = \frac{TAS \dfrac{\delta v_x}{\delta x}}{g} - \frac{W}{TAS}$$

In a paper by Elmore and Sand (1989), F-factor was plotted as a function of $\Delta V/\Delta R$ for 39 microbursts. In their analysis, a TAS of 75 m/s was used in the space-to-time conversion from $\Delta V/\Delta R$ to Dv_x/Dt. W is estimated from a sine wave model of divergent outflow. An F-factor of 0.13 is said to be the nominal value for aircraft performance to be marginal for level flight.

In the case of the Claycomo microburst, the maximum $\Delta V/\Delta R$ of 12.2 m/s per km would correspond to an F-factor of 0.186, significantly above the hazard threshold of 0.13 (indicated by the horizontal line in Figure 10). Figure 10 is a plot of F-factor throughout the life history of the microburst. It can be seen that the F-factor peaked above the hazard threshold five separate times and remained above this threshold for four minutes at the time of maximum ΔV. The maximum $\Delta V/\Delta R$ of 14.1 m/s per km as seen by the UND radar (not plotted) would correspond to an F-factor of 0.21(X in figure 10), a considerable hazard to an aircraft penetrating the outflow. This is comparable to the F-factor calculated for a hazardous microburst windshear on July 11, 1988 at Denver's Stapleton Airport (Schlickenmaier, 1989). Due to scanning strategy, UND data is only available from 093115 UT through 094307 UT (41 to 47 minutes).

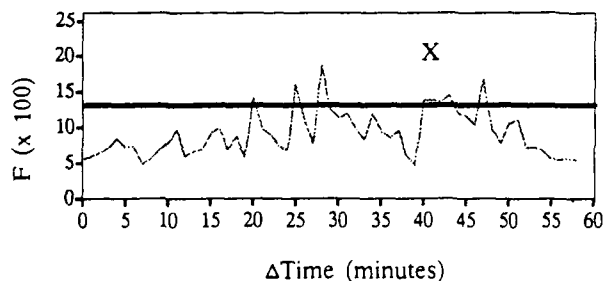*Figure 10. F-factor vs. ΔTime (Fl-2) for the Claycomo, Missouri microburst on July 30, 1989. T=0 is 084828 UT. X corresponds to the UND peak F-factor*

3. CONCLUSION

On July 30, 1989, a strong multicell thunderstorm near Claycomo, Missouri produced a microburst with a maximum differential velocity of 45 m/s. This was the strongest microburst observed during the 1989 data collection season in Kansas City. The microburst was preceded by mid- and upper-level velocity features as well as a descending high reflectivity core. For this case, each surface velocity differential pulse was preceded by a descent in CGZ. The average VIL at the beginning of the CGZ descent was a good predictor of the ranking of the surface velocity differential pulse magnitudes. An analysis of the maximum $\Delta V/\Delta R$ and F-factor revealed that this microburst would have been a considerable hazard to an aircraft penetrating the outflow.

REFERENCES

Campbell, S., 1989: "Use of Features Aloft in the TDWR Microburst Recognition Algorithm," 24th Conference on Radar Meteorology, Tallahasee, FL.

Elmore, K. and W. Sand, 1989: "A Cursory Study of F-Factor Applied to Doppler Radar," 3rd International Conference on the Aviation Weather System, Anaheim, CA.

Greene, D. and R. Clark, 1972: "Vertically Integrated Liquid Water -- A New Analysis Tool," *Monthly Weather Review*, **100**, 548-552.

Kessinger, C.J., J.W. Wilson, M. Weisman and J. Klemp, 1984: "The Evolution of Misoscale Circulations in a Downburst Producing Storm and Comparison to Numerical Results," 22nd Conference on Radar Meteorology, Zurich, Switzerland.

Merritt, M., D. Klingle-Wilson, and S. Campbell, 1989: "Wind Shear Detection with Pencil-Beam Radars," *The Lincoln Laboratory Journal*, **2**, 483-510.

Schlickenmaier, H.W., 1989: "Windshear Case Study: Denver, Colorado, July 11, 1988," FAA Technical Report DOT/FAA/DS-89/19.

Targ, R. and R Bowles, 1988: "Investigation of Airborne Lidar for Avoidance of Windshear Hazards," AIAA Conference on Sensor and Measurement Techniques for Aeronautical Applications, Atlanta GA.

A PROTOTYPE MICROBURST PREDICTION PRODUCT FOR THE TERMINAL DOPPLER WEATHER RADAR *

Steven D. Campbell and Mark A. Isaminger

Lincoln Laboratory
Massachusetts Institute of Technology
244 Wood Street
Lexington, Massachusetts, U.S.A.

1. INTRODUCTION

This paper describes a prototype microburst prediction product for the Terminal Doppler Weather Radar (TDWR). The prediction product was evaluated for microbursts observed during the spring and summer of 1989 at Kansas City. Results are presented demonstrating reliable prediction of high reflectivity microbursts of at least 15 m/s outflow intensity from single-Doppler radar data. The ability of the algorithm to predict microbursts approximately five minutes prior to the onset of surface outflow could be used to improve air traffic control (ATC) planning and to improve hazard warning time to pilots. In particular, this product could allow aircraft to avoid an impending microburst hazard, rather than penetrating it.

The present TDWR microburst recognition algorithm uses features aloft such as reflectivity cores and convergence to recognize microburst precursors. The algorithm uses precursors to make a microburst declaration while the surface outflow is still weak, thereby improving the hazard warning time (Campbell, 1989). The microburst prediction product is an extension of the algorithm to predict microbursts from these precursor signatures. The prototype prediction product is tuned to predict the high reflectivity microbursts typical of humid regions of the United States.

The paper begins by reviewing conceptual models for microburst development and comparing them to the observed characteristics of Kansas City microbursts. The prototype prediction product is then described, and performance statistics are presented. Finally, failure mechanisms and future work are discussed.

2. MICROBURST PRECURSORS

Research in Colorado (Fujita and Wakimoto, 1983, Roberts and Wilson, 1989, and Biron and Isaminger, 1989), Oklahoma (Eilts, 1987), and Alabama (Isaminger, 1987) identified precursors to microbursts such as descending reflectivity cores, mid-level rotation and convergence, reflectivity notches, upper-level divergence and lower-level divergence. Conceptual models were developed by Fujita and Wakimoto (1983), Roberts and Wilson (1989), and Campbell

(1988) to describe the storm evolution prior to a microburst outflow. The model for high reflectivity microbursts developed by Roberts and Wilson (1989) encompasses the vast majority of Kansas City microbursts. In this model, the combination of an increasing radial convergence at or near cloud-base and a descending reflectivity core was deemed a good radar indicator of a downdraft. The presence of rotation or reflectivity notches in combination with either of the above features was also considered a microburst precursor.

The characteristics of a typical Kansas City microburst producing cell were determined based on an examination of radar data for 18 events reaching a magnitude of 15 m/s or greater. As shown in Table 1, the most reliable feature was a descending high reflectivity core, which was observed in over 90% of the cases. Cyclonic rotation, anticyclonic rotation, convergence, and upper divergence were observed in three-quarters of the events. Kansas City microbursts were just as likely to be preceded by rotation and upper divergence as convergence.

The lead times from Table 1 were used to develop a conceptual model for the evolution of a typical Kansas City microburst. In the early stage of development, an updraft is indicated by the upper-level divergence at T-9 (i.e., nine minutes prior to the surface outflow initially reaching 10 m/s). At T-7, rotation is first observed in the cell at mid-levels. The reflectivity core descends at T-5 minutes, shortly after convergence is apparent within the core.

Of the features aloft observed, the descending reflectivity core was the most reliable indicator of downdraft onset. The lead time for the observation of descending cores had a standard deviation of 2.3 minutes. There was greater variability in the lead time for the mid- and upper-level velocity features, with standard deviations ranging from 4.7 to 5.7 minutes.

3. PRODUCT DESCRIPTION

The microburst recognition algorithm relies on the ability of the TDWR to scan both at the surface for microburst outflows and aloft in the parent cloud for features associated with microbursts, as shown in Figure 1 (Campbell, 1988). Features aloft associated with microbursts include high reflectivity cores, mid-level convergence and rotation, and upper-level divergence. These features aloft can be used

*Table 1. Radar observables in Kansas City micro-
burst producing cells. Percent occurrence,
lead time prior to onset of surface outflow
and standard deviation, based on 18 micro-
bursts reaching 15 m/s.*

Radar Feature	% Occur.	Lead time (min.)	Std.Dev. (min.)
Upper divergence	72.2	9.0	5.7
Cyclonic rotation	77.8	7.0	4.7
Anticyclonic rot.	77.8	7.0	5.5
Convergence	77.8	5.8	5.7
Descending core	94.4	5.0	2.3

*Figure 1. Illustration of TDWR scanning at surface for microburst
outflows and aloft in parent storm for features associated
with microbursts.*

to both confirm the existence of a microburst outflow and to predict a future microburst outflow.

The current TDWR microburst recognition algorithm detects microburst precursor signatures which typically precede the surface outflow by five to ten minutes. The criteria for declaring a microburst precursor are that a reflectivity core must be detected along with a mid-level convergence, mid-level rotation (cyclonic or anticyclonic) or upper-level divergence. The reflectivity core must meet certain site adaptable criteria, such as a minimum height of 4.5 km and a maximum reflectivity of at least 54 dBZ. In addition, one of two additional criteria must be satisfied: either the reflectivity core must be descending, or a convergence (or rotation) must extend below 3.5 km altitude. These criteria are intended to detect the presence of a strong downdraft which will lead to a microburst outflow at the surface.

Microburst precursor signatures are used in the current algorithm to increase the timeliness of microburst declarations (Campbell, 1989). Normally, the microburst algorithm must wait until a microburst outflow is detected on successive surface scans spaced one minute apart, and the second outflow must be at least 10 m/s (20 knots). However, when a precursor signature is detected the microburst can be declared when the initial, weak (< 10 m/s) surface outflow is detected.

The microburst prediction product is a simple extension of the existing microburst precursor recognition capability. The first time that a precursor is detected for a particular event, a microburst prediction is issued for five minutes in the future at the precursor location. This prediction is counted down for each subsequent surface scan (once per minute) until either the microburst occurs or a total of seven minutes elapse. The prototype prediction product does
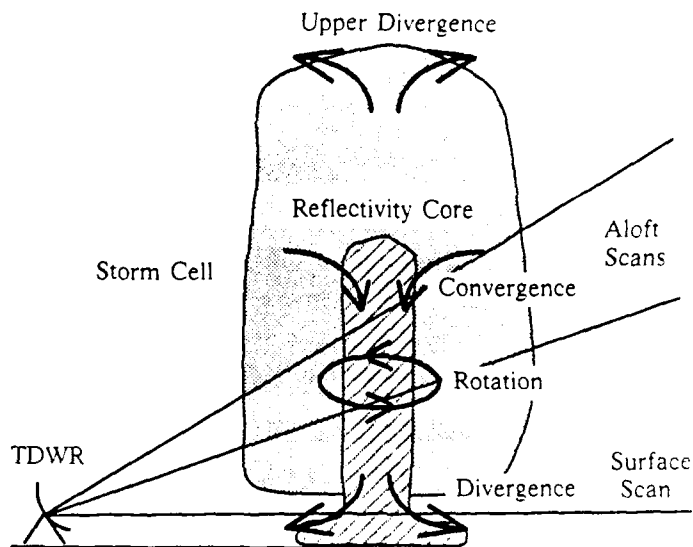
not predict the strength of the outflow, although the site adaptable parameters are intended to predict those microbursts reaching at least 15 m/s (30 knots) intensity.

It should be pointed out that the current version of the prediction product is aimed at predicting high reflectivity microbursts of the type commonly found in the Southeast United States. This type of microburst activity is expected to predominate at practically all airports scheduled for TDWR deployment, except for dry environments such as Denver which are characterized by low reflectivity events.

4. PERFORMANCE STATISTICS

The prototype microburst prediction product was tested using data from the FL-2 TDWR testbed radar operated by Lincoln Laboratory at Kansas City during the summer of 1989. The algorithm performance was assessed for eleven days between 14 May and 28 August on which microbursts occurred. Only those cells which developed in the airport sector and within 35 km of the FL-2 radar were considered (see Figure 2). A microburst was defined as a 10 m/s or greater radial divergence either at the surface or below 1 km AGL, as observed by either the S-band FL-2 radar or the C-band UND radar operated by the University of North Dakota.

The results of this assessment are shown in Table 2. A total of 89 microburst events were examined, 36 of which reached 15 m/s intensity. The product successfully predicted 61% (22 of 36) of the microbursts that reached 15 m/s. There were 45 microburst predictions issued, of which 40 (89%) resulted in microbursts of at least 10 m/s, and 5 (11%) were false alarms. The median time from initial prediction to onset of surface outflow was 5.0 minutes with a standard deviation of 2.8 minutes.

8

Figure 2. Radars used in 1989 Kansas City operation.

Table 2. Kansas City Microburst Prediction
Product Statistics.

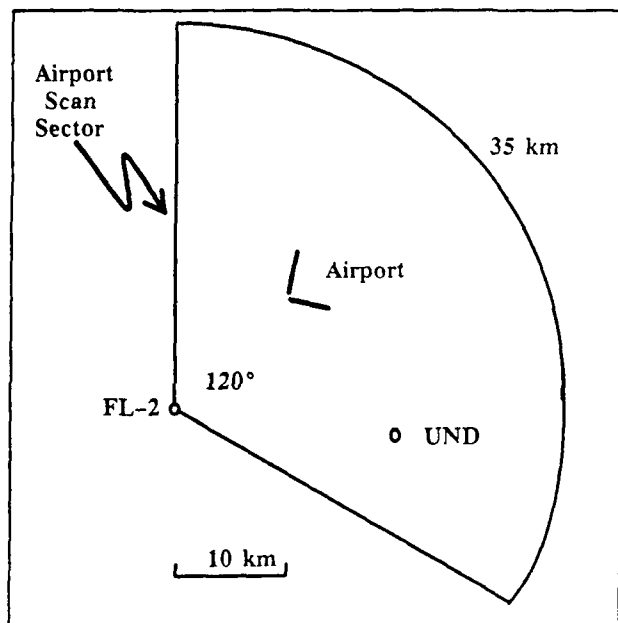|	
Number of events	89
Number of events ≥ 15 m/s	36
Number of events ≥ 15 m/s successfully predicted	22 (61%)
Number of predictions issued	45
Number of valid predictions (≥ 10 m/s outflow)	40 (89%)
Number of false predictions	5 (11%)
Median prediction lead time (minutes)	5.0
Standard deviation of prediction lead time (minutes)	2.8

Of the 40 valid predictions, there were two which did not reach 10 m/s from the FL-2 perspective, but did from the UND perspective. A likely cause of the difference in observed intensities is asymmetry in the microburst outflow. There were two additional events which exhibited divergence above the surface but below 1 km AGL. These events may be instances of the microburst divergence not reaching the surface due to a shallow layer of cold air from a previous outflow. These results suggest a potential use for features aloft in compensating for outflow asymmetry and the detection of mid-air microbursts.

Figure 3 summarizes the velocity features aloft that were found by the algorithm when microburst predictions were made (note: more than one velocity feature may be identified by the algorithm for a particular event). Cyclonic or anticyclonic rotation was found for slightly more than half of the predicted events. Convergence was detected in 30% of the cases, while upper-level divergence was seldom used to make a prediction. Reflectivity cores were identified in all cases (as required by the current algorithm), however, the core was identified as descending in only one-half of the cases. When compared to Table 1, these results suggest that the current algorithm does a credible job in detecting rotation, but needs improvement in the detection of mid-level convergence and upper-level divergence, and in the ability to declare cores as descending.
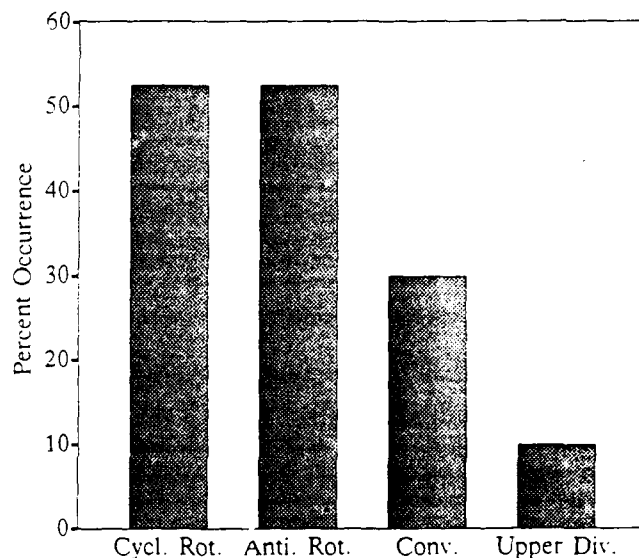
Figure 3. Velocity features aloft identified by algorithm when microburst predictions were made (percent occurrence for 40 cases).

5. FAILURE MECHANISMS

In this section, the failure mechanisms of the algorithm will be examined. Three of the fourteen microbursts which were not predicted exceeded a velocity differential of 20 m/s. Therefore, it is important to further analyze these so that improvements can be made to the prediction product.

As seen in Figure 4, half of the missed predictions were because the reflectivity core did not attain the maximum height threshold of 4.5 km. Other causes for missed predictions were: no reflectivity core detected, overlap with a preexisting microburst, not attaining the maximum reflectivity threshold, and no velocity feature detected. It appears that there is a class of lower reflectivity Kansas City microbursts which did not meet the current criteria for precursor declaration.

Further analysis of the prediction product performance suggests that the criteria used for reflectivity core height (4.5 km) and maximum reflectivity (54 dBZ) may be too restrictive for the Kansas City environment. These criteria were

9
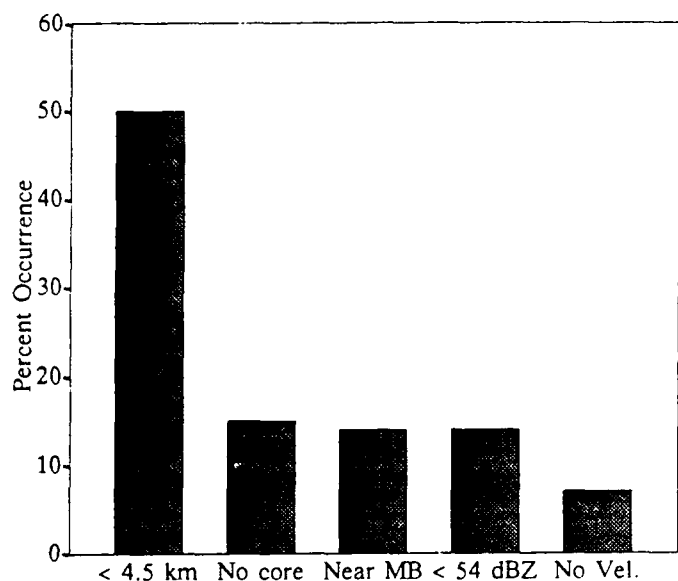
Figure 4. Reason for missed predictions of Kansas City microbursts (percent occurrence for 14 cases).

developed based on an earlier examination by Isaminger (1987) of microbursts in the Huntsville, AL area. It was found that the core height threshold could not be lowered without causing an unacceptable increase in false alarms. However, lowering the reflectivity threshold to 51 dBZ would increase prediction POD to 67% without impacting the false alarm rate.

To reduce false predictions, 40% could be eliminated by reducing the threshold for the lower altitude limit on velocity features from 3.5 to 2.7 km. It should be noted that such criteria as core height, maximum reflectivity and velocity feature lower altitude limit are parameters which can be adjusted on a site-adaptable basis to optimize performance.

6. FUTURE WORK

There are several areas for future work on the prediction product. As noted above, the current product does not predict low reflectivity microbursts typical of dry environments such as Denver, since these events are not associated with high reflectivity cores. Also, one-half of the microbursts not predicted in Kansas City were lower reflectivity events. It is possible that an extension of the algorithm to use moderate- and low-reflectivity structures (also recognized by the current algorithm) may allow these events to be predicted.

The current product does best at predicting isolated microbursts, and performance decreases whenever multiple outflows occur in close proximity, such as along a squall line or in large storm complexes. After the descent of the initial reflectivity core, the algorithm has difficulty in recognizing secondary descending cores associated with reintensifying or pulsating outflows. Work has begun at Lincoln in examining the use of features aloft in combination with detected surface outflows to predict microburst reintensification.

Other areas for future work are to improve the accuracy of prediction time and to add outflow strength prediction. Work has begun at Lincoln on the use of storm liquid water content to improve prediction time accuracy, and to potentially provide microburst strength and trend estimates.

7. SUMMARY

A prototype TDWR microburst prediction product was developed as an extension to the existing TDWR microburst recognition algorithm. This product was evaluated in the Kansas City environment and shown to predict over 60% of microbursts reaching 30 knots intensity. The average lead time from initial prediction to onset of surface outflow was five minutes. Of the predictions issued, nearly 90% resulted in microbursts of at least 20 knots intensity. Thus, favorable performance was demonstrated in a wet environment likely to be representative of most TDWR installation sites. It was shown that minor changes to site adaptable parameters could improve the prediction rate and reduce false predictions.

Further testing of the product will be conducted at Orlando, FL during the summer of 1990. Plans for these tests include operational evaluation of the prediction product by ATC personnel, and real-time display in the cockpit of an experimental aircraft. Longer-term work is planned to improve prediction of lower reflectivity events, and to include microburst strength prediction and trend estimation.

8. REFERENCES

1. Biron, P.J., and M.A. Isaminger, 1989: An Analysis of Microburst Characteristics Related To Automatic Detection from Huntsville, Alabama and Denver, Colorado, 24th Conference on Radar Meteorology, AMS, Boston, MA, 269-273.

2. Campbell, S.D., 1988: Microburst Precursor Recognition Using an Expert System Approach, 4th International Conference on Interactive Information and Processing for Meteorology, Oceanography, and Hydrology, AMS, Boston, MA, 300-307.

3. Campbell, S.D., 1989: Use of Features Aloft in the TDWR Microburst Recognition Algorithm, Preprints, 24th Conference on Radar Meteorology, AMS, Boston, MA, 167-170.

4. Eilts, M.D., 1987: Nowcasting Low-altitude Wind Shear with a Doppler radar, AIAA 25th Aerospace Sciences Meeting, Reno, Nevada, 1-5.

5. Fujita, T.T, and R.M. Wakimoto: JAWS Microbursts Revealed by Triple-Doppler Radar, Aircraft, and PAM Data, Preprints, 12th Conference on Severe Local Storms, AMS, Boston, MA, 97-100.

6. Isaminger, M.A., 1987: A Preliminary Analysis of Huntsville Microburst Precursors, Project Report ATC-153, MIT Lincoln Laboratory.

7. Roberts, R.D., and J.W. Wilson, 1989: A Proposed Microburst Nowcasting Procedure Using Single-Doppler Radar, Journal of Applied Meteorology, 28, 285-303.

PREDICTING SUMMER MICROBURST HAZARD
FROM THUNDERSTORM DAY STATISTICS *

Joseph A. Cullen and Marilyn M. Wolfson

MIT Lincoln Laboratory

Lexington, Massachusetts 02173

1. INTRODUCTION

Low-altitude wind shear, specifically, the aviation-hazardous form of wind shear known as the microburst, has been cited as the cause of several aviation disasters over the past two decades (Zorpette 1986). Microbursts are strong, small-scale convective storm downdrafts that impact the ground and cause a violent divergent outflow of wind. The Federal Aviation Administration (FAA) recently awarded a contract for the production of 47 Terminal Doppler Weather Radars (TDWRs) to detect microbursts (Evans and Turnbull 1989, Turnbull et al. 1989). Since the TDWR systems are expensive, only a limited number will be available for use at major U.S. airports. In deciding which airports will receive the TDWRs or any other advanced detection equipment, such as the ASR-9 with wind shear detection capability (Weber and Noyes 1988) or the Enhanced Low Level Wind Shear Alert System (Barab et al. 1985), a detailed cost-benefit study will be performed (Martin Marietta Information Systems Group 1989). One factor that would aid in determining the benefit of advanced wind shear detection equipment is a knowledge of the average relative microburst threat at each major airport. Using "thunderstorm day" statistics and the results of measurements by the FAA TDWR testbed systems, we propose a method for predicting this threat.

2. THE STUDY

Microburst statistics are not routinely collected, so some other convective storm related data must be used to determine the level of microburst hazard at each U.S. airport. One thunderstorm related statistic with a long archive and nationwide coverage is the "thunderstorm day", a calendar day on which thunder is heard at least once by a weather observer (Department of Commerce 1958). Thunderstorm day statistics have been gathered at NWS offices around the country for approximately 100 years.

Using actual TDWR testbed microburst data obtained in Memphis (1984 and 1985), Huntsville (1986), and Denver (1987 and 1988) and the reported number of thunderstorm days at these sites, we use statistical regression techniques to derive a mathematical relationship between microburst occurrence and the number of thunderstorm days recorded at each location.

The time period common to all our data is June 8 to September 8. This corresponds closely to the climatological definition of summer (June 1 to August 31), the season in which microburst activity is known to be at its peak. Thus, our derivation will predict the average number of summer microbursts occurring at most airports for which thunderstorm day data is available.

3. RELATING MICROBURSTS TO THUNDERSTORM DAY STATISTICS

3.1. Determining a Region of Applicability

The method for comparing the number of microbursts that occur around an airport to the actual number of thunderstorm days recorded there requires an estimate of the actual distance over which thunder can be heard by weather observers. Ideally, thunder can be heard at distances as great as 25-30 km (Viemeister 1961), but a weather observer stationed at an airport would hear thunder over a smaller area because 1) the observer spends most of the time indoors performing various duties and 2) the din of air traffic drowns out thunder originating at great distances. Thus, we define the *Thunderstorm Day Observation Region* (**TDOR**) as a circle of radius 15 km around the weather observation site. Only the microbursts that occur within the TDOR will be related to the thunderstorm day statistics.

3.2. Tallying Microbursts in the TDOR

To count microbursts in the TDOR, we chose to use mesonet data instead of Doppler radar data, or a combination of both, because the mesonet operated continuously and also provided us with an additional year of data (Wolfson 1989). Even though the mesonet does not sample uniformly, we can be assured that most microbursts that did fall in the net were detected because of the fairly dense station spacing

Table 1 . *Average station spacing (only those stations within 15 km of NWS site were used), coverage areas and scale factors used for each mesonet site.*

MESONET SITE	AVERAGE SPACING BETWEEN STATIONS (km)	APPROX. AREA OF COVERAGE (sq km)	SCALE FACTOR
Memphis 1984	1.90	190	3.72
Memphis 1985	2.16	240	2.95
Huntsville 1986 (w/ PAM) *	1.89	300	2.36
Huntsville 1986 (w/o PAM)	2.51	250	2.83
Denver 1987 & 1988	1.36	200	3.53

* The 1986 mesonet was enhanced by the presence of 41 additional portable automated mesonet stations during the COHMEX Project (Dodge et al. 1986) in June and July. This resulted in two different average station spacings for that year.

11

(Table 1). Microbursts which impacted the mesonet were identified by DiStefano (1987, 1988), Clark (1988), and DiStefano and Clark (1990). They found only a few microbursts that were detected by Doppler radar but not by the surface weather station network. Since these misses represent a very small percentage of the total number of observed microbursts, a correction for microburst misses by the mesonet was deemed unnecessary.

Given that mesonet data is to be used for counting microbursts in the TDOR, an *area of coverage* for each mesonet must be determined. The coverage area will be the sum of the individual mesonet station *influence areas* and will determine the fraction of the TDOR that was sampled. The influence area for a single mesonet station can be estimated from the working definition of a microburst. Fujita (1985) defines a microburst as a wind velocity differential of at least 10 m/s over a distance of 4 km or less. Therefore, if we assign an influence area equal to a circle of radius 2 km to each mesonet station, even a weak microburst, with a velocity differential of 10 m/s impacting two mesonet stations exactly 4 km apart, will be detected just within the influence area of the two stations. The average station spacing for each network provides solid areal coverage over most of the mesonet.

Since we ultimately want to project how many microbursts occurred within the TDOR based on our mesonet-detected microbursts that also occurred there, we need to determine the intersection of the solid area of mesonet coverage (given by the union of all the stations' influence areas) with the TDOR. This intersection yields an approximate area of coverage. An example of a mesonet's areal coverage is shown in Figure 1 along with the 15-km radius circle bounding the TDOR.
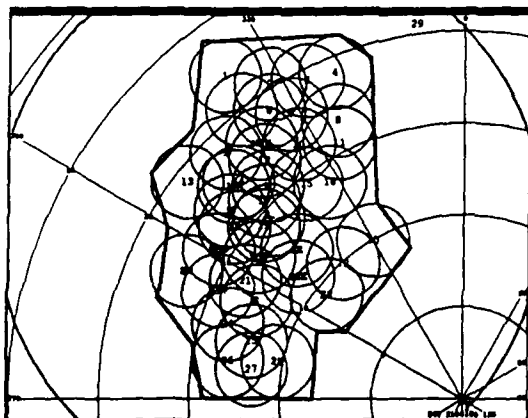

Figure 1 . Area of coverage for mesonet at Denver, CO. Circles of radius 2 km represent influence areas of individual mesonet stations, outer boundary of TDOR is visible at corners of illustration, and total area of mesonet coverage is represented by irregularly shaped polygon.

If we assume microburst occurrence is random and evenly distributed, multiplying the number of microbursts detected within the mesonet coverage area by a scale factor equal to the ratio of the area of the TDOR to the mesonet coverage area will yield a projected number of microbursts occurring within 15 km of the observation site. This assump-

tion of isotropic microburst occurrence is supported by the observed distribution of mesonet-detected microbursts (e.g., Figure 2). The scale factors used for each network are given in Table 1. The actual thunderstorm days recorded by NWS observers from June 8 through September 8 at each of the sites (T) and the scaled number of microbursts appropriate for comparison (M) are given in Table 2 .
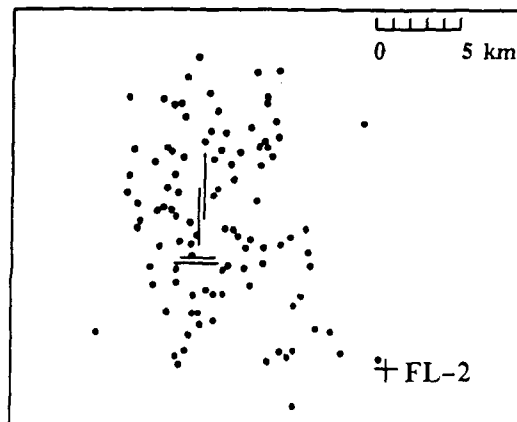
Figure 2 . Locations of the 1987 mesonet-impacting microbursts at the times of their peak strength (DiStefano, 1988). Solid horizontal and vertical lines represent position of runways at Stapleton International Airport. Similar isotropic distributions were observed during 1985 and 1986 in Memphis and Huntsville, respectively (DiStefano 1987, Clark 1988).

4. RELATING WET AND DRY MICROBURSTS TO THUNDERSTORM DAYS

Our results show that microbursts occur mainly on thunderstorm days in the southeastern part of the country, whereas many microbursts occur on days that are not thunderstorm days in the Denver area (Table 2). This is due to the common occurrence of *dry* microbursts in the Western Plateau. Dry microbursts originate from benign-looking, high-based cumulonimbus clouds that produce little if any surface rain (Krumm 1954; Wakimoto 1985; Wilson et al. 1984). These clouds are less likely to produce lightning (and therefore thunder) than the more typical low cloud base, heavy rain thunderstorms (Williams et al. 1989a).

Table 2 . Summary of scaled microburst and thunderstorm day data for each mesonet site. T is the observed number of thunderstorm days, M the total number of microbursts, MT the number of microbursts on thunderstorm days, MX the number of microbursts on non-thunderstorm days, Mwet the number of wet microbursts, and Mdry the number of dry microbursts.

MESONET SITE	T	M	MT	Mx	Mwet	Mdry
M 84	21	48	37	11	48	0
M 85	24	77	71	6	77	0
H 86	23	132	125	7	132	0
D 87	30	297	177	120	92	205
D 88	27	406	289	117	120	286

12

To check this assumption, we examine the surface rainfall characteristics of microbursts that occur both on thunderstorm days (given the symbol M_T) and on non-thunderstorm days (M_x). The total number of microbursts may be subdivided according to:

$$M = M_{wet} + M_{dry}$$

where M is the total number of microbursts that occur, M_{wet} the number that occur with measurable surface rainfall, and M_{dry}, those without measurable surface rainfall. However, it is also true that

$$M = M_T + M_x.$$

Because the type of microbursts in Denver appear different from those typical of the Southeast, we can anticipate that it will be necessary to derive two different equations to predict summer microburst occurrence in these regions.

4.1.   Rainfall Characteristics of M_x and M_T

All of the microbursts on non-thunderstorm days (M_x) in Denver 1987 were "dry" (Table 2); no measurable rainfall was detected at the surface. In Denver 1988, radar and mesonet data indicate only 21% of the microbursts on non-thunderstorm days were wet. Thus, as expected, the vast majority of microbursts occurring on non-thunderstorm days in Denver were dry.

In contrast to Denver, microbursts rarely occurred on non-thunderstorm days in the Southeast. During the study period, only 9% of the microbursts were observed on non-thunderstorm days (M_x) in Memphis and Huntsville (Table 2). Radar and mesonet rainfall data indicate at least 75% of these microbursts were wet. The rainfall characteristics of the other two events could not be determined because of lack of radar and rain gage data. (Interestingly, 38% of these microbursts on non-thunderstorm days occurred near the outer boundary of the TDOR.)

Based on the surface rainfall information, we found that the microbursts on non-thunderstorm days (M_x) were both wet and dry in Denver and only wet in Huntsville and Memphis. The observation of wet microbursts on non-thunderstorm days suggests possible observer error. Williams et al. (1989b) found only a small percentage of wet microbursts in 1987 and 1988 in Huntsville that were not accompanied by lightning, and these microbursts were very weak. Radar data for 6 of the 7 microbursts on non-thunderstorm days in Denver 1988 showed 40–55 dBz cells were present within 10 km of the observation site (Stapleton International Airport). Corona current measurements (Williams 1989) showed lightning was in the area during at least 5 of the events. However, the relationship between high radar reflectivity and lightning occurrence, and the exact locations of the lightning detected by the corona probe measurements are uncertain, so we cannot state conclusively that these occurrences represent observer error.

All microbursts in Memphis and Huntsville occurring on thunderstorm days (M_T) were associated with surface rainfall. However, in Denver only 52% of the events

in 1987, and 33% in 1988 were associated with surface rainfall.

4.2.   The Dependence of M_{wet} on T

Because two distinct types of microbursts occur in Denver and only one type occurs in the Southeast, an attempt to relate M, the *total* number of microbursts, to T using data from the two climatological regions would be inappropriate. It is more appropriate to relate similar types of microbursts to thunderstorm days. For Denver, M_{wet} is equal to only a fraction of the total number of microbursts. However, we assume that $M_{wet} = M$ in the Southeast, where we believe all microbursts are wet. Dry microburst occurrence in the Denver area will be considered in Section 5.

A least-squares statistical regression can be performed to determine the relationship between M_{wet} and T. The data was fit using the three basic mathematical models shown in Figure 3. Since the data consists of only six points (including the origin), only integer exponents are considered.

The rms error resulting from the least-squares fit of each model is indicated in parentheses in Fig. 3. Based on these errors, the linear model provides the best fit for the data and will be used as the expression relating M_{wet} to T. The coefficient "a" resulting from this fit is 3.7 ± 0.5, where 0.5 is the standard deviation of the regression coefficient. This implies that, on average, 3 or 4 wet microbursts occur within a TDOR on a given thunderstorm day. It is worth noting that the errors here are quite large. Not only is the sample small, but the available thunderstorm day data all falls within a very limited range, indicated by the shaded region in Fig. 3. More data over a larger number of years and a greater range of thunderstorm days is needed before much confidence can be placed in the linear model.
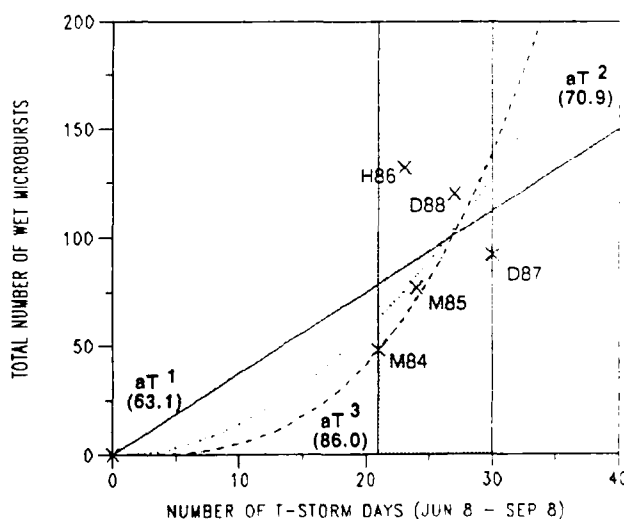

Figure 3.   Results of least-squares fits of selected models to the M_{wet} and T data shown in Table 2. Shaded region accentuates the limited range of data currently available for T

Assuming that each individual thunderstorm has the potential to spawn a microburst, we can speculate that more microbursts are likely to occur within a confined area (i.e.,

13

the Thunderstorm Day Observation Region) on a given thunderstorm day in the southern regions of the country (where thunderstorms are more frequent) than are likely to occur within the same area in the northern regions. Remembering that a weather observer records a thunderstorm day if he hears thunder *at least once* during any calendar day, it is plausible that the relationship between wet microbursts and thunderstorm days is nonlinear. The limited data we have to date suggests a linear relationship, but the acquisition of additional data may change this result.

5. PREDICTING MICROBURST OCCURRENCE

5.1. Predicting M_{wet}

To predict wet microburst totals in the Southeast and the Western Plateau region, direct use of the linear relationship between wet microburst totals and thunderstorm days is appropriate. This results in the following expression for the total number of wet microbursts.

$$M_{wet} = (3.7 \pm 0.5) \ T$$

The problem of predicting the total number of *dry* summer microbursts in the Western Plateau region is discussed in the following section.

5.2. Predicting M_{dry}

Dry microbursts occurred commonly on both thunderstorm days and non-thunderstorm days in Denver, and in inconsistent proportions to the wet microbursts on those days in the two different years of data. Remarkably consistent, though, was the percentage of the *total* summer microbursts that were dry; this was 69% in 1987 and 70% in 1988.

This observed consistency can be exploited in predicting M for Denver and the Western Plateau; assume M_{wet} determined in Section 5.1 is equal to 30% of the total number of microbursts. Then, if the wet to dry microburst ratio in Denver is characteristic of the *entire* Western Plateau, the equation projecting the total number of microbursts in the Western Plateau region is given by

$$\boxed{\begin{array}{c} \textbf{WESTERN PLATEAU} \\ \hline M_{wet} = (12.3 \pm 1.7) \ T \end{array}}$$

where the standard deviation of the regression coefficient determined in Section 4.2 has also been increased by 70% to 1.7. Thus, the average number of microbursts per recorded thunderstorm day in a Western Plateau TDOR is more than three times greater than in the rest of the country.

6. PREDICTING AVERAGE SUMMER AIRPORT MICROBURST HAZARD

To convert the equations for predicting mean summer microburst frequency in a TDOR into equations for predicting the average *summer hazardous* microburst frequency for an *airport* area, two additional factors need to be taken into account. These are described below.

6.1. Minimum Wind Shear Threshold for Hazard

The first TDWR Operational Demonstration conducted during July and August of 1988 at Stapleton International Airport in Denver (Turnbull et al. 1989) revealed that microbursts with differential velocities less than 15 m/s have very little impact on aircraft performance. However, the data used in this derivation defined a microburst as having a differential velocity of 10 m/s or more. Single Doppler peak estimates for microbursts which impacted the mesonet from 1985–1988 indicate that approximately 65% of both wet and dry microbursts detected by mesonet had a differential velocity greater than 15 m/s. The single Doppler peak estimate is comparable to the headwind–tailwind shear an aircraft would encounter during microburst penetration. Therefore, microburst totals predicted by our derived equations, multiplied by 0.65, will give the number of aviation-hazardous microbursts.

6.2. Airport Microburst Hazard Region

The TDWR Users Working Group recommends that a wind shear alarm region extend 3 nautical miles (5.6 km) from the end of airport runways (to protect the glideslope paths) and be 1 nautical mile (1.6 km) in width. Since most airport runways are not longer than 4 km in length, the region to be protected corresponds to approximately 25 square km per runway. The total area of the alarm region will vary from airport to airport, depending on the number of runways in use. However, our derived equations predict the number of microbursts expected within a circle of radius 15 km around an airport (the "TDOR"). Thus, to provide microburst totals that represent the aviation microburst hazard at each site, the number of predicted microbursts must be reduced by a factor R, the ratio between the areas of the wind shear alarm region of the airport of interest and the TDOR region.

$$R = \frac{\text{wind shear alarm region area (km)}^2}{\pi \ (15 \ km)^2}$$

6.3. Final Microburst Airport Hazard Equations

The inclusion of the factors mentioned in the preceding sections yields the final equations to be used to predict relative summer microburst hazard at U.S. airports. They are

$$\boxed{\begin{array}{c} \textbf{EQUATION A:} \\ \text{To be used for all parts of the country} \\ \text{except the Western Plateau} \\ \hline (2.4 \pm 0.3) \ T \ R \end{array}}$$

14

| **EQUATION B:** |
| To be used for the Western Plateau region only |

$$(8.0 \pm 1.1) \ T \ R$$

where T represents the mean number of *summer* thunderstorm days, and R is defined in Section 6.2.

6.4. Applicability of Microburst Hazard Equations

The final equations derived for relating microbursts to thunderstorm days are appropriate for summer only. In Denver, 69% of the annual thunderstorm days occur in the three summer months, on average (e.g., Court and Griffiths 1986). However, only 51% of the annual number in Huntsville, and 41% of the annual number in Memphis occur during the summer. Thus, a prediction of summer microburst totals clearly underestimates the *annual* microburst hazard in Memphis and Huntsville, relative to Denver. Furthermore, the microburst/thunderstorm day relationship could be different for the spring and fall seasons. Unfortunately, TDWR testbed mesonet data for these seasons is incomplete, so this relationship cannot be determined.

Since we currently lack data in regions where summer thunderstorm day totals are significantly lower or higher than in the regions used in this analysis, we suggest the resulting equations be used only for those locations where mean summer thunderstorm day totals fall within the range bounded by the Denver, Memphis, and Huntsville mean summer totals (22-30 thunderstorm days).

7. FUTURE WORK

TDWR testbed mesonet data obtained in Kansas City, Missouri in 1989 will be analyzed and additional data will be collected in Orlando, Florida (1990 and 1991) and possibly Washington, D.C. (1992). These data points can be included in this study as they become available. The data we have at present falls within a narrow range of thunderstorm days (21-30). Although Kansas City's mean summer thunderstorm day total also falls in this range, this data will be useful because it provides data from another climatological regime. The inclusion of microburst and thunderstorm day data from Orlando and Washington, which typically experience approximately 49 and 17 thunderstorm days during summer months, respectively, would certainly add confidence to our predictions made with the resulting equations. The prospect of obtaining two years of data from another site (Orlando) would also increase our confidence in the resulting equations since the significance of interannual variability in our derivation is still uncertain.

To check our argument that dry microburst occurrence is indeed rare in all regions of the country except the Western Plateau, statistics on wet and dry microbursts will also be computed for the Kansas City, Orlando, and Washington D.C. microbursts.

ACKNOWLEDGEMENTS

The National Climatic Center and personnel at the Memphis, Huntsville, and Denver National Weather Service offices supplied the thunderstorm day data.

REFERENCES

Barab, J.D., K.D. Jaffe, S.R. Marks, and P.J. O'Brien, 1985: Enhanced Low Level Wind Shear Alert System (LLWAS) at Denver, July 5-October 6, 1985. FAA Technical Report DOT/FAA/CT-TN86/12, 165 pp.

Clark, D.A., 1988: Observability of Microbursts with Doppler Weather Radar During 1986 in Huntsville, AL. MIT Lincoln Laboratory Project Report ATC-160, FAA Report DOT/FAA/RD/PS-88/11, 48 pp.

Court, A. and J.F. Griffiths, 1986: "Thunderstorm Climatology", Chapter 2 in Thunderstorm Morphology and Dynamics, ed by E. Kessler, University of Oklahoma Press, Norman, OK, 9-39

Department of Commerce, 1958: History of Observations: Instructions as Applied to Thunderstorms. Meteorological Rec. Doc. 3.12, Washington, D.C.

DiStefano, J.T., 1987: Study of Microburst Detection Performance During 1985 in Memphis, TN. MIT Lincoln Laboratory Project Report ATC-142, FAA Report DOT FAA/PM-87-18, 25 pp

DiStefano, J.T., 1988: Observability of Microbursts Using Doppler Weather Radar and Surface Anemometers During 1987 in Denver, CO. MIT Lincoln Laboratory Project Report ATC-161, FAA Report DOT/FAA/RD/PS-88/12, 102 pp

DiStefano, J.T. and D.A. Clark, 1990: Microburst Observability and Frequency During 1988 in Denver, CO. MIT Lincoln Laboratory Project Report ATC-170, FAA Report DOTFAATS-89 9, 45 pp.

Dodge, J., J. Arnold, G. Wilson, J. Evans, T. Fujita. 1986: The Cooperative Huntsville Meteorological Experiment (COHMEX) Bulletin of American Meteorological Society, 67, 417-419.

Evans, J. and D. Turnbull, 1989: Development of an Automated Windshear Detection System Using Doppler Weather Radar Proc. IEEE, 77, 1661-1673.

Fujita, T.T., 1985: The Downburst - Microburst and Macroburst Department of Geophysical Sciences, University of Chicago, 122 pp

Krumm, W.R., 1954: On the Cause of Downdrafts from Dry Thunderstorms over the Plateau Area of the United States. Bulletin of American Meteorological Society, 35, 122-125.

Martin Marietta Information Systems Group, 1989: Integrated Wind-Shear System Deployment Study, Vol. I. ATC-89-1145, 84 pp

Turnbull, D., J. McCarthy, J. Evans, and D. Zrnic. 1989: The FAA Terminal Doppler Weather Radar (TDWR) Program. Preprints, Third International Conference on the Aviation Weather System. Anaheim, CA, American Meteorological Society, 414-419

Viemeister, P.E., 1961: The Lightning Book. The MIT Press, Cambridge, MA, 316 pp.

Wakimoto, R.M., 1985: Forecasting Dry Microburst Activity Over the High Plains. Monthly Weather Review, 113, 1131-1143.

Weber, M.E. and T.A. Noyes. 1988: Low-Altitude Wind Shear Detection with Airport Surveillance Radars: Evaluation of 1987 Field Measurements. MIT Lincoln Laboratory Project Report ATC-159, FAA Report FAA/PS-88/10, 107 pp.

Williams, E.R., M.E. Weber, and C.D. Engholm, 1989a: Electrical Characteristics of Microburst-Producing Storms in Denver. Preprints, 24th Conference on Radar Meteorology. Tallahassee, FL, American Meteorological Society, 89-92

Williams, E.R., M.E. Weber, and R.E. Orville. 1989b: The Relationship Between Lightning Type and Convective State of Thunderclouds. Journal of Geophysical Research, in print

Williams, E.R., 1989, personal communication.

Wilson, J.W., R.D. Roberts, C. Kessinger, and J. McCarthy, 1984: Microburst Wind Structure and Evaluation of Doppler Radar for Airport Wind Shear Detection. Journal of Climate and Applied Meteorology, 23, 898-915.

Wolfson, M.M., 1989: The FLOWS Automatic Weather Station Network. Journal of Atmospheric and Oceanic Technology, 6, 307-316.

Zorpette, G., 1986: The Menacing Microburst. IEEE Spectrum, November, 50-56.

Aspect Angle Dependence of Outflow Strength in Denver Microbursts: Spatial and Temporal Variations *

Robert G. Hallowell

M.I.T. Lincoln Laboratory

Lexington, Massachusetts 02173

1. INTRODUCTION

MIT Lincoln Laboratory is being sponsored by the Federal Aviation Administration (FAA) to develop and test the Terminal Doppler Weather Radar (TDWR) wind shear surveillance system (Turnbull et al. 1989). As part of this program Lincoln has developed algorithms for automatically detecting microbursts, or thunderstorm outflows using the radial velocity data gathered from a single TDWR. Output from the detection algorithms will be used to warn aircraft of microburst hazards. While the success in automatically detecting microbursts using the Lincoln Laboratory microburst detection algorithm has been encouraging (Merritt et al. 1989), one issue which continues to cause concern is microburst asymmetry. Asymmetry, or aspect angle dependence, in microbursts refers to outflows that have a divergent surface outflow strength or extent that varies depending on the aspect (or viewing) angle of the radar.

The TDWR detection algorithms utilize input from a single Doppler radar; therefore, an asymmetric microburst may be underestimated or go undetected if the radar is viewing the event from an aspect angle where the strength of the outflow is weak. Additionally, the size and location of the event may be distorted when the outflow extent is significantly asymmetric. Most of the present outflow modeling and detection methods are based on the assumption of axial symmetry both in the strength and extent of outflows. Asymmetry in microbursts, therefore, is a major concern for TDWR microburst detection performance.

Past work by Wilson et al. (1984) and Eilts (1987, 1988) has indicated that some microbursts are highly asymmetric, for at least a portion of their lifetime. However, this previous work has been limited in scope to single "snapshots" of the microbursts, generally at their peak outflow strength. Strength asymmetries from these previous studies indicated asymmetry ratios (maximum over minimum strength) ranging from 1.3:1 to as high as 6:1. None of the studies dealt with shape (or extent) asymmetries.

This paper describes the results from a detailed study of 96 individual observations from 27 microburst events. Measurements were taken to determine both the strength and extent of each microburst at multiple aspect angles. The data clearly show that microbursts, on average, have maximum strengths and extents which are 1.9:1 and 1.5:1 asymmetric, respectively.

2. DATA

Single-Doppler radar measurements were collected in Denver during 1987 using the FL-2 S-Band (Lincoln Laboratory) and UND C-Band (University of North Dakota) radars. As shown in Figure 1, the UND radar was located 20.3 km north and 1.6 km east of the FL-2 radar. The radar scanning was coordinated to cover microbursts that occurred in favorable dual-Doppler regions. For each scan of an event, the two-dimensional wind field was calculated using the multiple Doppler radar synthesis system suggested by Brown et al. (1981). Surface dual-Doppler wind fields at 250 meter resolution were synthesized from the radar radial velocity fields. The paired radar scans were all surface tilts (0.3°–0.5°) and had time differences of less than 1 minute. In addition the beam intersection angle of the radars had to be greater than 30° and less than 150° (denoted as the shaded area in Figure 1).

The raw two-dimensional wind fields were then smoothed using 3 iterations of a simple 3-by-3 median filter, with 4 of 9 points required to be valid. This smoothing technique had the advantage of filling some small holes in the data without artificially expanding the analysis region greatly. The 10% trimmed mean wind was then removed. A trimmed mean was used to reduce the impact of erroneous wind values on the mean wind. This final perturbation wind field was used for all analyses.

A wide variety of cases were chosen for this analysis to obtain a representative sample of the microbursts found in the Denver environment (Table 1). The "scans" column in Table 1 indicates the number of observations of a particular event, "peak reflectivity" (surface) is listed to show that
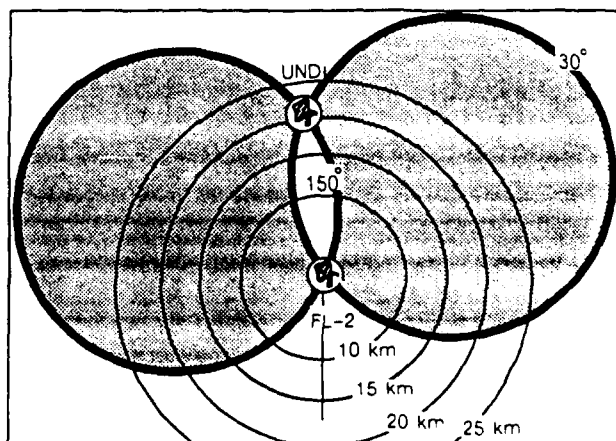

Figure 1. Relative locations of UND and FL-2. Shaded region denotes valid dual-Doppler region.

both "wet" and "dry" microbursts were examined, and the "maximum strength" indicates the largest differential veloc-ity over all the aspect angles and observations of an event.

2.1. Data Accuracy

The accuracy of the strength estimates used in this analysis is on the order of ± 0.5 m/s. However, the layering of polar data to Cartesian grids and the application of a me-dian filter causes a general 15-20% reduction of raw velocity measurements. This reduction is uniform and therefore does not affect the asymmetry statistics presented here. Since the strengths shown here would likely be perceived in raw radar data at slightly higher levels, some weak microburst events (<10m/s) were included in this analysis. Shape estimates have a general accuracy of ± 0.35 km.

Figure 2. *Typical velocity profile through microburst center.*

Table 1. *Denver, Co microburst cases used in asymmetry analysis.*

Date	Case#	Times(UT)	Scans	Peak Reflect. (dBz)	Max Strength (m/s)
7/16	1	2306-2320	5	15	24
	2	2307-2313	4	13	26
7/28	3	2320-2235	8	31	16
	4	2220-2233	8	36	15
	5	2220	1	12	10
	6	2224	1	34	16
	7	2241-2243	3	49	16
	8	2248-2250	3	54	24
	9	2256-2257	2	49	18
7/31	10	2251	1	4	17
	11	2251-2256	5	43	10
	12	2252-2256	4	38	8
	13	2255-2301	6	38	13
	14	2259-2300	2	35	10
8/2	15	2243-2247	5	28	10
	16	2247-2257	11	33	13
	17	2252	1	10	12
8/6	18	2025-2030	6	16	10
	19	2026-2029	4	16	11
9/3	20	2135-2145	3	31	14
	21	2145	1	13	10
	22	2145	1	5	15
	23	2150-2200	3	27	18
	24	2200-2205	2	20	15
	25	2200	1	0	8
9/4	26	2015-2018	2	23	15
9/11	27	0258-0308	3	56	24

3. ANALYSIS METHODOLOGY

Figure 2 illustrates the velocity trace along a line seg-ment passing through the center of a microburst. The seg-ment between the start and stop arrows indicates a region where the radial velocity is generally increasing (i.e., a re-gion of positive or divergent shear). To find these regions of divergent microburst outflow, the perturbation wind field was examined visually, and a bounding polygon was subjec-tively drawn around each microburst region.

In general, the sides of the polygon were drawn to enclose the region of positive shear discussed above. The shape of the polygon was used to determine the outflow ex-tent of the microburst, and was therefore important in the calculation of microburst shape statistics. The polygons for isolated microbursts (single distinct outflows) were fairly easy to define. Complicated multi-cell or line microbursts, such as those discussed by Hjemfelt (1985), were much harder to define using a single polygon. Consequently, only the portions of the overall flow which had distinct edges
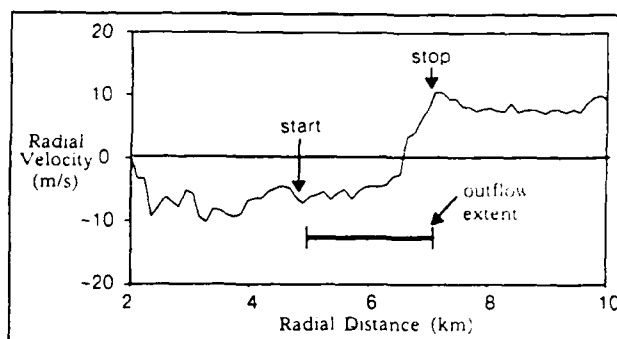
(surrounded by regions of convergence) were identified and analyzed for multi-cell and line microbursts.

Once an event was drawn, the velocity difference across every unique gridpoint pair within the polygon was calculated, taking into account the relative aspect angle of the segment. Note that the differential velocity measurement was calculated between two points; no shear threshold was set for the intervening points. The strength calculations were only performed on points whose connecting lines were com-pletely contained within the defined polygon. It was assumed that points within the polygon were generally divergent be-cause the sides of the polygon limit the strength analysis to the microburst outflow region.

The relative aspect angle of the line formed by each pair of gridpoints was determined by placing a fictitious ra-dar 15 km from the centroid of the polygon. As shown in Figure 3, the radar which has a beam parallel to the test segment within the polygon (thick line on figure) defines the aspect angle of that segment. In the example shown the as-pect angle of the segment is 130° (relative to the event poly-gon, not the radar).

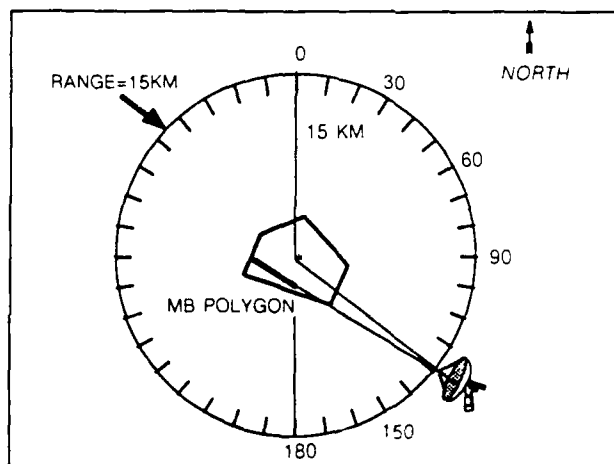Figure 3. *Diagram illustrating relative aspect angle calculation for asymmetry analysis.*

Differential velocity and shape measurements were obtained from all possible aspect angles and then grouped into one of eighteen aspect angle categories. The categories ranged from 0°±5°(due North), to 170°±5° in ten degree steps. Aspect angles over 180° were not considered because they generally reflect measurements made from 0°-180°

18

(though not exactly due to the way relative aspect angles were calculated). Other statistics such as mean wind and peak reflectivity (magnitude, extent and location) were also measured.

4. TYPES OF ASYMMETRY

The TDWR system is designed to identify the location and size of a microburst and estimate the maximum differential velocity of the event. Figure 4 shows the dual-Doppler wind field for a microburst that is nearly symmetric in strength and shape. A Doppler radar would find roughly the same strength, location, and size for this event, regardless of its viewing angle. This is the kind of symmetry which, in general, is currently assumed to exist for all microbursts. However, there are primarily two types of asymmetry that may occur in microbursts: strength and shape.

4.1. Strength Asymmetry

The strength asymmetry of an event is measured by estimating the largest differential velocity within the microburst outflow at multiple aspect angles. Differential velocity is the magnitude of the wind change between any two points within the event. The severity of the aspect angle dependence for strength in an observation may be measured by dividing the maximum strength by the minimum strength over all aspect angles. A strength asymmetry ratio of 1.0 would indicate a microburst perfectly symmetrical with respect to strength. The observation shown in Figure 4 has a strength asymmetry of only 1.3:1 (20m/s ÷ 15m/s).

A single-Doppler radar will, in general, underestimate the maximum strength of a microburst strongly asymmetric in strength. The dual-Doppler wind field shown in Figure 5 reveals a microburst with a strength asymmetry ratios of 2.3:1. The differential velocity trace over all aspect

angles is given in the graph directly above the wind field. Figure 6 shows the contours of radial velocity for a radar viewing from the maximum strength aspect angle (0°) and located 15 km from the centroid of the event shown in Figure 5. Similarly, Figure 7 shows the radial velocity contours for a radar radially aligned with the angle of weakest strength (90°). Note that the velocity field from the peak viewing angle indicates a strong shear region with a peak velocity differential of 24.3 m/s. The radial velocity field from the weak viewing angle, on the other hand, yields a weak radially skewed velocity couplet with peak radial velocity of only 10.4 m/s. The "skewed couplet" is a common occurrence in any asymmetric microburst; unfortunately, it may occur at any aspect angle (not just the minimum strength angle) and therefore gives little insight on the true asymmetry of the event (Eilts 1988).

4.2. Shape Asymmetry

The shape asymmetry of an event is measured by estimating the largest spatial extent of the microburst outflow at multiple aspect angles. The shape of an event (outflow extent) is measured by estimating the cross-distance from one end of the outflow polygon to the other at a variety of aspect angles. The level of aspect angle dependence for outflow extent is calculated by dividing the largest cross-distance by the smallest cross-distance over all aspect angles. The event shown in Figure 4 has a shape asymmetry of 1.2:1 (5.5km ÷ 4.5km).
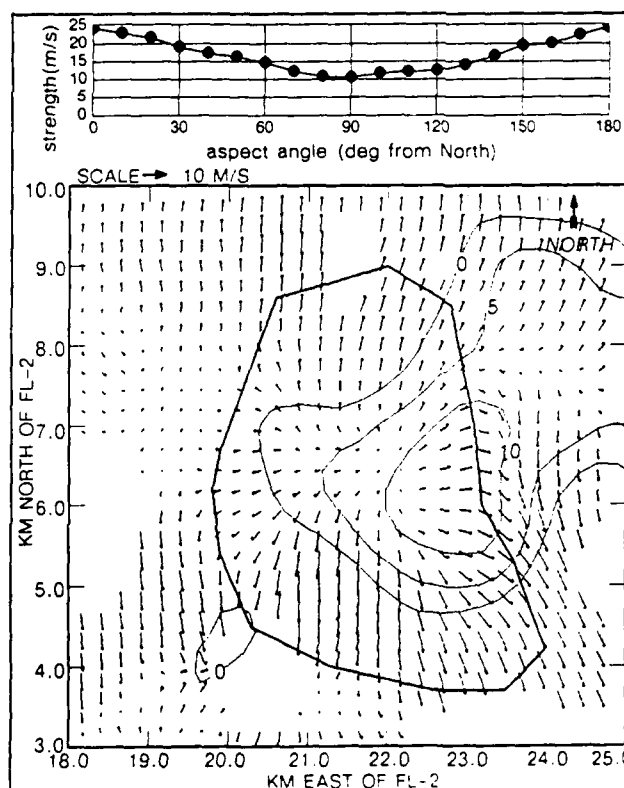
Figure 5. Graph (top) indicating variation of measured strength with aspect angle. Dual-Doppler wind field (bottom) for a shape and strength asymmetric microburst on July 16, 1987 at 23:07:41 UT. Polygon for event shown in center, contoured lines are of reflectivity at 0, 5, and 10 dBz.
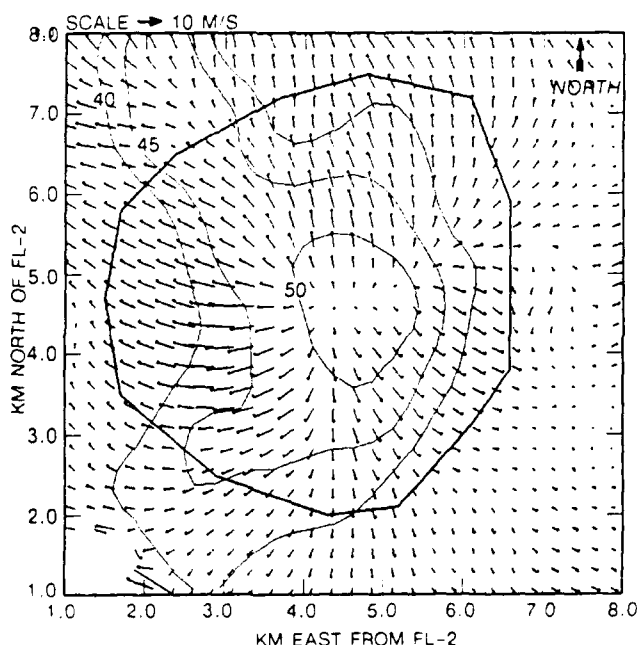

Figure 4   Dual-Doppler wind field for a shape and strength symmetric microburst on July 25, 1987 at 22:48:27 UT. Polygon for event shown in center, contoured lines are of reflectivity at 40, 45, and 50 dBz.

Figure 6. Contours of the radial velocity field (1m/s intervals) extracted from dual-Doppler wind field in Figure 5 relative to a fictitious radar located at a range of 15 km and an azimuth of 0°.

Figure 7. Contours of the radial velocity field (1m/s intervals) extracted from dual-Doppler wind field in Figure 5 relative to a fictitious radar located at a range of 15 km and an azimuth of 90°

A highly aspect-angle-dependent outflow shape makes it difficult to capture the shape, and sometimes central location, of the microburst using a single-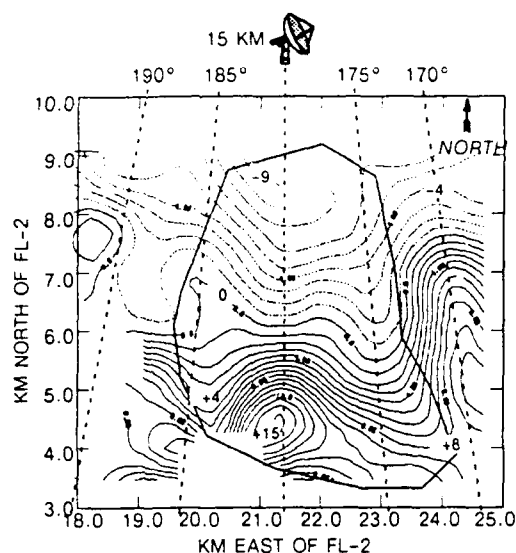Doppler radar. For example, the observation in Figure 5 has a shape asymmetry of 1.7:1. If we reexamine the radial velocity fields shown in Figure 6 and Figure 7, we see differences in not only the strengths of the fields, but also the location of the peak strengths. Further, the extent of the event (searching for radials where the strength is a fixed percentage of the peak at that angle) is significantly different in size and shape. Part of this difference is caused by the strength asymmetry, but a major portion is caused by the elongated physical shape of the outflow.

5. CHARACTERISTICS OF ASYMMETRY

The characteristics of asymmetry may be divided into two categories: general and event lifetime. The general characteristics are compiled using all the observations listed in Table 1. Lifetime characteristics are based only on the events in Table 1 having more than 4 scans of the event.

5.1. General Characteristics

The events chosen for this analysis were randomly chosen from those available during 1987 Denver operations and, as such, the distribution of maximum event strengths is similar to that found by Biron & Isaminger (1988). The maximum and minimum strengths for each observation are shown in Figure 8. The aspect angle dependence of strength for all events is between 1.3:1 and 3.8:1, with a median value of 1.9:1. As shown in Figure 9, this cumulative probability does not change significantly between weak (thin solid line) and moderate-strong (dotted line) events.

The maximum and minimum outflow extents for each microburst observation are shown in Figure 10. Shape asymmetry ratios for all events range from 1.1:1 to 2.4:1, with a median value of 1.55:1. As for strengths, the cumulative frequency of shape asymmetry ratios, as shown in
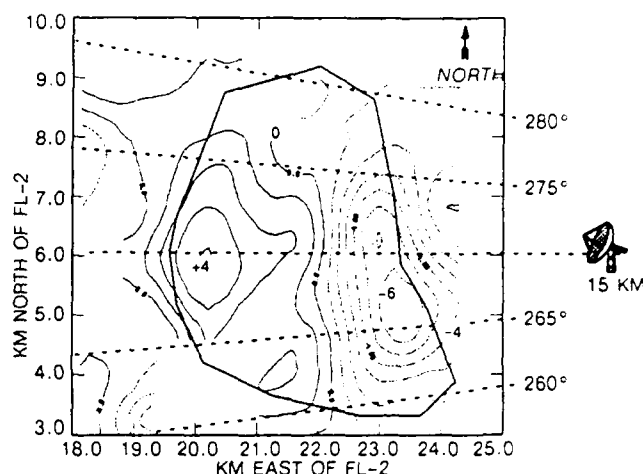
Figure 11, does not vary significantly between weak (thin solid line) and moderate-strong (dotted line) events

Figure 9 and Figure 11 (and further statistical analyses not discussed here) indicate that the maximum strength of an event has little or no correlation with the degree of the strength or shape asymmetry. Additionally, the two forms of asymmetry are statistically unrelated. High or low strength asymmetry ratios are equally as likely to have high or low shape asymmetry ratios and vice-versa. None of the microbursts parameters (mean wind speed, peak reflectivity, strength, etc.) analyzed during this study showed significant correlation to the strength or shape asymmetry of individual observations.

In most instances, the azimuth angles of the maximum strength and extent showed no preferred orientation with respect to the environment or each other. The exception to this was for those events with both high strength (>2.3) and shape (>1.75) asymmetry ratios, for which orientation angles tended to be co-located (i.e., the peak strength occurred along the largest cross-distance). However, the lim-
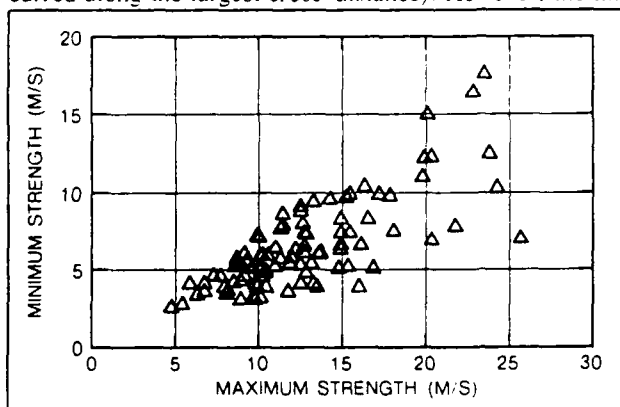

Figure 8. Scatter diagram illustrating spread of maximum and minimum strengths for each observation.
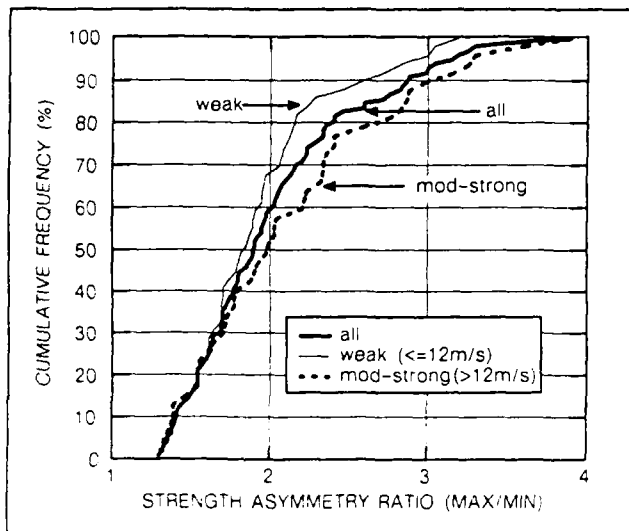
20

Figure 9. Cumulative frequency of strength asymmetry ratios for various maximum strength classes
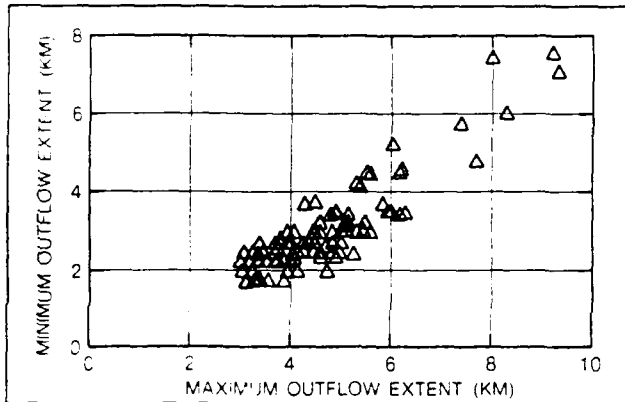

Figure 10. Scatter diagram illustrating spread of maximum and minimum outflow lengths for each observation.
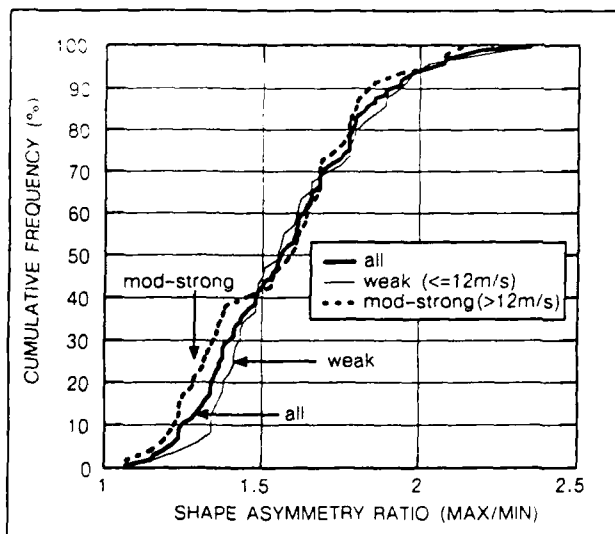

Figure 11. Cumulative frequency of shape asymmetry ratios for various maximum strength classes.

ited number of cases which met this criteria makes the reliability of this correlation uncertain.
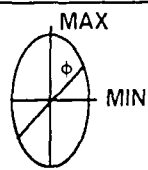
5.2. Lifetime Characteristics

There were only seven events which had more than 4 dual-Doppler scans, and were thus suitable for analysis of lifetime characteristics. This is a limited data set, but large enough to provide some estimate of the broad changes in asymmetry over an event's lifetime.

The orientation angle of both the maximum strength and maximum cross-distance remains relatively constant ($\pm 10°$) over the lifetime of the microburst. This is important in that a radar which is viewing an asymmetric event from an unfavorable angle (with respect to strength) will continue to underestimate the strength of the event unless it moves into a more favorable position. At a range of 15 km, an event would need to move approximately 3 km to change the viewing angle by 10° (assuming motion is not directly away from or toward the radar). For the seven event lifetimes analyzed, the microbursts traveled a total distance (based on the polygon centroid) of between 1 and 5 km. This small movement would not likely be sufficient to obtain a more favorable viewing angle.

The magnitude of the strength or shape asymmetry for isolated events tended to remain stable throughout the event's history. However, environmental influences (other microbursts, gust fronts, minor divergences) appeared to cause significant fluctuations in the magnitude of the asymmetry over time.

6. INDICATIONS OF ASYMMETRY

The assumption has generally been made that microbursts are symmetric events. The data presented here clearly indicate that this is not the case. Perhaps a better representation of microburst strength and shape is an ellipse (formed by the maximum and minimum strength or extent of the event). If an ellipse were used to represent microburst outflows, then a parameter P (strength or shape) may be predicted at any aspect angle ϕ using the formula in Figure 12.

$$P_\phi = \frac{MAX}{\sqrt{\left(\left(\frac{MAX}{MIN}\right)^2 - 1\right) SIN^2(\phi) + 1}}$$

Figure 12. Formula for the elliptical distribution of strength and shape parameters.

This formula was applied to all the microburst observations. Figure 13 shows a scatter diagram of the measured strength versus the strength predicted with this formula for all observations and aspect angles. The overall correlation for all aspect angles was 0.92 for strength and 0.96 for shape (not shown). The angle between the maximum and minimum strength orientation angles is 70°-90° in over 70% of the cases, and the same was true for cross-distances. An elliptical representation of microburst strength and shape parameters gives a surprisingly good fit over a wide range of strengths and extents.

21

A non-aspect angle dependent measure of the orientation of this ellipse would clearly be helpful. As noted earlier, none of the parameters examined in this analysis were found to indicate the orientation or degree of the asymmetry. In most cases, asymmetry appeared to be a function of the location of the microburst relative to other microbursts or weak divergence regions. Strong outflows would push into weak outflows, thereby distorting the flow of the weaker event. Observationally, isolated microbursts appear to be more symmetric than line or multiple microbursts. However, even isolated microbursts have some asymmetry which appears to be, in part, a function of the complexity of the environmental flow.

7. FUTURE WORK

While the analysis presented above is sufficient to describe microburst asymmetry in Denver's unique weather environment, microbursts from other regions of the country should also be examined. The TDWR testbed from which the data were taken operated in Kansas City, MO during 1989, and is currently operating in Orlando, FL. These data should be examined for asymmetry to confirm or modify the results presented here.

The point-to-point method of calculating differential velocity, while simple to implement and efficient to use, requires the assumption that intervening wind data points are divergent. Careful scrutiny of both the wind fields and event polygons helps to reduce any potential analysis problems. In the future, however, it may be beneficial to search for line "segments" within the polygon which have generally positive shear along their length.

Finally, the mechanism for creating asymmetry needs to be understood. The environmental flow, proximity and orientation to other events, and even the topography of the land underlying microburst may be a factor. A thorough analysis of the interaction of microbursts with their surrounding environmental flow would be worthwhile. A comparison of Denver, CO (sloping terrain) and Orlando, FL (flat wetlands) may yield some insight on the effect of terrain on asymmetry.

8. SUMMARY & CONCLUSIONS

Over 27 events encompassing 96 total observations of microbursts were examined for asymmetry. There were two types of asymmetry which were studied: strength and shape. The median strength and shape asymmetry ratios, for the cases presented here, were 1.9:1 and 1.55:1, respectively. The representation of microbursts as symmetric flows is clearly inaccurate.

The magnitude of the shape and strength asymmetry ratios were found to be independent of the magnitudes of the maximum cross-distance (shape) and strength measurements. No preferred orientation angles were found for maximum strength or shape, although the orientation angles did remain relatively stable throughout the lifetime of the events.

Based on these findings, a single-Doppler radar has an equal chance of viewing a microburst of all sizes and strengths from any random aspect angle. Therefore, the radar will underestimate the overall maximum strength of the event, on average, by approximately 30% (based on median strength asymmetry ratio of 1.9:1). The primary cause of asymmetry (or at least fluctuations in its magnitude) in microbursts appears to be the proximity of other wind shear events (gust fronts, microbursts, or weak divergences). There appear to be no reliable, single Doppler-radar based measurements (reflectivity, peak radial strength, mean wind, etc.) which indicate the severity or orientation of asymmetry in microbursts.

REFERENCES

Biron, Paul J., and Isaminger, Mark A., 1989: An analysis of microburst characteristics related to automatic detection from Huntsville, AL and Denver, CO. Preprints, 24th Conference on Radar Meteorology, Tallahassee, FL, American Meteorological Society, pp. 269-273.

Brown, et al., 1981: Multiple Doppler radar analysis of severe thunderstorms: designing a general analysis system. NOAA Technical Memorandum ERL-NSSL-92.

Eilts, Michael D., 1988: Use of a single Doppler radar to estimate the runway to wind shear component in microburst outflows. 26th Aerospace Sciences Meeting Paper, Jan., 1988, American Institute of Aeronautics and Astronautics, AIAA-88-0694.

Eilts, Michael D., and Doviak, Richard J., 1987: Oklahoma downbursts and their asymmetry. Journal of Climate and Applied Meteorology, vol. 26, pp. 66-78.

Hjemfelt, M.R., and Roberts, R.D., 1985: Microburst lines. Preprints, 14th Conference on Severe Local Storms, Indianapolis, Indiana, American Meteorological Society, pp. 297-300.

Merritt, Mark W., et al., 1989: Wind shear detection with pencil-beam radars. The Lincoln Laboratory Journal, Volume 2, Number 3, pp. 483-510.

Turnbull, D., J. McCarthy, J. Evans, D. Zrnic', 1989: The FAA Terminal Doppler Weather Radar (TDWR) program. Preprints, 3rd International Conference on the Aviation Weather Systems, Anaheim, CA, pp. 414-419.

Wilson, et. al., 1984: Microburst wind shear and evaluation of Doppler radar for airport wind shear detection. Journal of Climate and Applied Meteorology, vol. 23, pp. 898-915.
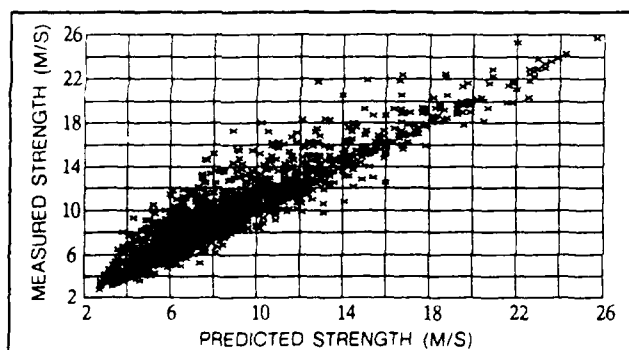
Figure 13. Scatter diagram of predicted strength (using elliptical model) vs. measured strength for all observations and aspect angles.

OBSERVED DIFFERENCES BETWEEN DENVER AND KANSAS CITY GUST FRONTS AND THEIR IMPACT UPON THE PERFORMANCE OF THE GUST FRONT DETECTION ALGORITHM *

Diana Klingle-Wilson and Michael F. Donovan

M.I.T. Lincoln Laboratory

Lexington, Massachusetts 02173

1. INTRODUCTION

The Terminal Doppler Weather Radar (TDWR) testbed radar (known as FL-2) collected data near Denver's Stapleton Airport during 1988 and near the Kansas City International Airport (MCI) during 1989. One objective of the TDWR Program is to detect gust fronts and their associated wind shifts. This information can be used by an Air Traffic Control (ATC) supervisor to plan runway changes and for warnings of potentially-hazardous gust front-related wind shears to arriving and departing pilots. This function is performed by the gust front detection algorithm.

An ongoing assessment of the performance of the current TDWR gust front algorithm is necessary to ensure that the algorithm performs consistently in different environments. Such assessments were performed after the 1988 TDWR Operational Test and Evaluation in Denver and after the 1989 operational season in Kansas City. This paper presents a comparison of gust front characteristics such as length, duration, strength, and propagation speed and direction that occurred in Denver and Kansas City and a comparison of algorithm performance at each location.

In the following, the term **gust front** refers to the leading edge of the thunderstorm outflow throughout its life cycle. A gust front **event** is a single observation of a gust front (on a radar volume scan) by the National Severe Storms Laboratory (NSSL) ground-truth analyst.

2. GUST FRONT CHARACTERISTICS

In order to compare the frequency of gust front occurrence in Denver and Kansas City, gust fronts during the months of June, July, and August in Denver in 1988 and in Kansas City in 1989 were tabulated. Although FL-2 operated outside these months at both locations, only these months of operation were common to both demonstrations. The distribution of these gust fronts is provided in Figure 1. More gust fronts were observed in Denver (133) than in Kansas City (49) during this three-month period. In Denver, the month of peak gust front activity was July, while in Kansas City August was the month of peak activity.

Gust front strength is determined by the change in Doppler velocity (ΔV) across the gust front. The strength of a gust front is defined as "weak" for $5 \text{ m/s} \leq \Delta V < 10 \text{ m/s}$; "moderate" for $10 \text{ m/s} \leq \Delta V < 15 \text{ m/s}$; "strong" for $15 \text{ m/s} \leq \Delta V < 25 \text{ m/s}$; and "severe" for $\Delta V \geq 25 \text{ m/s}$. The percent of gust front **events** in each strength category are

Figure 1. Number of observed gust fronts during the months of June, July, and August at Denver (1988) and Kansas City (1989)
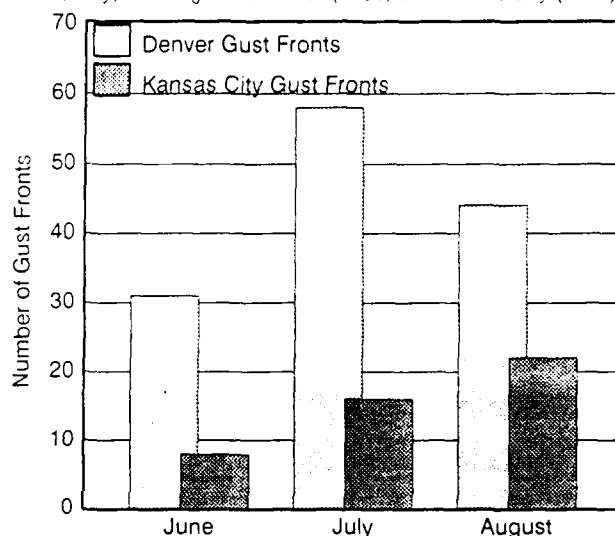
shown in Figure 2. Kansas City gust events were stronger than Denver gust events.

The distribution of lengths of gust front events is provided in Figure 3. Denver gust fronts tend to be shorter than Kansas City gust fronts. The average gust front length for Denver and Kansas City was 29 km and 31 km, respectively.

Figure 2. Percent of gust front events in each strength category
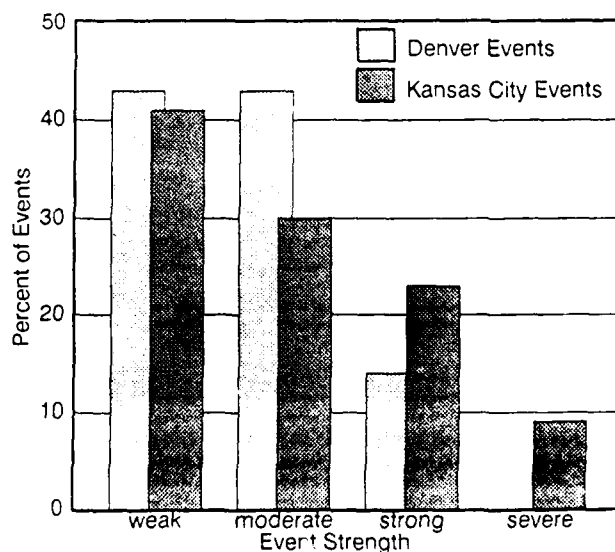
23

Figure 3. Percent of gust front events in each length category. The values on the ordinate are the midpoints of the intervals.

Figure 5. Percent of Gust Fronts in each propagation speed category. The values on the ordinate are the midpoints of the intervals.
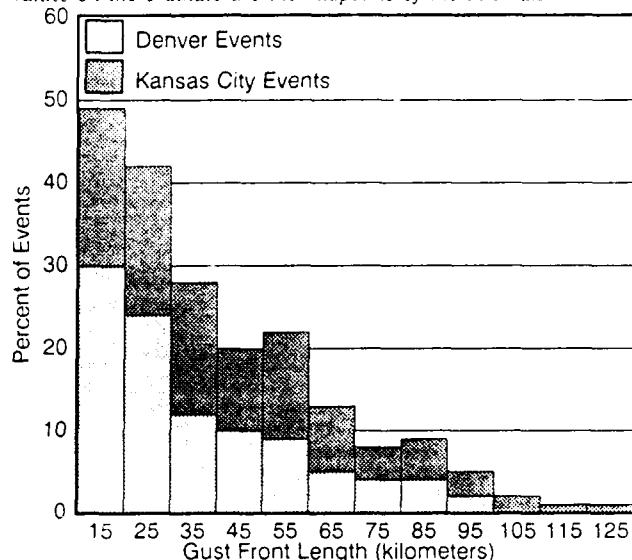
Seventy-seven Denver (1988) and 66 Kansas City (1989) gust fronts were chosen from the complement of gust fronts for analysis of duration and propagation. The distribution of gust front duration is shown in Figure 4. About

Figure 4. Percent of gust fronts in each duration category. The values on the ordinate are the midpoints of the intervals.
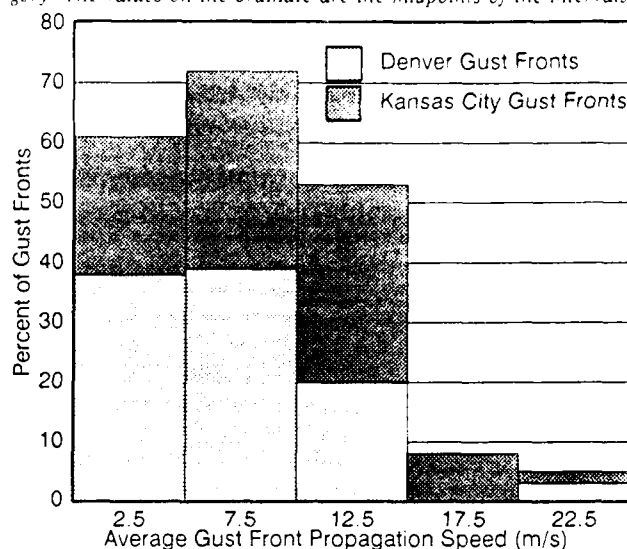
Figure 6. Percent of gust fronts in each propagation direction category.

82% of Kansas City gust fronts had durations of less than 60 minutes, as compared to 52% of Denver gust fronts. The mean duration of Denver and Kansas City gust fronts was 71 and 42 minutes, respectively. Thus, Denver gust fronts are longer-lived than Kansas City gust fronts.

The distribution of gust front propagation speed is shown in Figure 5., which indicates that Kansas City gust fronts propagated faster than Denver gust fronts. The average propagation speed of Denver and Kansas City gust fronts was about 7 m/s and 10 m/s, respectively.

The distribution of the direction toward which the gust front propagated is given in Figure 6. In both Denver and Kansas City, the preferred direction of propagation was from the northwest quadrant to southeast quadrant.
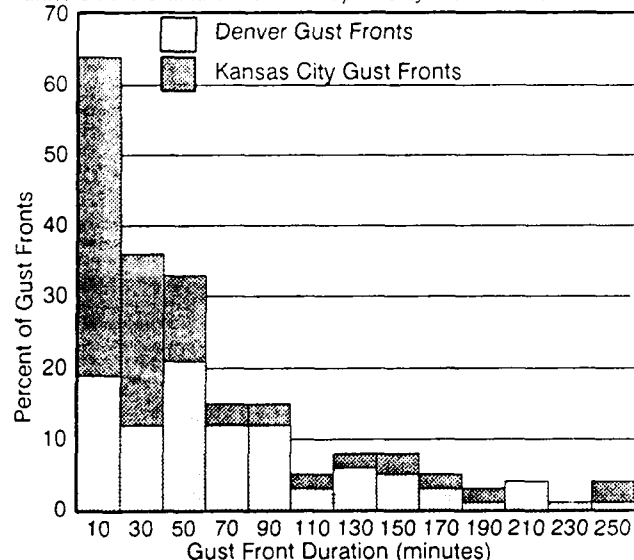
3. GUST FRONT/WIND SHIFT DETECTION AND PREDICTION PERFORMANCE

The gust front algorithm serves two functions: warning and planning. Wind shear hazard warnings are issued when a gust front impacts the runways or within 3 miles of the ends of the runways. The alarm message consists of the type of hazard (wind shear for gust fronts), the location and expected gain in wind speed (e.g. wind shear alert, 35 knot gain, one mile final). The planning function consists of alerting an Air Traffic Control Supervisor when a change in wind speed and/or direction due to a gust front at the airport is imminent. A description of the algorithm and an assessment of its performance during the 1988 Denver operational demonstration are found in Klingle-Wilson, et al., (1989), Merritt, et al. (1989), and Smith, et al., (1989).

3.1. Warning Performance

The ability of the algorithm to produce timely, useful warnings rests upon its ability to detect convergent shears in the Doppler velocity data. Two basic statistics were used

to quantify detection performance: Probability of Detection (POD) and Probability of False Alarm (PFA). These statistics are defined as:

$$POD = \frac{detected\ events}{total\ events}$$

$$PFA = \frac{false\ alarms}{correct\ alarms + false\ alarms}$$

An event is a single observation (on a volume scan) by the NSSL ground-truth analyst of a gust front in the radar data. A detected event is an algorithmic declaration of a gust front that overlaps ground truth. A false alarm is an algorithmic declaration that does not overlap ground truth. Only those gust fronts that are located within 60 km of the radar are truthed and scored. In general, it is more important to detect the stronger gust fronts since they represent the greatest hazard to aviation. For that reason, the following discussion deals only with gust fronts of moderate or greater strength.

3.2. Gust Fronts Within 60km of the Radar

POD, for all truthed gust fronts (of moderate or greater strength) as a function of gust front strength, for 1989 Kansas City is shown in Table 1. (ALL refers to all

Table 1.   Probability of Detection

	MODERATE	STRONG	SEVERE	ALL	PFA
1988	73%	91%	100%	78%	2%
1989	72%	81%	92%	77%	13%

gust fronts of moderate or greater strength.) Corresponding POD results from the 1988 Denver operational demonstration are provided for comparison. In general, there is little difference in performance between 1988 and 1989. The largest POD differences are in the strong and severe categories. However, one must take care in interpreting the POD for severe gust fronts since there was only one severe event during 1988.

The POD does not indicate how well a gust front is detected. One measure of the goodness of the detection is the percent of the length of the event that is detected by the algorithm. The average Percent of Length Detected as a function of gust front strength is given in Table 2.

Table 2.   Average Percent of Length Detected

	MODERATE	STRONG	SEVERE	ALL
1988	66%	69%	73%	67%
1989	59%	61%	50%	60%

For the 1988 Denver and 1989 Kansas City data, the Probability of False Alarm (PFA) was 2% and 13% respectively. A common producer of false alarms in Kansas City was the vertical shear in the horizontal wind (i.e., winds increasing, decreasing, or veering with height). This change of wind with height produced an apparent convergence in the Doppler velocity field that was detected by the gust front algorithm. In addition, the locations of these regions were roughly equal to the range of the airport from the radar, resulting in false warnings to pilots. Techniques for discriminating vertical wind shear-induced false alarms are under investigation at NSSL.

A second source of false alarms was ground clutter that was not completely removed by the clutter residue editing process. Since ground clutter exhibits a near-zero Doppler velocity, a false convergence is created by winds

blowing against clutter. This was observed on the bluffs surrounding the Missouri River.

3.3. Gust Fronts at the Airport

The gust front algorithm estimates the wind shear hazard associated with each gust front and issues a warning if the gust front is over the airport. The warning is composed of two parts, the location of the wind shear and the intensity. A warning is viewed as correct only if the gust front alarm is issued for the appropriate location along a runway center line. The probability of correctly locating the wind shear event is determined by computing the number of wind shear alerts issued at the airport divided by the number wind shear alerts that should have been issued. The results of this analysis for 1988 (Denver) and 1989 (Kansas City) are shown in Table 3. It is important to note that the ability

Table 3   Probability of Correctly Detecting Wind Shear at Airport

	MODERATE	STRONG	SEVERE	ALL	PFW
1988	64%	86%	-	70%	0%
1989	29%	68%	40%	45%	40%

to correctly locate wind shear over MCI is significantly less than over Stapleton. The reason for this is the location of the radar relative to the respective airports.

The primary cause of missed detections was inadequate convergence in the radial direction. Because the algorithm detects only radial convergence, it is easier to detect gust fronts that are oriented perpendicular to the radar beam. As gust fronts move closer to the radar, less of their lengths are oriented perpendicular to the beam, making them more difficult to detect. An example of the loss of detection of a gust front as it moves over the radar is given in Figure 7. The locations of the Stapleton and MCI airports

Figure 7.   Example of the loss of a gust front detection as the gust front passes over the radar. The rectangles represent ground truth and the solid lines represent detections. MCI is located northeast of the radar, DEN is located northwest of the radar.
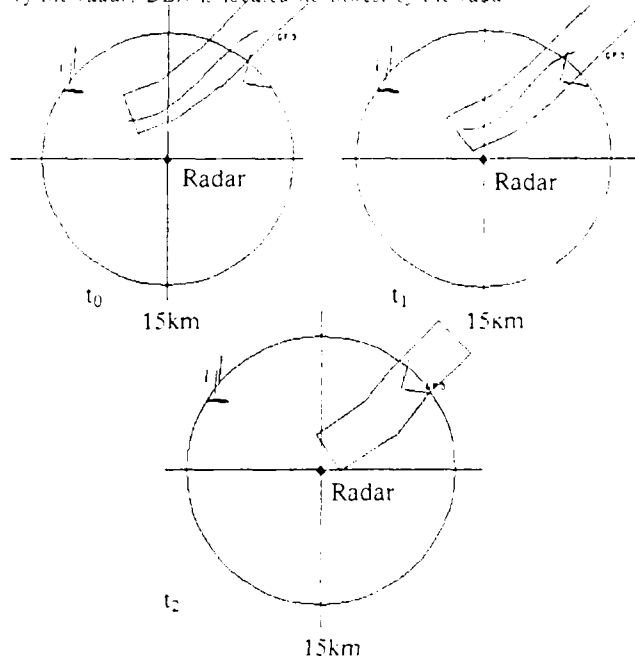
relative to FL-2 are shown.

25

The preferred propagation direction for gust fronts at both locations was northwest to southeast. If one assumes that gust front orientation is perpendicular to propagation direction, then the preferred gust front orientation is northeast to southwest. In Denver, Stapleton Airport was located to the northwest of FL-2 and therefore most gust fronts that passed over Stapleton were oriented perpendicular to the radar beam and the probability of detecting them was quite good. However, when those gust fronts moved too close to the radar (*i.e.*, overhead) the detections were lost.

In Kansas City, MCI was located northeast of FL-2 with the result that most of the gust fronts that impacted MCI were oriented parallel to the beam. In addition, those gust fronts typically passed over the radar at the same time they were impacting the airport. Therefore, the probability of detecting gust fronts over MCI and issuing warnings to pilots was small. The ability to detect reflectivity thin lines and/or azimuthal shears is essential in cases where the TDWR radar site is unfavorable with respect to the local gust front climatology.

The Probability of False Warning (PFW) is defined as the number of false alarms issued divided by the total number of alarms issued. For Kansas City 1989, the PFW was 40% versus 0% for Denver 1988. The Kansas City false warnings were due entirely to vertical shears in the horizontal winds over the airport.

The accuracy of the wind shear intensity estimates is scored by comparing the intensity expressed in the alert to pilot reports as logged by observers in the tower. For 1989 and 1988, the average difference between pilot reports and alerts was about 15 kts, with alerts overestimating wind shear relative to pilot reports.

The number of pilot reports available for the analysis of the wind shear hazard estimate is quite small (less than 10). There is some evidence in the literature (Wolfson, 1990) that suggests that the wind shear hazard associated with a gust front may not be appropriately characterized by the simple calculation used in the algorithm. From 1986 through 1989, the UND Citation aircraft performed a number of gust front penetrations. These data will be analyzed to determine if the gust front wind shear hazard estimation algorithm should be refined.

3.4. Planning Product Performance

Runway management is improved with the TDWR by alerting an Air Traffic Control (ATC) Supervisor when a wind shift is expected at the airport (forecasted location) and the winds that will result after the gust front passage (wind shift estimate). The forecasted location is scored by determining if a forecast overlaps the truth region for the time at which the forecast is valid. If so, a valid forecast is declared. There are two type of errors in forecasts: forecasts whose locations do not agree with the ground truth (a missed forecast) and forecasts for gust fronts that no longer exist (a false forecast). Forecasts are made for 10 and 20 minutes into the future. The statistics for evaluation of the performance of the forecasting function are the Probability of a Correct Forecast (POCF) and Probability of False Forecast (PFF) and are given by:

$$POCF = \frac{number\ of\ valid\ forecasts}{number\ of\ events\ forecasted}$$

$$PFF = \frac{number\ of\ false\ forecasts}{number\ of\ (forecasted\ events\ +\ false\ forecasts)}$$

POCF, as a function of gust front strength, is given in Table 4. For Denver (1988), the PFF for the 10 and 20

Table 4. Probability of Correct Forecast

	MODERATE	STRONG	SEVERE	ALL	PFF
	1988				
10 MIN	97%	98%	100%	97%	11%
20 MIN	82%	84%	-	83%	18%
	1989				
10 MIN	95%	100%	67%	97%	18%
20 MIN	95%	93%	100%	94%	21%

minute forecasts was 11% and 18%, respectively. For Kansas City (1989) the PFF for the 10 and 20 minute forecasts was 18% and 21%, respectively. Forecasts were generated only about 56% of the time. The high POCF values show that, when generated, forecasts were very accurate.

The accuracy of the wind shift estimate is determined by comparing the wind shift estimate to the mesonet data. The average absolute difference in wind speed and direction between the wind shift estimate and the mesonet data was 3 m/s and 30°, respectively. The wind shift speed was, on the average, about 2 m/s larger than that determined from the mesonet data and the wind shift direction was about 5° counterclockwise of the mesonet wind direction. These results are nearly identical to the 1988 Denver results.

4. CONCLUSIONS

A comparison of the gust fronts that occurred at each location shows significant differences in gust front characteristics. Although Kansas City gust fronts were fewer in number, they tended to be stronger, longer, faster-moving, and shorter-lived than Denver gust fronts.

In general, there was no significant difference (between Kansas City and Denver) in the ability of the algorithm to detect gust fronts within 60 km of the radar. However, the ability of the current algorithm (which uses only radial convergence) to generate wind shear hazard warnings at MCI was less than at Denver. There appears to be a preferred gust front orientation (northeast to southwest) in both Denver and Kansas City. Stapleton airport was located northwest of FL-2 and gust fronts moving over the airport were perpendicular to the beam. MCI was located northeast of FL-2 and gust fronts over MCI were aligned along the radar beam. The incorporation of reflectivity thin line and/or azimuthal shear detection into the gust front algorithm would improve detection capability in cases of unfavorable viewing angle.

5. REFERENCES

Klingle-Wilson, D., S. Olson, W. Wilson, W. Mahoney, S. Smith, A. Witt and M. Eilts, 1989: Gust Front Detection Algorithm for the Terminal Doppler Weather Radar: Part 2, Performance Assessment, *Preprints, 3rd Int'l Conf. on the Aviation Weather System*, Anaheim, CA. (#p10.27), pp. 398-402.

Merritt, M. W., D. Klingle-Wilson, and S. Campbell, 1989: Wind Shear Detection with Pencil-Beam Radars, *The Lincoln Laboratory Journal*, v. 2(3), pp. 483-510.

Smith, S.D., A. Witt, M. Eilts, D. Klingle-Wilson, S. Olson, J. Sanford, 1989: Gust Front Detection Algorithm for the Terminal Doppler Weather Radar: Part 1, Current Status, *3rd Int'l Conf. on Avia Wea. Sys.* (# 1.6), pp 31-34.

Wolfson, M. M., 1990: Understanding and predicting microbursts, PhD thesis, Massachusetts Institute of Technology, Cambridge, MA, 303 pp.

A COMPARISON OF ANEMOMETER AND DOPPLER RADAR WINDS
DURING WIND SHEAR EVENTS*

Margita C. Liepins, Marilyn M. Wolfson, David A. Clark, and Barbara E. Forman

M.I.T. Lincoln Laboratory

Lexington, Massachusetts 02173

1. INTRODUCTION

The Federal Aviation Administration (FAA) currently uses the anemometer-based Low Level Wind Shear Alert System (LLWAS) as the primary method of wind shear detection at major U.S. airports. With the upcoming deployment of the Terminal Doppler Weather Radar (TDWR) system (Turnbull et al. 1989), potential methods for integrating the two systems are being investigated. By integrating, the advantages of both sensor systems can be utilized. Advantages of the LLWAS ground sensor network include true wind direction measurements, a high measurement frequency, a lack of sensitivity to clear air reflectivity, and few false alarms from radar point targets such as planes, birds, etc. Advantages of the radar include complete scan coverage of the region of concern, the ability to predict events, fewer terrain problems such as sheltering which can reduce the wind speed readings, and almost no false alarms due to non-hazardous wind shear such as thermals.

The objectives of this study are to gain a clearer understanding of the basic relationship between the wind information provided by these two very different sensing systems, and to determine the impact this relationship may have on integration of the two operational systems. A proposed mathematical technique for "correcting" LLWAS winds where needed to better match radar winds is evaluated for cases of microburst (divergent) and gust front (convergent) wind shear.

2. THE STUDY

In this study we use a large base of Doppler radar and anemometer data to determine a numerical relationship between the respective wind measurements. This relationship is influenced by:

1. Actual wind differences within the sampling spaces used by the two sensors. These include differences due to sampling height, and effects of local anemometer obstructions (both sheltering and channeling of wind).

2. Effects resulting from the different sensing methodology, or from physical characteristics of the actual sensors.

A number of studies have been conducted to measure the change of wind speed with height by mounting wind sensors on meteorological towers or on existing television tow-ers. In general, a power law has been found to best describe the wind profile in the frictional boundary layer (e.g. Joffre 1984). This profile is generally dependent on the temperature lapse rate and ground roughness (Haltiner and Martin 1957). For this study, we chose to use the power law profile to represent the winds measured by the anemometer and radar since it provides for a nonlinear solution that accounts for the inherent difference in sampling height. The power law profile is stated:

$$U / U_1 = (Z / Z_1)^p \qquad (2.1)$$

where U and U_1 represent the wind speeds at heights Z and Z_1 respectively and $0 \leq p \leq 1$. The exponent p is empirically derived by comparing a large number of radar and anemometer wind values measured during a variety of wind shear events. In our case p is dependent not only on the lapse rate and ground roughness, but on the inherent differences in the two sensors.

3. METHODOLOGY

3.1 Data

Doppler weather radar and surface anemometer data were collected during 1988 in Denver, CO as part of the FAA TDWR measurement program and operational demonstration. Doppler wind measurements were collected with an S-Band radar (FL-2) developed and operated by Lincoln Laboratory (Evans and Turnbull 1989), while surface ane-
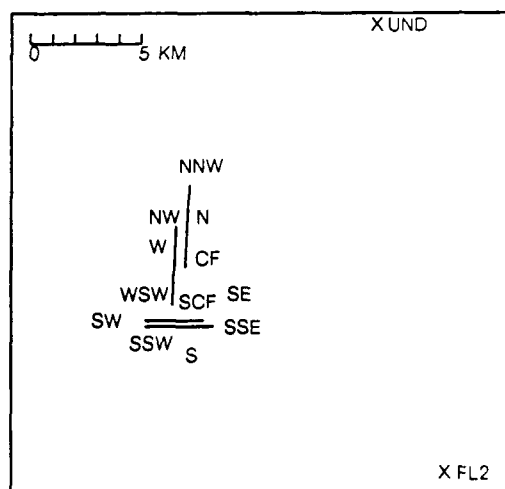

Figure 1. The 1988 LLWAS network at Stapleton International Airport in Denver, CO. The runways are denoted by the two pairs of straight lines. UND and FL-2 radar locations are indicated (X) in the upper and lower right corners respectively.

mometer wind measurements were collected from twelve LLWAS sensors situated in the vicinity of Denver's Stapleton International Airport. Dual-Doppler data were created using the University of N. Dakota C-Band radar (UND) and FL-2 (Figure 1).

Twelve cases were chosen to include a variety of meteorological events and wide range of radar reflectivity values. Cases included gust fronts, microbursts, areas of divergence, and areas of widespread strong winds that occurred from mid-May to mid-August, and covered time periods of approximately one-half to two hours each (Table 1).

3.2 Comparing Radar and Anemometer Winds

Doppler wind measurements were taken from the lowest elevation scan (either 0.3° or 0.4°) which typically updated at a rate of approximately once per minute. A signal-to-noise ratio (SNR) threshold of 6 dB was applied to reduce noisiness in the data. Doppler (radial) velocity measurements were then read from the radar gate closest in range and azimuth to each LLWAS station location, and from the eight surrounding gates. The radar gate size was 120 m in the radial direction and varied from approximately 200 m to 300 m azimuthally depending upon radar range. The median Doppler velocity value from the nine gates was then used for comparison with the corresponding radial component of LLWAS wind, provided at least four of the gates were not flagged as "bad data", or empty due to SNR thresholding. This filtering reduced the effect of gates which were contaminated with ground clutter or point targets.

LLWAS wind measurements are made every 6-7 seconds, so insignificant as well as significant wind fluctuations

were recorded. Cornman et al. (1989) defined a "significant fluctuation" model as an objective basis for identifying wind shear events. The most recent automated LLWAS wind shear detection algorithm (Cornman and Wilson 1989; UCAR 1990) attempts to eliminate insignificant fluctuations by applying a running weighted mean filter covering approximately 60-90 seconds in time. A similar approach was taken here, except the values included in the 1 minute average were evenly weighted.

The height of the center of the radar beam above the surface anemometer ranged from approximately 150 m to 250 m. The heights above ground level of the 12 LLWAS anemometers are shown in Figure 2 . In 1988, they ranged
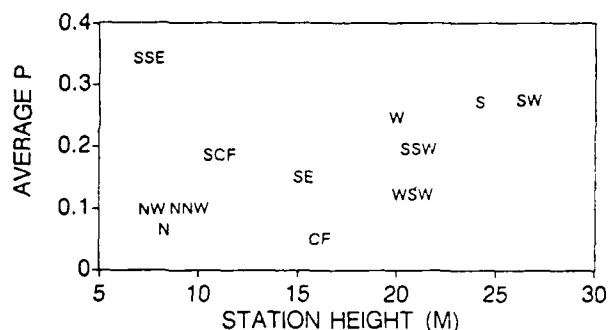

Figure 2 .   Plot of the average value of the exponent p versus station height.

from 7.6 m to 26.8 m. (Some anemometer heights have since been raised to reduce sheltering.)

Table 1.   Chart showing the date, description, reflectivity, Doppler wind speed range, and number of data points for each case. The number of data points refers to the average number of valid radar data points per station with SNR > 6 dB, suitable for comparison with LLWAS data. [* denotes case where 46% of the radar data containing the wind shear event were invalid after SNR thresholding and much of the valid data was just above threshold. Data from this case were not used in the study.]

DATE (1988)	DESCRIPTION	DBZ	WINDS m/s	# DATA POINTS
10 MAY 19:15-21:00	widespread rain, solid wind field	25 - 30	-10 -> +2	48
18 MAY 21:00-22:00	multi-cell storm with some divergence, turns into a line storm	up to 60	-12 -> +7	34
09 JUN 20:50-22:15	weak widespread cells	20 - 30	+2 -> +7	54
09 JUN 23:30-23:59	widespread winds, convergence line	up to 35	-12 -> +12	17
25 JUN 20:00-20:40	line storm moving westward, gf at N end of the network	up to 50	-15 -> +5	26
07 JUL 00:00-01:00	10 km storm cell	up to 55	0 -> +10	42
11 JUL 22:00-23:00	region of widespread rain, strong microbursts in the SE corner of the network	up to 40	-12 -> +7	41
16 JUL 22:00-23:59	10 km cellular storm moves N to S divergent line at 22:50, microburst 23:08-23:35	20 - 55	-15 -> 0 -12 -> +12	84
17 JUL 21:35-22:00	compact 10 km line cell	10 - 25	-15 -> -10	51
29 JUL 22:30-23:59	isolated 5 km cells over the network, turns into a line storm by 23:50	up to 55	+5 -> +12.5	50
09 AUG 18:30-20:00	microburst located in the N end of the network	up to 15	+10 -> -15	0*
21 AUG 88 21:15-22:00	cellular storm at the S end of the network becomes widespread winds	40 - 45 up to 30	0 -> +5 -5 -> -8	30

28

3.3 Derivation of Power Law Exponent

The power law profile provides a model of the atmospheric boundary layer by which the relationship between radar and surface wind measurements may be assessed. Referring to Eq. (2.1), values for p were calculated for each LLWAS station by using the Doppler velocity as U, the radial component of the LLWAS wind as U_1, the height of the radar gate above the LLWAS station as Z, and the height of the LLWAS station above the ground as Z_1. Data from the twelve cases provided 5773 values of p for the 12 stations.

From this data set, the probability density versus the value of p was plotted. The plots yielded an approximately normal distribution for each station (see Figure 4), as measured by the χ^2 goodness-of-fit test. The mean value of p and the standard deviation were calculated for each station. These values are shown in Table 2, and also indicated in Figure 4 .

Table 2.   Statistical data from derivation of power law relationship for twelve LLWAS stations.

station	$\bar{p}$	σ	$\bar{p} -1/2\sigma$	multiplier $(z/z_1)^p$ implied by:	
				$\bar{p}$	$\bar{p} - \sigma/2$
CF	0.050	0.139	-.020	1.10	0.95
SCF	0.186	0.142	0.109	1.51	1.37
W	0.246	0.126	0.183	1.49	1.53
NW	0.100	0.109	0.039	1.29	1.14
NNW	0.101	0.175	0.012	1.27	1.04
N	0.069	0.120	0.009	1.19	1.03
SE	0.152	0.169	0.067	1.37	1.19
SSE	0.340	0.235	0.223	2.40	2.07
S	0.270	0.264	0.138	1.46	1.34
SSW	0.196	0.144	0.124	1.36	1.32
SW	0.277	0.263	0.146	1.44	1.34
WSW	0.126	0.192	0.001	1.22	1.00

3.4 Discussion of results

We found a large variation for the twelve stations, and a significant range of variances as well. Wind speeds measured at stations CF and N are most representative of the radar wind speed, with near-zero $\bar{p}$ values implying an excellent anemometer exposure. Station SSE shows the most difference, with $\bar{p} = 0.4$. Notice also how low the variance of the p distribution is for this station; the wind speeds measured at SSE are always too slow. This may indicate the need to raise the anemometer or replace the bearings. The large $\bar{p}$ values at stations S, SW, and W also imply a large difference between the LLWAS and radar wind speeds. There appears to be little correlation between the variability of $\bar{p}$ with either the height of the LLWAS station (Figure 2) or its distance from the radar (Figure 3). The measured differences can be fairly confidently attributed to anemometer exposure and sensor maintenance at the different LLWAS sites.

4.   APPLICATION

The representation of the difference in measured wind speed between the radar and LLWAS with a power law profile provides a useful method for "adjusting" the LLWAS speed to some radar height equivalent. For a constant radar height, e.g. the average height of the lowest tilt over the LLWAS network, the adjustment to the LLWAS speed becomes linear for an individual station, represented by $(Z / Z_1)^p$. Statistically, this would yield an overestimate with respect to the radar equivalent wind speed 50% of the time.

For practical application, it is prudent to take a more conservative approach and reduce the power law exponent by some amount dependent upon the variance of p for a particular station. For instance, reducing $\bar{p}$ by one standard deviation would reduce the probability of overestimation to 16%. This, however, would also reduce the adjustment to a negligible amount. Since analysis of the error variance of the sample data indicated that a large portion of the overestimated winds were associated with low wind speed values, it would seem reasonable to take an intermediate approach and reduce the exponent by one-half standard deviation. This appears to provide a reasonable wind speed adjustment with a sufficiently low percentage of overcorrection (30%).

Table 2 also includes the multiplication factors for adjustment of LLWAS wind speeds to a radar equivalent, using both the $\bar{p}$ and $\bar{p} - \sigma/2$ as the exponent in the power law relationship, and a typical radar scan height of 200 m.

4.1 Microburst Case Study

In order to observe the potential impact of the LLWAS wind adjustment, we applied it to data from a strong microburst event which affected flight operations at Stapleton Airport on 11 July 1988 (Schlickenmaier 1989). The microburst developed as a series of pulses along a line to the east and south of the east-west runways from 2206-2221 UTC. Figure 5 shows LLWAS wind plots at two instances during the microburst period. Figure 5 (a) (2209:22 UTC) shows the location of two main pulses (labeled A and B) along the microburst line. The locations of these pulses were determined through analysis of single- and dual-Doppler radar data, and supplemental surface anemometer data. By 2211:21 UTC [Figure 5 (b)], a third pulse (C) is identified near station SSE. Pulse B ultimately provided the strongest shear, as radar data indicated more than 80 knots of headwind loss to the east of the east-west runways. The shear from this pulse, however, was beyond the range of the LLWAS network and not fully sensed by the anemometer system.
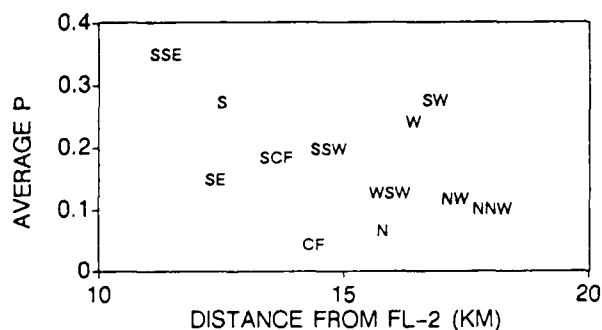

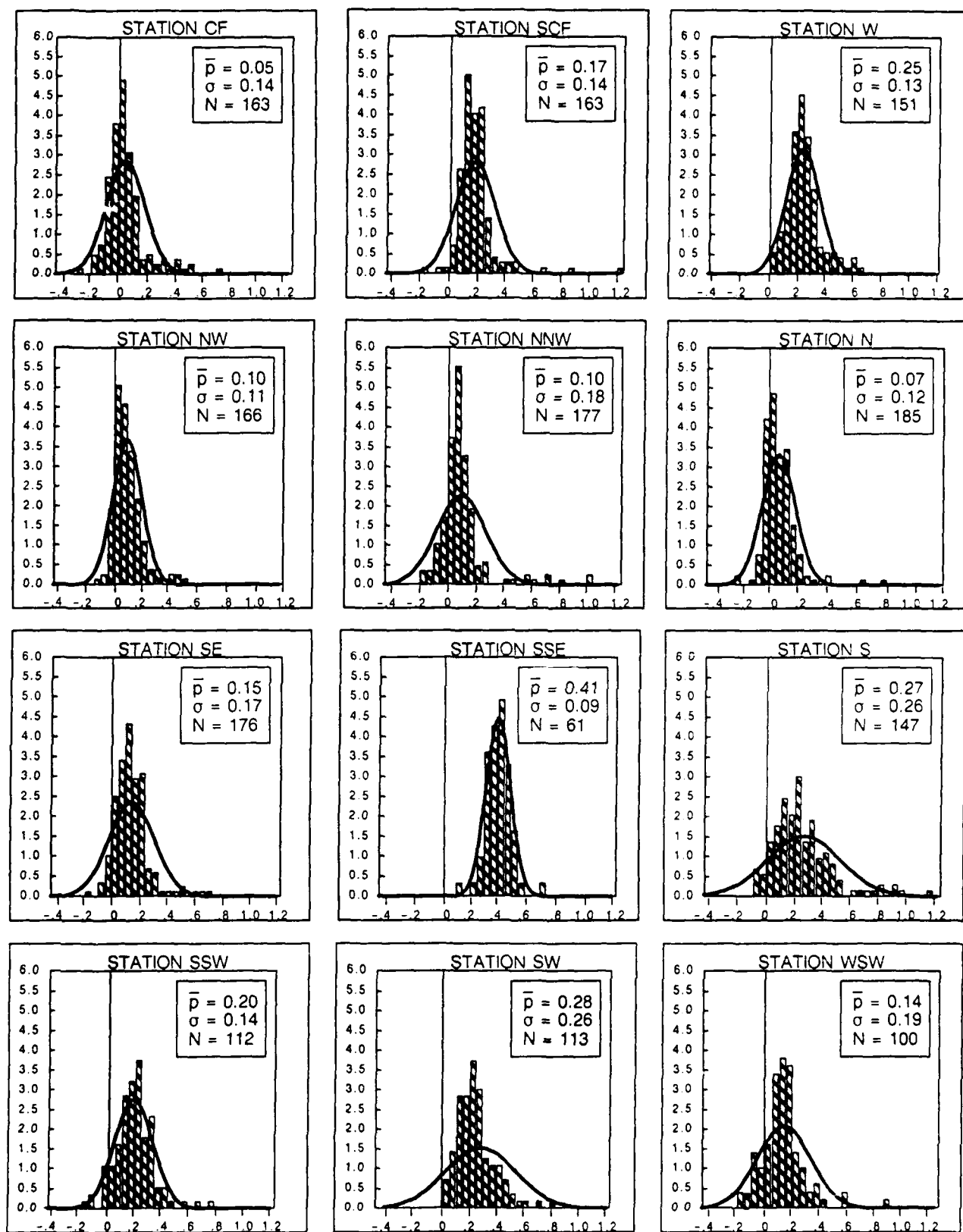*Figure 3 .   Plot of the average value of the exponent p versus station distance from the FL-2 radar.*

Figure 4. Histogram plots of the probability density of p for each station where $\bar{p}$ is the value of the power law profile exponent, σ is the standard deviation, and N is the total number of data points used to determine the distribution.
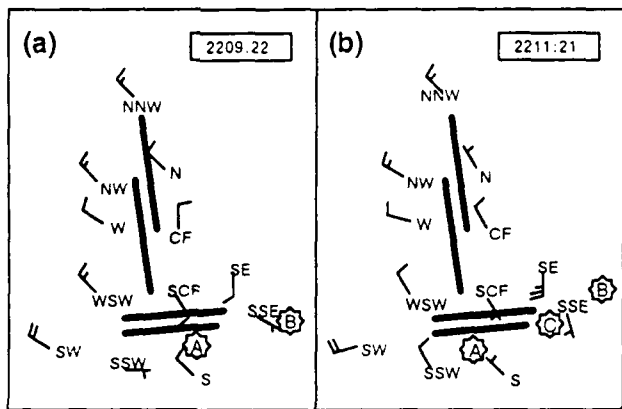
30

Figure 5 . LLWAS winds for 11 July 1988 at a) 2209:22 UTC and b) 2211:21 UTC. One full barb represents 10 m/s. Runways are denoted by bold straight lines. Positions of main microburst pulses are lettered A, B, and C.

The LLWAS winds (adjusted and unadjusted) were compared with wind vectors from dual-Doppler radar data, with particular attention to those stations affected by the microburst, namely SE, SSE, SCF, S, and SSW. The LLWAS wind speeds were adjusted to a height of 200m above ground

level (the approximate average height of the low-elevation tilts over the network), conservatively applying the power law by reducing the empirical value of $\bar{p}$ by $\sigma/2$. The adjustment of the LLWAS wind speed made it more consistent with the dual-Doppler wind, *prior to the microburst*. However, once the microburst winds began to affect a station, the LLWAS wind speed was *greater* than that from dual-Doppler data, and the adjustment of the LLWAS wind actually increased the difference in wind speed as measured by the two systems.

Two examples of this overcorrecting are shown in Figure 6 . At station SSE, the adjustment to the LLWAS wind speed makes it more consistent with the dual-Doppler speed up until 2208 UTC, at which time there is a spike in the wind speed resulting from the nearby microburst. For the next few minutes, the LLWAS speed is either equal to or greater than that measured from dual-Doppler data, and the adjustment of the LLWAS wind results in a greater difference from the dual-Doppler wind. A similar affect is seen at Station SE [Figure 6 (b)], as the third pulse in the microburst caused a wind speed spike shortly after 2210 UTC, at which time the LLWAS wind speeds generally exceed the radar speeds. A possible explanation for this overcorrecting is discussed in section 4.3.

4.2 Gust Front Case Study

On 17 July 1988 a strong gust front traversed the LLWAS network shortly after 2130 UTC with the strongest component of wind oriented radially with respect to the FL-2 radar. Unlike the previous microburst case in which the strong winds developed impulsively from a downdraft directly over the LLWAS network, the strong winds here propagated over the network from the northwest. Figure 7 shows both the unadjusted and adjusted radial component wind speed traces for two LLWAS stations as compared to the radar-measured wind.

For Station SSE, statistical analysis yielded a significant adjustment for the LLWAS wind speed (Station SSE has the highest adjustment factor). It can be seen in [Figure 7 (a)] that this adjustment to the LLWAS wind speed is successful in bringing the LLWAS winds closer to the radar winds. In the case of station SCF [Figure 7 (b)], where statistical analysis yielded a much smaller adjustment to the LLWAS winds, the results are very similar to Station SSE in that the LLWAS wind estimate is greatly improved. LLWAS winds are not overcorrected in either case.

4.3 Discussion

The overcorrection by the empirical power law relationship during the microburst (divergent) wind shear event may be explainable by the deviation from the typical vertical wind profile within the lower boundary layer during a microburst [Figure 8 (a)]. As the microburst reaches the ground, its downward momentum locally perturbs the vertical wind profile, and the horizontally divergent wind results in a very thin layer of very high wind speeds near the ground. In contrast, the boundary layer wind profile in a gust front [Figure 8 (b)] conforms better to that modelled with an average power law profile. Also, the radar measurement of wind over a pulse volume in this case more nearly equals
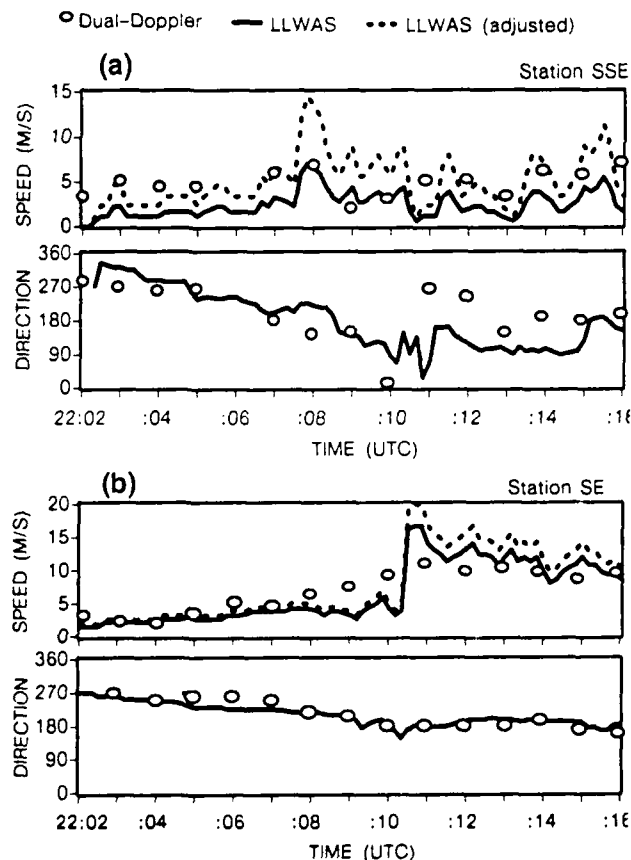

Figure 6 . Time series plots of wind speed and direction for LLWAS (solid line), adjusted LLWAS (dashed line), and dual-Doppler synthesized winds (circles) for LLWAS stations a) SSE and b) SE during a microburst event.
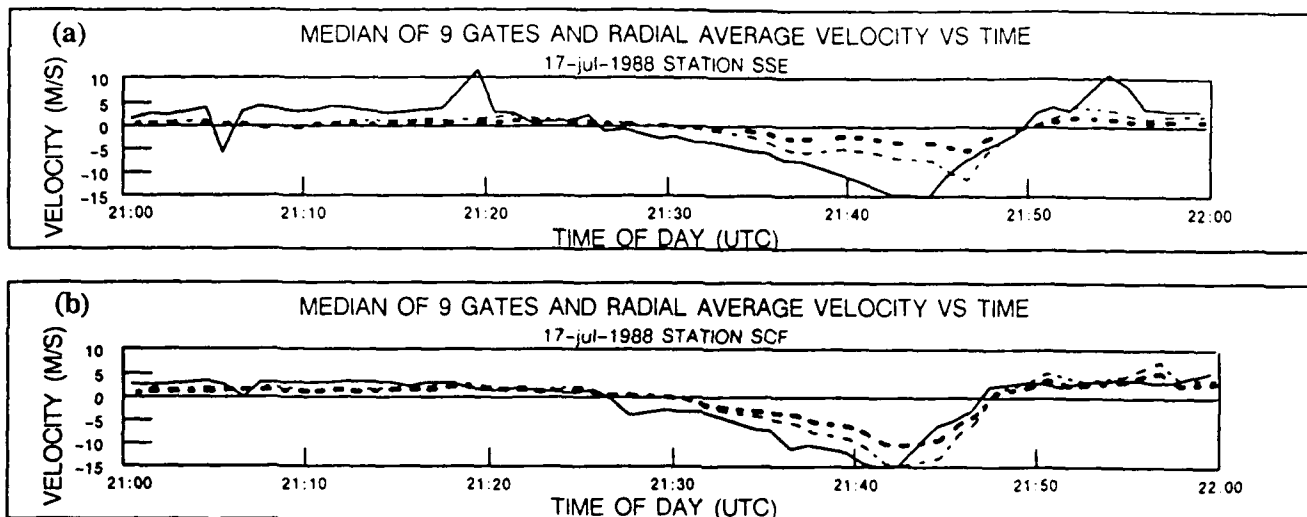
31

(a) MEDIAN OF 9 GATES AND RADIAL AVERAGE VELOCITY VS TIME
17-jul-1988 STATION SSE

(b) MEDIAN OF 9 GATES AND RADIAL AVERAGE VELOCITY VS TIME
17-jul-1988 STATION SCF

Figure 7 . Plot of radial component of wind speeds with respect to FL-2 as measured by radar (solid line), LLWAS (bold dashed line), and adjusted LLWAS (dashed line) at location of LLWAS stations a) SSE and b)SCF.
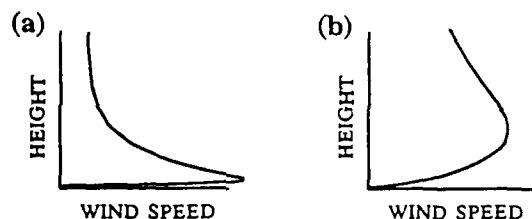

Figure 8 . Schematic illustration of wind speed profile for surface conditions a) with strong divergent wind shear, and b)strong persistent straight line winds.

a point measurement, because the wind speed variations with height are smaller.

5. CONCLUSIONS

It has been found that wind speed measurements by surface anemometers and by Doppler radar were, in general, quite comparable over the Denver 1988 LLWAS network for a set of 11 days with appreciable weather. We used the exponent p from the power law shown in Eq. (2.1) as an indicator of the correlation between surface and radar wind speeds. In Figure 4 it can be seen that the highest probability density of p occurs fairly close to zero for most of the stations. Such p values imply the need for little or no correction of surface wind speeds. A few of the stations (i.e. SSE, S, W, and SW) show higher p values. These higher values are most likely the result of poor anemometer siting or a mechanical problem with the sensor. The best solution would be to resite or raise the anemometer, but this is not always possible. The possibility of providing the necessary correction numerically using the power law profile was evaluated.

A closer look at the data reveals that during microburst conditions, where a strong downdraft results in a horizontal spreading of air close to the surface, the two sensors

yield equivalent speeds. During such events the application of a wind speed correction factor is not necessary and could result in the overestimation of ground wind speeds. In the case of a gust front, however, where winds are generally parallel to the surface and penetrate the surface boundary layer to a lesser extent, the comparison between the two sensors is not as good. It has been shown that in these cases the application of a correcting factor can make LLWAS winds more comparable to Doppler radar winds.

6. REFERENCES

Cornman, L.B., P.C. Kucera, M.R. Hjelmfelt, and K.L. Elmore, 1989: Short time-scale fluctuations in microburst outflows as observed by Doppler radar and anemometers. Preprints, 24th Conference on Radar Meteorology, Tallahassee, FL, Amer. Meteor. Soc., 150-153.

Cornman, L.B., and F.W. Wilson, Jr., 1989: Microburst Detection from Mesonet Data. 3rd International Conference on the Aviation Weather System, Anaheim, CA, 35-40.

Evans, J.E., and D.H. Turnbull, 1989: Development of an automated windshear detection system using Doppler weather radar. Proc. IEEE, 77, 1661-1673.

Haltiner, G.J., and F.L. Martin, 1957: Dynamical and Physical Meteorology. McGraw-Hill, New York, 228-233.

Joffre, S.M., 1984: Power laws and the empirical representation of velocity and directional shear. J. Appl. Meteor., 23, 1196-1203.

Schlickenmaier, H.W., 1989: Windshear Case Study: Denver, Colorado, July 11, 1988. FAA Report No. DOT/FAA/DS-89/19, 552 pp.

Turnbull, D., J. McCarthy, J. Evans, D. Zrnic', 1989: The FAA Terminal Doppler Weather Radar (TDWR) program. Preprints, 3rd International Conference on the Aviation Weather System, Anaheim, CA, Amer. Meteor. Soc., 414-419.

University Corporation for Atmospheric Research, 1990: Network Expansion LLWAS Algorithm Specification.

32

VERTICAL REFLECTIVITY PROFILES: AVERAGED STORM STRUCTURES AND APPLICATIONS TO FAN-BEAM RADAR WEATHER DETECTION IN THE U.S. *

Seth W. Troxel and Cynthia D. Engholm

M.I.T. Lincoln Laboratory

Lexington, Massachusetts 02173

1. INTRODUCTION

The FAA is deploying over 100 next generation airport surveillance radars (ASR-9) at selected major airports across the country. Like previous ASRs, the ASR-9 utilizes dual broad elevation fan beams (Figure 1) along with a rapid scan rate (12.5 RPM) to exercise its primary function of detecting aircraft over a 60 nmi radius. In addition, the ASR-9 has a separate dedicated weather reflectivity channel which allows air traffic controllers to display quantitative precipitation intensity reports corresponding to the NWS six-level intensity scale on their PPI display. The 30 second update rate of the weather channel coupled with the large sample volume swept by the ASR-9 fan-beam combine to provide timely and useful indications of precipitation intensity within the terminal airspace.

The PPI display of precipitation intensity which is presented to the air traffic controller is essentially a 2-D (R,θ) representation of the 3-D (R,θ,ϕ) reflectivity field sampled by the fan-shaped beam of the ASR-9. Since the antenna gain varies with elevation angle (Figure 1), the parameter reported by the ASR-9 weather channel represents a beam-weighted, vertically averaged estimate of storm intensity. Previous research has shown that the vertically integrated reflectivity automatically reported by fan-beam radars such as the ASR-9 correlates well with estimates of vertically integrated liquid water content (VIL), a useful meteorological parameter which is a measure of overall storm intensity. (Dobson, et al., 1978, Alaka, et al., 1979). Dobson found a linear relationship between VIL and fan-beam reflectivity from 30 to 60 dBZ assuming the beam is filled with precipitation (see discussion in Section 4).

If the beam is non-uniformly or only partially filled with precipitation, then the inherent vertical integration introduced by the fan-beam may cause an underestimation of the storm intensity. This beam filling loss is most acute at long range, where the vertical extent of the beam intercepts more than 10 km of altitude. The magnitude of this error depends on the complex interaction between the vertical reflectivity structure of the storm and its interception by
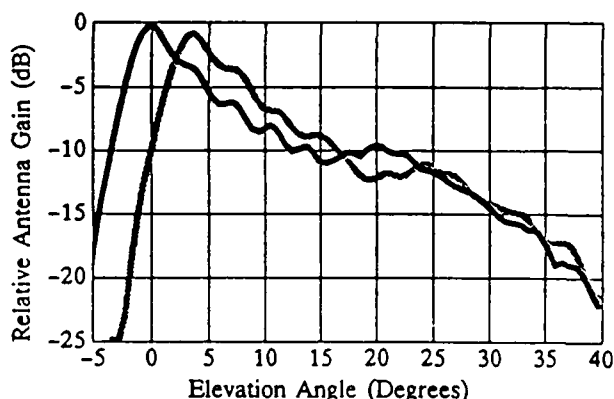

Figure 1. ASR-9 antenna pattern in the principal elevation plane. Black curve is low beam; gray curve is high beam. Plot is for a 0° elevation antenna tilt.

the fan-shaped beam. If the shape and altitude extent of the vertical reflectivity profile (such as could be provided by a pencil-beam radar) are known, then a suitable adjustment can be calculated and applied to the fan-beam reflectivity estimate in order to produce the desired reflectivity report.

The six-level weather thresholds are stored in processor memory for each range gate as functions of receive beam (high or low). The thresholds can be adjusted to compensate for beam filling losses. The adjustments initially implemented in the ASR-9 were derived using a reflectivity profile model which assumes the maximum reflectivity of the storm is distributed constantly from the surface up to 4 km, and then falls off at 3 dBZ per km above 4 km. The success of the reflectivity correction depends on how well the model profile matches actual storm profiles. If regional variations in general storm morphology are significant, then different beam filling loss correction models may need to be developed for specific regions. Understanding the significance of these regional variations in storm vertical reflectivity structure and their impact on ASR-9 weather report accuracy provided the motivation for this study.

2. METHOD

2.1. Overview

Volumetric pencil-beam radar data from selected sites in the continental U.S. were used to construct vertical profiles of reflectivity from which VIL, echo tops and bases, and mean reflectivity profiles were calculated. The pencil-beam data were also used to construct the vertical profile maximum projection Z_{max} — a useful 2-D reflectivity representation for air traffic control purposes in summertime convective storms. Z_{max} represents a conservative report of storm intensity and is indicative of the worst conditions which may be encountered by an aircraft at any altitude. There may be situations in which the Z_{max} parameterization is not appropriate. For example, Z_{max} would be overly sensitive to profile peaks caused by bright-band effects. A bright band is an enhanced reflectivity layer occurring in the region of ice-to-water phase change, usually not indicative of vigorous vertical motions.

A simulation facility was developed which calculates the equivalent ASR-9 fan-beam reflectivity estimate for a reflectivity profile positioned at any range from the radar (see Section 2.4). By using this facility, we were able to assess the amount of adjustment in the ASR-9 reflectivity estimates required to produce the desired Z_{max} reflectivity product.

2.2. Site Selection

In order to examine regional variations in precipitating cloud systems, the continental U.S. was divided into five regions : East (E), Florida and South Plains (S), Midwest (M), High Plains (HP), and West (W) (Figure 2). Digital
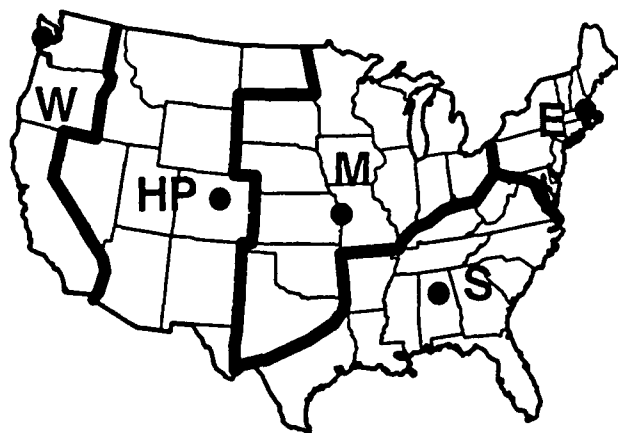

Figure 2.   ASR-9 Beam Filling Loss Storm Model Regions.

radar data recorded during previous field experiments using radars operated by MIT Lincoln Laboratory (FL-2), MIT Center for Meteorology and Physical Oceanography, and NCAR (CP-3) were obtained for one representative site from each region. The sites selected were: Denver, Colora-

do; Kansas City, Missouri; Huntsville, Alabama; Boston, Massachusetts; and Seattle, Washington.

2.3. Construction of Vertical Reflectivity Profiles

Each radar volume scan consisted of a series of full-circle or sector PPI scans containing between 5 and 20 elevation tilts. Selected azimuth sectors of these volume scan data were mapped onto a cylindrical coordinate grid having a range radius of 111 km and a height of 20 km. Azimuthal and range granularity were matched to those of an ASR-9 — 1.41° and 0.926 km respectively — while vertical granularity was 0.5 km. A profile cylinder generated from a full-circle volume scan could therefore contain as many as 30,720 individual vertical reflectivity profiles.

Each of the individual profiles in the cylinder was smoothed using a vertical reflectivity gradient check to reject single-point outliers caused by clutter residue or noise spikes in the data. Profile bins which remained empty after polar-to-cylindrical coordinate mapping were filled using a cubic interpolatory spline.

2.4. ASR-9 Fan-Beam Reflectivity Computation

For each of the reflectivity profiles in the cylinder, the equivalent ASR-9 fan-beam reflectivity Z_{asr} was computed at 4 nmi range intervals from 0 to 60 nmi and for both high and low receive beams using:

$$Z_{asr}(R) = \frac{\int_0^{\pi/2} Z(R,\phi)\, B_t(\phi)\, B_r(\phi)\, d\phi}{\int_0^{\pi/2} B_t(\phi)\, B_r(\phi)\, d\phi} \cdot \quad (1)$$

Here $Z(R,\phi)$ is the vertical reflectivity profile value found at range R and elevation angle ϕ (horizontal stratification of the reflectivity profile is assumed in converting from height to elevation angle), and $B_t(\phi)$ and $B_r(\phi)$ are respectively the transmit and receive antenna gain at elevation angle ϕ. Antenna gain measurements were previously obtained from a testbed ASR-9.

2.5. Calculation of VIL

The vertically integrated liquid water content (VIL) was computed for a given vertical reflectivity profile using the formulation proposed by Greene (1972):

$$VIL = 3.44 \times 10^{-6} \int_{h_{base}}^{h_{top}} Z^{4/7} dh \quad (2)$$

where h_{base} and h_{top} are the cloud base and cloud top in meters, and Z is the radar reflectivity factor in the standard units of mm^6/m^3. VIL has units of kg/m^2 and represents the in-cloud water content per unit area.

2.6. Calculation of ASR-9 Reflectivity Adjustments

The ASR-9's weather thresholds are stored as functions of range, receive beam, and weather level. The Z_{asr}(R,beam,weather level) curves and the Z_{max} values provide the information needed to derive threshold adjustments to bring the measured reflectivity in line with Z_{max}. The problem becomes one of computing the reflectivity scaling factor η which minimizes the mean square relative error ϵ between Z_{max} and Z_{asr} over the ensemble of profiles $\{p_1, p_2, ..., p_{N-1}, p_N\}$:

$$\epsilon^2(R,\text{beam,wx level}) = \sum_{p=1}^{N} \left[\frac{Z_{max} - \eta Z_{asr}(R,\text{beam})}{Z_{max}} \right]^2 . \quad (3)$$

The scaling factor which minimizes the error is given by:

$$\eta(R,\text{beam,wx level}) = \frac{\sum_{p=1}^{N} (Z_{asr} / Z_{max})}{\sum_{p=1}^{N} (Z_{asr}^2 / Z_{max}^2)} . \quad (4)$$

Equation (4) was used to calculate η (the reciprocal of the required threshold adjustment) as a function of range for both receive beams and for each of the six NWS weather levels. The weather level of a profile was defined to be the NWS level corresponding to Z_{max}.

3. VERTICAL REFLECTIVITY PROFILES

Vertical reflectivity profiles from each site were grouped into three intensity classifications, and the mean profile for each intensity category was computed. Profiles were assigned the greatest intensity category defined by peak reflectivity or altitude (18 dBZ top) criteria shown in Table 1. Mean profiles for the moderate and strong storm intensity categories for each of the five sites are shown in Figures 3 and 4 with solid curves. The number of profiles used to calculate each site-specific mean profile is given in parentheses. An overall mean profile was constructed by computing the unweighted mean of the five site-specific mean profiles for each intensity category and is depicted as a dashed curve in each of the graphs of Figures 3 and 4. Results from Konrad (1978) for observations taken at Wallops Island, Virginia are also shown for comparison. Konrad computed mean profiles from individual profiles grouped into 5 dBZ bins. For comparison with our results, we regrouped Konrad's mean profiles into our corresponding moderate or strong intensity categories, normalized each mean profile by it's peak reflectivity value, and computed mean relative reflectivity profiles.

Moderate profiles from Boston, Denver, Huntsville, and Kansas City tend to fall off significantly between 8 and

Table 1. Storm profile intensity classification criteria.

Category	Reflectivity (dBZ) [NWS Levels]	Altitude (ft)
Weak	< 41 [1 - 2]	< 25,000
Moderate	41 - 50 [3 - 4]	25,000 - 35,000
Strong	> 50 [5 - 6]	> 35,000

12 km. This is probably associated with the rapid decrease of moisture near the tops of the storms and the limiting effect of the tropopause. The Wallops Island profile is not inconsistent with this idea. The Huntsville, Kansas City, and Wallops Island profiles indicate a sharp reduction in drop sizes and/or number density above a surface-based high relative reflectivity layer. The surface-based constant reflectivity layer seen in the Denver profile exhibits lower relative reflectivity presumably due to the presence of a dry sub-cloud environment in some of the profiles. Profiles constructed from wintertime stratiform precipitation in Seattle are quite different from those from other sites. The mean profile exhibits a pronounced peak at 3 km, which is attributed to bright band effects.

Strong mean profiles extended 2-6 km higher than their moderate counterparts (Figure 4). This is especially true of the Kansas City profiles, probably because of the increased frequency of supercell storms in the Midwest. The Wallops Island profiles showed the least amount of change between the two intensity categories. There were almost no strong profiles from the Seattle data set, so no mean profile was constructed for this category.

In order to characterize the representativeness of the mean profiles, the standard deviation of relative reflectivity was computed as a function of altitude over the ensemble of profiles from each site (Figure 5). The standard deviation was computed based on normalized linear reflectivity units which range from 0 to 1. Hence, a standard deviation of 0.30 represents a variability of 30 percent. The standard deviations are between 0.35 and 0.40 at the surface, with a slight decrease in variability with height up to approximately 8 and 12 km for moderate and strong profiles, respectively. This region of relatively high variability implies the presence of small-scale reflectivity cores occurring over a range of altitudes. The large magnitude of this variability suggests that mean profiles should not be used in computations sensitive to small-scale features.
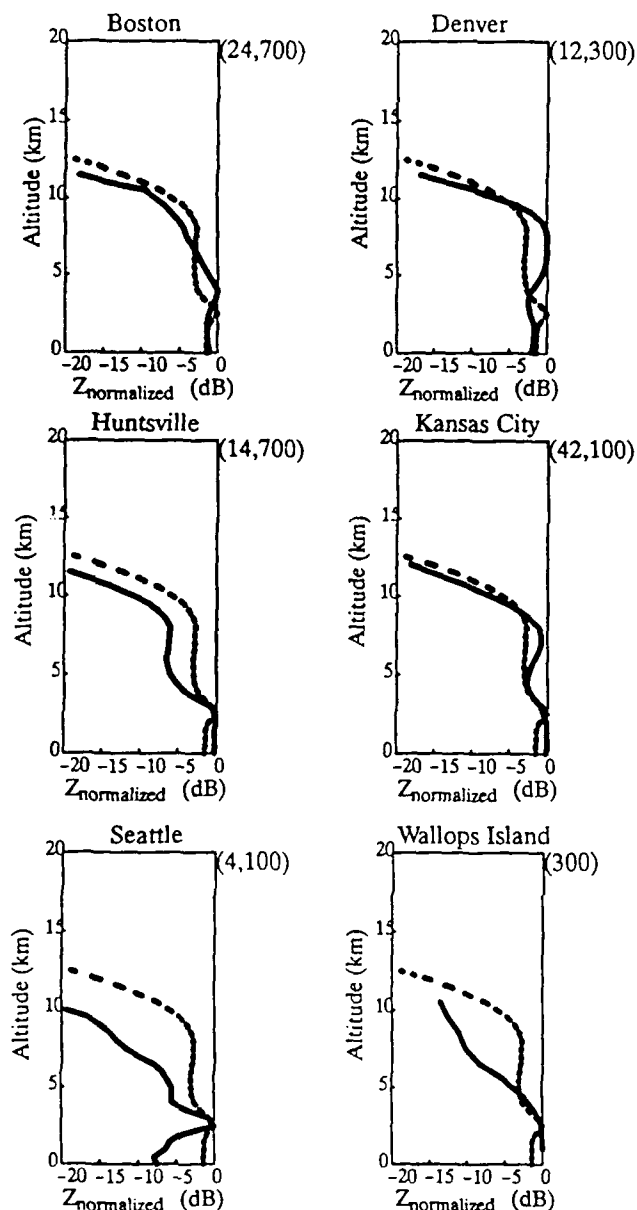
Figure 3. *Mean vertical relative reflectivity profiles (solid line) of moderate intensity for each of the five sites and for Wallops Island (from Konrad, 1978). Dashed line is 5-site mean profile. Numbers in parentheses indicate the number of profiles used to determine the mean.*

Figure 4. *As in Figure 3 but for strong profiles.*

4. COMPARISON OF CORRECTED ASR-9 REFLECTIVITY ESTIMATES AND VIL.

Mean vertical reflectivity profiles are useful for characterizing climatological similarities and differences between sites and different storm intensities. However, we found that the use of mean profiles for deriving threshold adjustments does not account for small-scale features often observed in the individual profiles. These features may be peaks associated with regions of hail growth or heavy precipitation aloft and may present significant hazards to aircraft.

Mean vertical reflectivity profiles are therefore inappropriate for determining fan-beam reflectivity adjustments.

An illustration of this can be seen in Figure 6a which shows a set of three synthetic reflectivity profiles normalized by their own maximum reflectivity and whose shapes are comparable to profiles commonly observed at different stages during the evolution of a storm cell. The corresponding mean profile is given in Figure 6b. The deep layer of near-maximum reflectivity apparent in the mean profile is an artifact resulting from the averaging of profiles with peaks at varying altitudes. Clearly, if a vertically averaged quantity such as Z_{asr} is computed for the mean profile and compared against the corresponding Z_{max}, the resulting dis-

36

Figure 5. *Standard deviations of moderate and strong mean profiles.*

Figure 7. *Differential reflectivity between the vertical profile maximum and uncorrected ASR-9 reflectivity for the three profiles and their mean shown in Figure 6. Curves are for the low receive beam.*

(a)   (b)

Figure 6. *Example of (a) three individual profiles (normalized by their maximum value) and (b) the corresponding mean profile (not normalized a second time).*

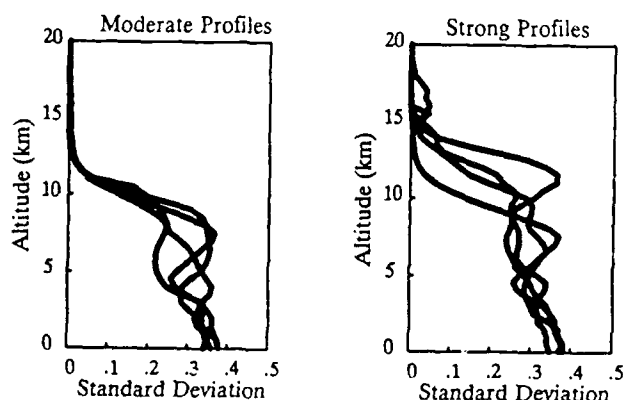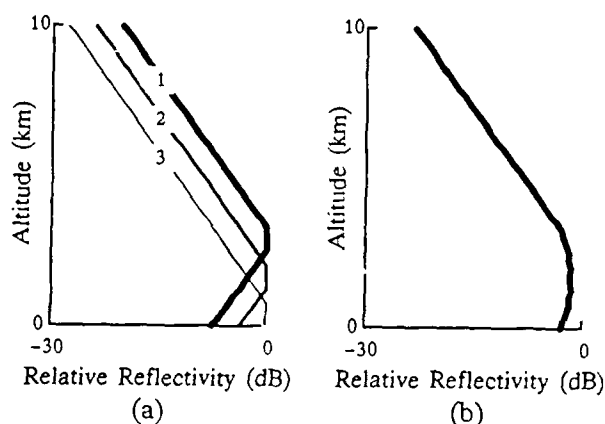agreement will be small, suggesting that very little adjustment of the Z_{asr} estimate is required. Figure 7 plots the differential reflectivity between Z_{asr} (uncorrected) and Z_{max} using individual and averaged profiles. Relative to the mean profile, a significantly greater differential reflectivity is seen between Z_{asr} and Z_{max} computed from the individual profiles in Figure 6a, especially at those ranges where the nose of the radar beam intercepts the storm profile above or below the profile peak.

The method adopted for computing a correction to the ASR reflectivity observations in order to more accurately report the storm intensity minimized the error between the reported reflectivity (Z_{asr}) and the desired reflectivity(Z_{max}). This computation was done for each of the five sites separately with one correction for each of the six NWS weather levels. These "site/level dependent" corrections were then combined and an exponential fit to the data was calculated to define the new correction. The metric used to evaluate the success of the correction was the percentage of profiles assigned to the correct weather level. The results of this

evaluation are shown in Figure 8 as a function of range. Shown are the results for the observed or uncorrected ASR reflectivities, the current operational correction, and the exponential fit or new correction. A significant improvement over the current correction is achieved by using the new corrections computed according to the method of minimizing the error.
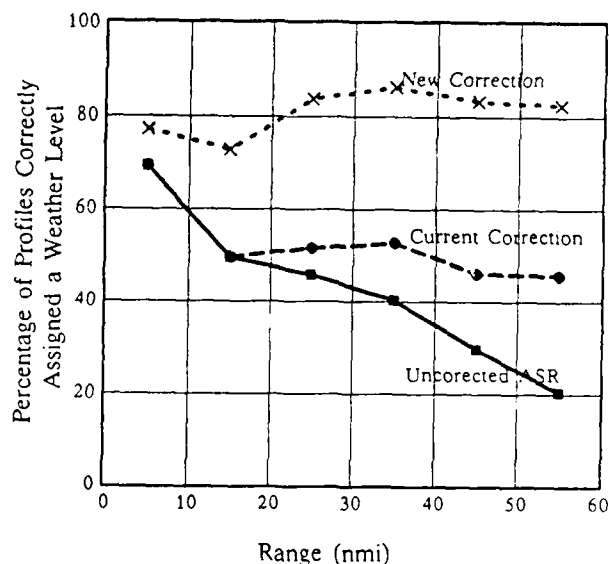
Figure 8. *Evaluation of the effectiveness of the new correction compared to the current correction and the uncorrected reports of precipitation intensity. See text for further explanation.*

Dobson (1978) found that fan-beam reflectivity was well correlated to VIL for a set of 37 profiles between the values of 30 and 70 dBZ. 115,000 profiles were available in the same reflectivity range from the data set used in this study and are also found to be well correlated to VIL. The correlation was computed for both uncorrected ASR reflectivity and ASR reflectivities adjusted with the new correction. This is shown in Figure 9 with boxes and triangles for

37

the uncorrected and corrected ASR reflectivities, respectively. A linear fit to the data in dB units was computed for each reflectivity product, and yield correlation coefficients of 0.85 and 0.88, respectively, for profiles with reflectivities greater than 30 dBZ. Inspection of the data suggests a linear relationship between VIL and fan-beam reflectivity for reflectivities above 20 dBZ, but that this relationship breaks down for reflectivities less than 20 dBZ. Note that for values less than the NWS level 1 threshold (18 dBZ), no correction is applied. The results shown here differ slightly from the results of Dobson (1978) (Figure 9 dashed line).

Figure 9. Comparison of VIL and ASR reflectivity for uncorrected ASR reflectivity (boxes) and corrected ASR reflectivity (triangles), where the correction is only applied to reflectivities greater than 18 dBZ. The dashed line indicates results of a similar comparison done by Dobson (1978).

were found to be inappropriate for use in calculation of the adjustments of the weather levels.

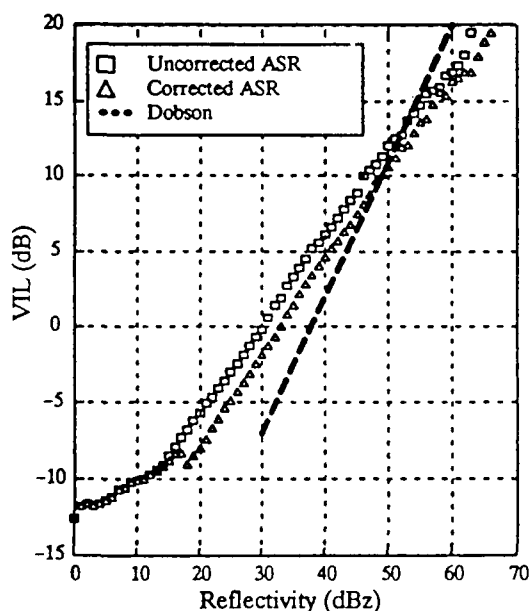Weather level adjustments were computed by minimizing the relative error between the fan-beam reflectivity Z_{asr} and the storm intensity represented by Z_{max}. A single correction was found to be suitable for all regions and weather levels. This correction yields substantial improvement over the initial adjustment based on a model reflectivity profile. Both adjusted and uncorrected fan-beam reflectivity estimates were found to be linearly correlated with VIL for reflectivities above 20 dBZ. This result may be useful in future interpretation of fan-beam reflectivity estimates.

6. REFERENCES

Alaka, M.A., R.C. Elvander, and R.E. Saffle, 1979: Nowcasts and Short-Range (0-2 Hour) Forecasts of Thunderstorms and Severe Convective Weather for Use in Air Traffic Control. Technical Report, U.S. Dept. of Commerce, NOAA, FAA-RD-79-98.

Dobson, E.B., A. Arnold, and F.L. Robison, 1978: Weather Detection Using Fan-Beam Radars. Preprints, 18th Conference on Radar Meteorology, 413-416.

Donaldson, R.J., 1961: Radar Reflectivity Profiles in Thunderstorms. J. Meteor., 18, 292-305.

Greene, D. R., 1972: A Comparison of Echo Predictability: Constant Elevation vs. VIL Radar Data Patterns. Preprints, 15th Radar Meteorology Conference, 111-116.

Joss, J. and A. Waldvogel, 1989: Precipitation Estimates and Vertical Reflectivity Profile Corrections. Preprints, 24th Conference on Radar Meteorology, 682-688.

Konrad, T.G., 1978: Statistical Models of Summer Rainshowers Derived from Fine-Scale Radar Observations. J. Appl. Meteor., 17, 171-188.

Weber, M.E., 1986: Assessment of ASR-9 Weather Channel Performance: Analysis and Simulation. Project Report ATC-138, Lincoln Laboratory, MIT, FAA-PM-86-16.

5. SUMMARY

The ASR-9 radar provides air traffic controllers with estimates of precipitation intensity quantized into the NWS six weather levels. The fan-beam reflectivity estimates may not be representative of the storm intensity in those instances where the vertical reflectivity profile is non-uniform. To counteract this effect, the weather reflectivity thresholds may be adjusted on a regional and range basis. Five regions across the continental United States were identified, and one site from each region studied. The analysis began with a characterization of the vertical reflectivities at each site through derivation of the mean profiles for moderate and strong storms. Examination of these profiles and their associated standard deviations lead to the conclusion that there is a large degree of variability in the shapes of these profiles and the altitude extent of the highest reflectivity features. Because of this variability, mean profiles

UNDERSTANDING AND PREDICTING MICROBURSTS *

Marilyn M. Wolfson

MIT Lincoln Laboratory

Lexington, Massachusetts 02173

1.   INTRODUCTION

Wind shear is a major cause of aircarrier accidents in the United States, and most of these accidents have been caused by one particular form of wind shear called a microburst (Zorpette, 1986). Microbursts have been defined as small scale, low-altitude, intense downdrafts which impact the surface and cause strong divergent outflows of wind. We know they are associated with thunderstorms and are usually but not always accompanied by heavy rainfall at the ground. However, a number of meteorologically distinct phenomena associated with thunderstorms can give rise to strong downdrafts and high surface winds. Most microburst research has focussed on the main precipitation driven downdraft of thunderstorms, both with and without significant surface rainfall. But other downdraft types such as the dynamically driven downdrafts at low altitude associated with "vortices" at the leading edge of expanding thunderstorm outflows and with "roll clouds" have also been associated with the microburst problem.

In this paper, I discuss these two primary forms of low altitude downdraft phenomena in thunderstorms. This differentiation is essential to discovering exactly what atmospheric conditions lead to the development of the most hazardous microbursts. A physically based predictive model for thunderstorm downdraft strength is presented which shows that the radar reflectivity of a storm alone cannot be used an a hazard index; information about the static stability of the atmosphere is also essential. I then show that the downdrafts associated with the gust front around a cold outflow from a small isolated thunderstorm, a microburst, are inherently stronger at low altitudes than those found in more straight-line gust fronts. Finally, I reexamine the most recent fatal U.S. microburst accident, the crash of Delta 191 at Dallas/Ft. Worth in 1985, and show that both types of low altitude downdrafts were encountered as part of the "microburst", although the downdrafts came from different storms.

2.   THE MICROBURST AIRCRAFT HAZARD

Three major aircraft accidents account for all of the aviation fatalities attributed specifically to microbursts in the United States (see Table 1). The first of these – the crash of Eastern 66 at Kennedy airport in New York on 24 June 1975 (112 fatalities, 12 injuries) – led to the introduction by Fujita and Byers (1977) of the new downburst/microburst terminology. The two other fatal microburst accidents were Pan Am 759 at New Orleans International airport on 9 July 1982 (152 fatalities, 9 injuries), and Delta 191 at Dallas/Ft. Worth International airport on 2 August 1985 (130 fatalities, 31 injuries). No one escaped injury in any of these

accidents. In all three of these cases, the thunderstorm downdraft implicated in the accident descended into a pre-existing outflow that was produced from a nearby thunderstorm. The presence of the turbulent gust front at the leading edge of the pre-existing outflow was not taken into consideration in assessments of the wind shear hazard in these cases.

In two of the four additional fatal accidents attributed to thunderstorm low altitude wind shear (Table 1), roll clouds were noted by eyewitnesses. These were the crash of a Braniff Airways plane at Falls City, NE on 6 August 1966 and the crash of an Ozark Air Lines plane St. Louis MO on 23 July 1973. No one escaped injury in these two accidents, either. In the Falls City crash, "ground witnesses observed the aircraft to fly into or over a roll cloud preceding a thunderstorm and shortly thereafter saw an explosion in the sky followed by a fireball falling out of the cloud. Two pieces, later identified as major portions of the right wing and empennage, were seen falling separately from the main part of the aircraft. Shortly thereafter the witnesses noted high gusty surface winds and light to moderate rain which accompanied the passage of a squall line through the area. The cause of the accident was determined to be inflight structural failure caused by extreme turbulence" (Rudich 1986). Roll clouds mark the ascending branch of a horizontal vortex, usually either the gust front itself, a solitary wave, or part of an undular bore (Smith 1988). Before microbursts, gust fronts were considered the primary form of aviation hazardous low altitude wind shear. The information in Table 1 indicates that they are indeed extremely hazardous.

What role did the low altitude downdrafts and turbulence associated with the gust front at the leading edge of a pre-existing outflow play in the three microburst related fatal aircraft accidents? Certainly the divergent headwind-tailwind shear of the thunderstorm outflow itself can easily become strong enough to cause an unmanageable loss of lift to an aircraft penetrating it (Figure 1). Figure 2 shows that the magnitude of the downdraft velocity has as much effect as the horizontal wind shear on the ability of a plane to maintain its speed and glide slope profile. But Figure 2 also shows that even performance increasing wind shear (increasing headwind) and updrafts, typically associated with gust fronts, can be unsafe when their magnitudes are large. The effect of *turbulence* on aircraft control is not captured by the F-factor index, but the hazard can be extreme, especially at low altitudes.

I suggest that the pre-existing gust front in each of the fatal microburst accident cases may have added a crucial ingredient to the overall hazard encountered. When a thunderstorm outflow forms on top of an existing gust front, two hazardous regions become juxtaposed that would otherwise be physically separate. This *combination* may be what was first called a downburst, and later a microburst, by Fujita and Byers (1977).

Table 1. Aircraft accidents in the United States attributable to microbursts or low altitude wind shear associated with thunderstorms. Wind speed is given in meters per second, and cell diameters are given in kilometers. F/I/U indicates number of fatalities, injured, and uninjured. Information adapted from Viemeister (1961), Fujita (1985), Rudich (1986), and Laynor (1986). MB indicates microburst.

Location	Date	Winds	Diameter	Rain	Weather	F / I / U
Bowling Green	28 Jul 43	strong	10–15	yes	strong squall wind from violent downdraft fanning out at surface. unusually severe turbulence	? ? 2
Mason City, IA	22 Aug 54	35–40	5	heavy	plane entered thunderstorm at 400–500 ft; sank in downdraft	12 ? ?
Rochester NY	2 Jul 63	shift-ing	?	heavy	thunderstorm approaching runway from west. plane took off into heavy rain and shifting winds	? ? ?
Falls City, NE	6 Aug 66	gusty	n/a	light	roll cloud preceding thunderstorm; severe turbulence	42 0 ?
St. Louis	23 Jul 73	strong	?	heavy	severe thunderstorm with roll clouds, heavy rain, strong winds	38 6 0
Chatta-nooga	27 Nov 73	?	?	heavy	low altitude wind shear existed in heavy rain on approach	0/42/37
New York	24 Jun 75	10–17	5–10	heavy	hot smoggy day, seabreeze; light, moderate, & heavy rain; numerous small cells, spearhead echo 8 x 32 km; MB	112 12 6
Denver	7 Aug 75	>12	2	light	numerous scattered showers–small and weak; cell broke into two, thunder heard, spearhead echo 8 x 16 km; MB	0/15/119
Raleigh-Durham	12 Nov 75	?	?	heavy	unexpected heavy rain, windshear and downdraft at 100 ft agl	0 ? 135
Phila-delphia	23 Jun 76	20	4	yes	headwind increase in front of shower; scattered showers and thunderstorms near warm front, growing spearhead echo 13 x 27 km; MB	0/86/23
Tucson	3 Jun 77	14	2	none	numerous CB around airport; gust front passed with 25 m/s surface winds; MB	0 0 ALL
New Orleans	9 Jul 82	>15	2	heavy	scattered showers, 7 gust fronts nearby, recent growth of convective cloud tops; MB	152/9/0
Detroit	13 Jun 84	10–16	?	heavy + hail	thunderstorm with heavy rain; 3/4 inch hail at 100–200 ft agl; turbulence, severe wind shear	0 0 ALL
Dallas	2 Aug 85	22–35	4	very heavy	scattered small cells initiated on gust front out of large cell to NW, very hot day, cloud top of MB cell 23 Kft (questionable – NTSB reported 40–50 Kft); MB	130/31/0

Figure 1. Schematic drawing of an aircraft encounter with a microburst. Notice that the increased headwind lifts the plane above its intended glideslope while the increased tailwind causes the plane to fall below its intended glideslope. This simplified view of a microburst is inaccurate because it does not depict the extremely turbulent vortex at the leading edge of the outflow.
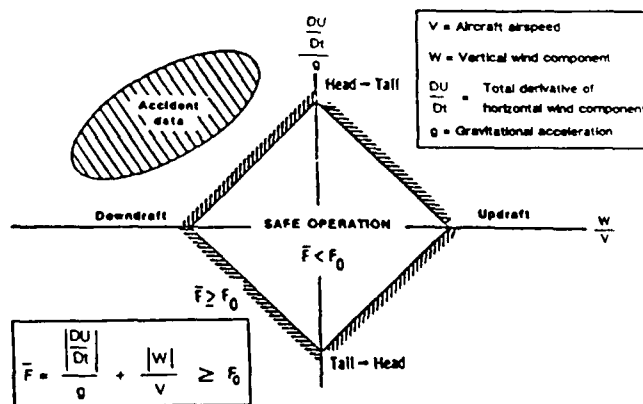
Figure 2. Definition of F-factor wind shear hazard index. Typical threshold values (F₀) for jet transport range from 0.10 - 0.15. Notice that all of the aircraft accidents are thought to have taken place in the quadrant associated with divergent horizontal winds and downward vertical velocities along the flight path. Adapted from Targ and Bowles (1988).

40

3. PREDICTING THUNDERSTORM DOWNDRAFT AND OUTFLOW STRENGTH

Certainly a newly formed thunderstorm downdraft and surface outflow were key factors in all the microburst aircraft accidents. In this section, I focus on the identification of observable parameters that will allow quantitative prediction of the eventual maximum downdraft and outflow strengths.

A great deal of research over the last few years has attempted to quantify the factors influencing the development of the strongest thunderstorm downdrafts and outflows. One of the apparent mysteries is that thunderstorms with quite different downdraft and outflow strengths can occur simultaneously, in the same environment. Even when the reflectivity or water content of these cells is taken into account, differences remain that are related to cell forcing, geometry, or the proximity and strength of neighboring convection. Another apparent mystery is that storms with similar reflectivity levels on different days produce very different strength outflows. Because of the proportionality between reflectivity and the downward acceleration due to water loading, some argue there should be a monotonic relationship between downdraft/outflow strength and reflectivity. Yet evidence is to the contrary (e.g., Wilson et al. 1984; Biron and Isaminger 1989). This is, in part, because environmental factors that promote the thermodynamic generation of negative buoyancy are of crucial importance in determining the ultimate downward acceleration and observed downdraft strength. Subtle differences in the vertical temperature structure of the environment, such as the existence and height of any elevated stable layers or inversions, also play an important role in determining the ultimate downdraft strength (Knupp 1987).

3.1. Model Derivation

Although a number of observational studies on determining reliable precursors for microbursts have been performed (e.g., Campbell and Isaminger 1989; Potts 1989), none have gone beyond basic statistical correlation of these precursors with resultant outflow strength. The approach used here is to quantitatively predict thunderstorm downdraft and outflow strength with a simple model based on the vertical momentum and continuity equations. The published axisymmetric numerical thunderstorm model output of Proctor (1989; referred to as P89), Krueger and Wakimoto (1985; KW) and Droegemeier and Babcock (1989; DB) is used as "data" to derive the model. Details of the derivation not presented here can be found in Wolfson (1990).

The vertical momentum equation is used to indicate the expected dependence of the vertical velocity on the various forcing mechanisms at work in the thunderstorm downdraft. Neglecting entrainment, the Boussinesq form of the vertical momentum equation can be written as:

$$\frac{dw}{dt} = g\frac{\theta'}{\theta_0} - g(l+i) - \frac{P_z'}{\rho_0} \qquad (3.1)$$

where w is the vertical velocity, t is time, g is the gravitational acceleration, θ_0 is the potential temperature of the environment which varies only in height and θ' is the difference in potential temperature between a parcel and the environment, $(l+i)$ is the mass mixing ratio of liquid water plus ice, P' is the perturbation pressure, ρ_0 is the density

which varies only in height, and the subscript z denotes partial differentiation in height. Perturbation pressure buoyancy itself (as opposed to its vertical gradient) and frictional effects are ignored. Buoyancy effects of humidity in the environment have not been included but they can be easily by substituting virtual potential temperature for θ in Eq. (3.1).

The rationale behind the model development is to relate each term in the vertical momentum equation to the observable environmental or storm characteristics that are physically responsible for its ultimate magnitude. A number of simplifying assumptions have to be made. The total vertical acceleration is approximated as:

$$\frac{dw}{dt} \sim (\frac{w^2}{2})_z \qquad (3.2)$$

This represents the left hand side of Eq. (3.1). Making this substitution, and integrating Eq. (3.1) in height, the following dependence of the vertical velocity on the depth of the downdraft column results:

$$w^2 \sim forcing \cdot \Delta z$$

Knupp (1987) showed that this downdraft depth can be related to the "transition level" in the sounding. The downdraft velocity data from the cases he investigated do show this square root dependence on the height of the transition level. Addis (1984) showed a similar dependence of the vertical velocity on the height of the downdraft column in his convective storm outflow modelling work.

The first term on the right hand side of Eq. (3.1) is the temperature buoyancy. For a given condensate mixing ratio, the downdraft velocity will increase as the lapse rate in the subcloud environment increases from stable toward neutral values, largely because of the resultant temperature buoyancy contribution to the vertical acceleration. Studies have shown that for strong downdrafts and outflows to occur at lapse rates below about 7 K/km, high reflectivity must be present. However, when the lapse rate approaches the dry adiabatic value, almost any concentration of precipitation can produce strong downdrafts, especially if the subcloud layer is deep. Srivastava (1985) calculated the temperature excess of descending air parcels over their ambient environment for various subcloud lapse rates and liquid water mixing ratios, using a model based on evolution equations for raindrop mass and size distribution, thermodynamic energy, water substance, and vertical velocity. His tabulated data show a quadratic dependence of this temperature difference on lapse rate for a given liquid water mixing ratio:

$$\theta' \sim \Gamma^2 \quad or \quad w^2 \sim \Gamma^2 \Delta z \qquad (3.3)$$

where Γ is the temperature lapse rate. By comparison with the axisymmetric numerical model data of KW(Figure 3), it was discovered that this relationship does indeed hold true for a given precipitation mixing ratio. As the mixing ratio increases, greater downdraft velocities are achieved, but the linear dependence of vertical velocity on lapse rate does not vary much. The mixing ratio dependence of the temperature buoyancy represents one part of the vertical acceleration due
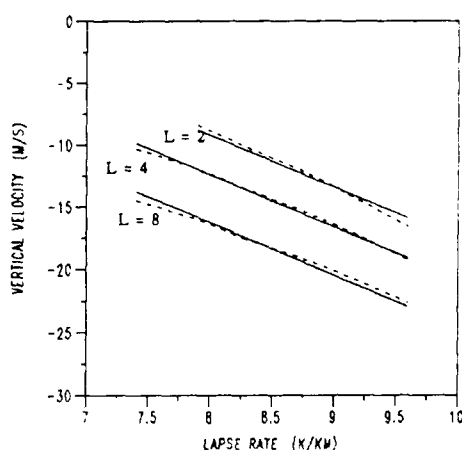
Figure 3 . Plot of the vertical velocity (w) vs the environmental lapse rate (Γ) from the numerical simulations by Krueger and Wakimoto (1985), for liquid water mixing ratios (L) of 2, 4, and 8 g/Kg (dashed lines). The solid lines represent the best fit for each mixing ratio using the mean of the slopes derived from the least squares linear fit for each mixing ratio curve individually: $w_2 = -4.175 \ \Gamma + 24.19$; $w_4 = -4.175 \ \Gamma + 20.99$; $w_8 = -4.175 \ \Gamma + 17.14$.

to total water concentration, and can be represented by an undetermined function of the mixing ratio:

$$w^2 \sim [\ \Gamma^2 + f (L) \ ] \ \Delta z \ .$$

Note that L is used to represent the total mixing ratio instead of ($l + i$) as in Eq. (3.1) because no account is taken of the phase of the water mass present. The temperature buoyancy effects from the total water content can be quantitatively incorporated in the precipitation loading term.

The second term on the right hand side of Eq. (3.1) is the contribution of precipitation loading to the vertical acceleration. The form of that term, combined with the simplifying approximation of Eq. (3.2), gives the following dependence of the vertical velocity on the precipitation content:

$$w^2 \sim L \ \Delta z \ .$$

Comparison with numerical model results of KW and DB showed that if L was interpreted as the peak value of a Gaussian distributed precipitation region, then the vertical velocity also depended equally strongly on the vertical depth (Gaussian half amplitude width in the vertical) of that precipitation region. Representing this depth as D, the velocity dependence can be expressed as:

$$w^2 \sim L \ D \ \Delta z \ .$$

The parameters L and D will ultimately be estimated from radar reflectivity which depends strongly on the precipitation drop size distribution present in the storm. Many equations relating reflectivity to water content that account for these different distributions have been derived. The choice of equation will depend on the type of convection present (perhaps the peak reflectivity observed), the climatic region, the season of the year, etc. All of the known depen-

dence of the vertical velocity on precipitation size distribution and phase will be contained in this choice.

The third and final term on the right hand side of Eq. (3.1) is proportional to the vertical gradient of the perturbation pressure. For this thunderstorm downdraft application, the pressure perturbation of interest is created largely by the descending downdraft itself, and it generally opposes the downward motion. If all other forcing remains equal, the downdraft velocity will vary inversely with the downdraft radius at large radii, because of the induced pressure perturbation (P89, KW). But the same induced pressure perturbation sets up the horizontal pressure gradient that ultimately drives the divergent surface outflow as the downdraft reaches the ground; the pressure is thus the connection between the downdraft and outflow. Based on the continuity of mass and on dimensional grounds, it can be seen that:

$$\frac{u}{w} \ \sim \ \frac{width}{height} \ \sim \ \frac{1}{A}$$

where u is the outflow velocity from a cylindrical downdraft reaching the ground, and A is the aspect ratio of the downdraft defined as the ratio of its height to width. The third term on the right hand side of Eq. (3.1) will be neglected, and the pressure effects will be incorporated in a prediction equation for the ratio u/w.

The predicted outflow speed will depend not only on the vertical velocity and the aspect ratio of the downdraft, but on the temperature of the downdraft (outflow) air as well. Fawbush and Miller (1954) modelled this dependence of horizontal wind speed with a cubic equation in temperature based on observations, but P89 recently found that a linear relationship was roughly as accurate. However, there are no theoretically obvious reasons for either the cubic or linear relationships. One theoretical guideline that could be used is the well known equation for the speed of the leading edge of a density current that is thin relative to the depth of the fluid in which it is propagating (e.g., Simpson 1987):

$$V \ = \ \sqrt{ \ 2 \ g \ h \ \frac{\Delta \rho}{\rho} }$$

where V is the gravity current speed, $\Delta \rho$ is the density difference across the front, ρ is the density of the less dense fluid, and h is the depth of the density current. The horizontal flow behind the leading edge is often faster than, but directly proportional to the speed of the front, so the dependence on density difference should be the same. Since the magnitude of the fractional potential temperature difference across the front is proportional to that of the fractional density difference, Eq. (3.3) would imply the outflow speed was related linearly to the lapse rate:

$$\frac{u}{w} \ \sim \ \Gamma \ .$$

Comparison with numerical modelling results showed there was indeed a dependence of the outflow speed on the lapse rate that could be modelled as linear, but not enough data were available to determine if the dependence was of higher order or not. Thus a linear dependence between the outflow speed and the lapse rate was assumed, and the best fit coefficients were derived.

42

3.2. Prediction Equations

In the preceding section, the dependence of vertical velocity on the radius and depth of the precipitation core, the precipitation mixing ratio, the environmental temperature lapse rate, and the height of the transition level was inferred by simple physical arguments. These results were confirmed through comparison with results from the published axisymmetric numerical modelling studies of P89, KW, and DB. These quantitative results were combined to yield:

$$W^2 = [\, 7.3\, \Gamma^2 + 9.75\, L\, D - 480\,]\, \frac{T_r}{3.3} \qquad (3.4)$$

where W is the maximum downdraft velocity in m/s, Γ is the mean temperature lapse rate from the surface to the freezing level in K/km, L is the precipitation mixing ratio in g/Kg, D is the depth of the precipitation core in km, and T_r is the transition level of the sounding in km. If evaluating the terms on the right hand side of Eq. (3.4) produces a negative number, W should be interpreted as negligibly small.

The dependence of the ratio of the maximum outflow speeds (U) to the maximum downdraft speeds (W) was found to depend strongly only on the aspect ratio (A) of the precipitation core (i.e. ratio of vertical to horizontal extent), with a weak dependence on the environmental lapse rate. These results were combined into a predictive equation for the ratio U/W which, when combined with Eq. (3.4), provides a predictive equation for U alone:

$$\frac{U}{W} = (\, \frac{.75}{A} + .65\,)\, \frac{\Gamma}{9} \qquad (3.5)$$

where all of the variables have been defined above. If the predicted value of U/W is less than 1.0, the value should be set equal to 1.0. For example, when the lapse rate is dry adiabatic, $U/W = 1$ for aspect ratios ≥ 2.75.

In applying Eqs. (3.4) and (3.5), a three dimensional radar reflectivity field would be searched for storm "cells", significant maxima in the field, to locate the sites of potential strong downdrafts. A bi-Gaussian distribution would then be fit to these regions, after they had been converted from reflectivity to water mixing ratio. The peak value of the Gaussian mixing ratio distribution would be used for L, the depth at half maximum for D, and the ratio of D to the width at half maximum would be used for A. Because information on the downdraft width is available through application of this model, the surface divergence as well as the downdraft and outflow speeds can be predicted. Indicators of aircraft performance loss that depend not only on the differential velocity, but on the horizontal divergence and the vertical velocity as well, can readily be calculated (e.g., F-factor index, Frost and Bowles 1984; see Figure 2).

3.3. Application of Model

Recent papers by Wakimoto and Bringi (1988) and Kingsmill et al. (1989) gave enough data on a "strong" airmass thunderstorm that occurred near Huntsville, AL on July 20, 1986 to estimate the parameters needed for predicting the downdraft and outflow velocities via Eqs. (3.4) and (3.5), and to compare the predictions with what was actually

observed. Enough data were also presented for predictions on two other storms, July 13 and July 16, 1986. Wakimoto and Bringi (1988) noted that the soundings on these two days were similar to the July 20 sounding, but that these storms resulted in only "weak" and "moderate" outflows, respectively.

To estimate the parameters needed for the prediction equations, the reflectivity values were first converted to liquid water content using an equation derived by Burrows and Osborne (1986) for the volume concentration of water, and normalized by the ambient density. A Gaussian shape was subjectively fitted to the resulting distribution to give the liquid water content at the peak (L), the core depth (D; the Gaussian width at half amplitude), and the core aspect ratio (A). By fitting a bi-Gaussian distribution to the liquid water content field, the data characteristics match as closely as possible the water content fields used to initiate the numerical models from which the equations were derived. The other required parameters were derived from the published soundings.

The model estimates for these three high reflectivity cases are compared with the actual data in Table 2 . The simple model given by Eqs. (3.4) and (3.5) has correctly ranked these quite different storms occurring in similar environments, according to their outflow strength. This suggests that thunderstorm downdraft and outflow strength might be predicted quite adequately with standard radar reflectivity data and a proximity sounding. Because radar reflectivity increases when frozen condensate melts, part of the increased acceleration from the thermodynamic effects of ice is incorporated even in this simple model.

Wakimoto et al. (1989) studied a low reflectivity storm that occurred in the Denver area on July 9, 1987 with multiple Doppler radars and photogrammetric analyses. The model estimates for this case are also given in Table 2 . In

Table 2 . *Application of predictive model to 4 storm cases. The variables given are identified in Eqs. (3.4) and (3.5). The asterisks indicate outflow values estimated from single Doppler radar data; the vertical velocities for those cases were not estimated. The other data were derived from multiple Doppler analyses.*

Jul 20 '86	A	D	dBZ	L	Tr	Γ	W	U
(Strong)	1.8	2	63	27	2.2	7.2	16.8	16.5
						actual:	13	17
Jul 13 '86	A	D	dBZ	L	Tr	Γ	W	U
(Weak)	1.25	1.5	57	10	2	7.0	4	4
						actual:	?	7 *
Jul 16 '86	A	D	dBZ	L	Tr	Γ	W	U
(Moderate)	1.0	2	60	34	1.2	7.0	14	14
						actual:	?	9 *
Jul 9 '87	A	D	dBZ	L	Tr	Γ	W	U
(Low dBZ)	1.0	2	25	0.2	4	9.4	14.3	21.5
						actual:	13.4	> 15

contrast to the previous high reflectivity cases, this case had only 25 dBZ or 0.2 g/Kg peak water content in the core. Thus the second term on the right hand side of Eq. (3.4) is essentially negligible in this case. Again in contrast to the first three cases, the first term on the right hand side of Eq. (3.4) is very large in this case because of the nearly dry adiabatic lapse rate between the surface and the freezing level. The result is a downdraft and outflow strength comparable to the "strong" high reflectivity storm of July 20, 1986.

3.4. Summary

The ability of the model given by Eqs. (3.4) and (3.5) to correctly rank, and fairly closely estimate, the eventual downdraft and outflow velocities in these four quite different cases adds confidence to the assertion that it approximately captures the essential physics of accelerating downdrafts and outflows. By developing a physically based predictive system, there is hope that the system can remain reliable as the storms it has to detect change from the very dry virga shafts typical of the Denver area to the very wet thunderstorms in the humid southeastern part of the country. This model shows that the radar reflectivity of a storm alone cannot be used as a hazard index; information about the static stability of the lower atmosphere is also essential.

4.   LEADING VORTEX RING IN AXISYMMETRIC OUTFLOWS

The most important low altitude downdrafts in thunderstorm outflows, apart from the central precipitation driven downdraft, are those associated with the "vortex" that develops at the leading edge of the dense outflow, the gust front. As mentioned previously, in all three of the fatal microburst aircraft accidents, a gust front from an older thunderstorm outflow was present when the thunderstorm outflow implicated in the accident occurred.

While every gust front has a horizontal vortex circulation associated with the "head" (Figure 4), the circulation
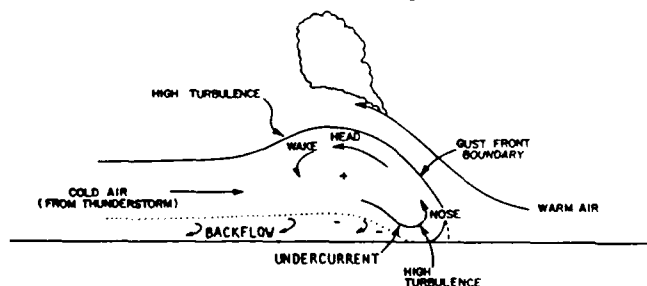
Figure 4 . Schematic representation of an atmospheric density current. Taken from Goff (1976).

is much more pronounced relative to the depth of the outflow in an axisymmetric outflow than in a unidirectional flow. Strong surface winds and strong downdrafts *at low altitudes* will be associated with this leading vortex region, as will extreme turbulence. It is thus a very important part of the microburst problem, and needs to be understood. In this section, I focus on explaining the leading vortex ring structure of gust fronts from axisymmetric outflows.

4.1.   Observations

Figure 5 shows the surface reflectivity of a strong, isolated microburst observed with the FAA–Lincoln Laboratory Terminal Doppler Weather Radar (TDWR) testbed (Evans and Turnbull 1989) near the Memphis International

airport on 26 June 1985. Observers noted extremely heavy precipitation during this storm. Taking as time T the time shown in Figure 5 (a), the evolution of the outflow at five times from T+1.5 min to T+5.6 min is shown in Figure 5 (b). The high reflectivity (45–55 dBZ) main storm
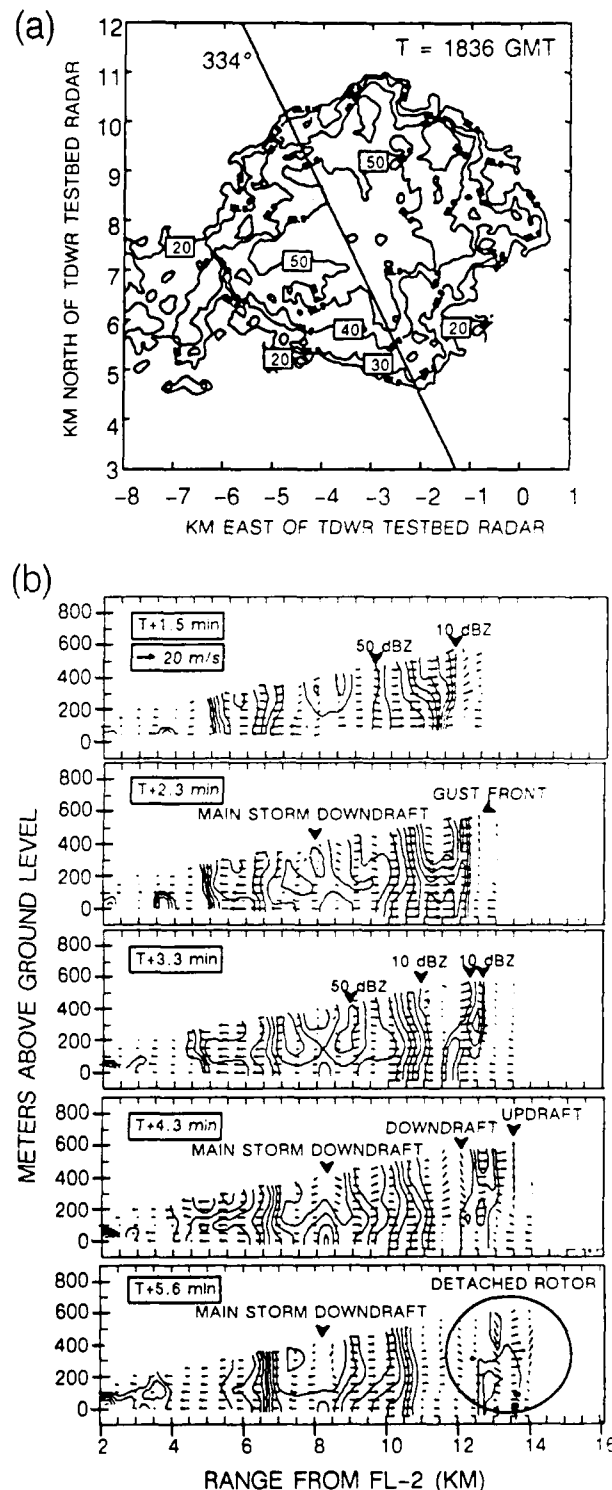
Figure 5 .   (a) TDWR testbed radar 0.5° elevation scan at time T, 1836:29 GMT, on 26 June 1985. Data were collected near Memphis, TN. Reflectivity is contoured at 20, 30, 40, and 50 dBZ (selected contours are labelled with boxed numerals). (b) Vertical cross-sections along azimuth 334° [shown in (a)], at five sequential times. Reflectivity is contoured every 5 dBZ from 10 dBZ.

downdraft is located at a range of approximately 8 km from the TDWR testbed radar in these cross-sections. The strongest outflow winds are located approximately 100 m agl. The cross-sections clearly show the development of a horizontal vortex or "rotor" associated with the leading gust front as the outflow spreads away from the storm center. This vortex eventually detaches and moves away from the main outflow.

4.2. Physical Explanation of Leading Ring Formation

This process of formation of an intense leading "vortex ring" in an axisymmetric gravitational flow has been qualitatively explained as a result of radial expansion of the circumference, and thus the head wave vortex axis, of the dense outflow (Fujita 1984; see Figure 6). The argument
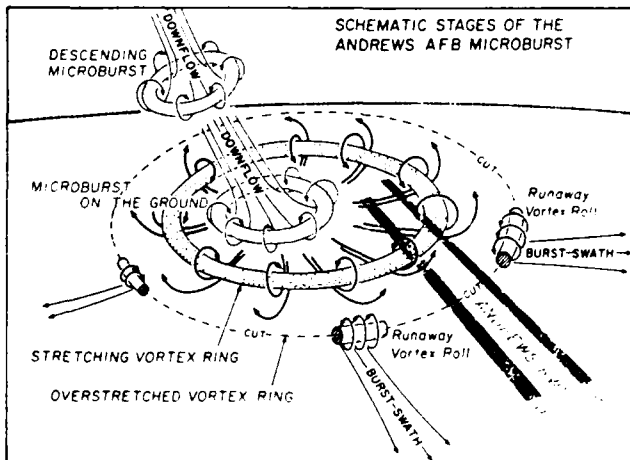
Figure 6 . Depiction of the four stages in the Andrews Air Force Base microburst by Fujita (1984).

offered is that, "because the fluid volume in a vortex is (approximately) conserved, its cross-sectional area must decrease. Conservation of angular momentum about the center line of the vortex then implies that the vorticity increases." (Linden and Simpson 1985). This qualitative model for the leading vortex in dense axisymmetric outflows has been inconsistently formulated without the benefit of complete observations. It is essentially incorrect; the volume of the leading vortex is not conserved but steadily increases with time.

The correct model for understanding the formation of a leading vortex ring in dense, axisymmetric outflows has been described by Garvine (1984). Garvine modelled the case of a radially spreading surface buoyant flow with a continuous source to help explain the observed characteristics of river plumes, created where fresh water empties into coastal seawater. A thin layer of buoyant water spreads radially under the force of gravity, with a sharp frontal boundary at the leading edge.

The main body of the plume is modelled using the inviscid nonlinear shallow water equations, and the frontal boundary is represented by a jump condition. The Boussinesq approximation is made, and wind stress, mixing, and the Coriolis acceleration are all neglected. The difference in density between the buoyant fluid and the surrounding fluid is constant, so the radial pressure gradient and the fluid velocity are vertically uniform. With these approximations, the governing equations of mass continuity and radial momentum for the main plume body are:

$$(c^2)_t + \frac{(rc^2 u)_r}{r} = 0$$

$$u_t + (\frac{u^2}{2} + c^2)_r = 0$$

where $c \equiv \sqrt{(g'd)}$ is the long internal wave speed (g' is the reduced gravity, and d is the depth of the gravity current), t is the time from initial fluid release, r is the radial distance from the source center, u is the radial velocity, and the subscripts denote partial differentiation with respect to that variable. These two equations together form a hyperbolic system with a pair of characteristic lines given locally by:

$$\frac{dr}{dt} = u \pm c \qquad (4.1)$$

along which the corresponding characteristic equations are:

$$du \pm 2 dc = \mp \frac{cu}{r} dt \qquad (4.2)$$

The "+" (upper) and "−" (lower) families of characteristics represent the nonlinear, internal gravity waves that propagate upstream and downstream, respectively, at phase speed c relative to the outflow, and at absolute wave speed $u \pm c$ relative to fixed coordinates. The equations corresponding to Eqs. (4.1) and (4.2) for parallel flow are identical except for the term on the right hand side of (4.2), which represents the effects of radial expansion on the flow.

The results of a sample calculation with no entrainment are shown in Figure 7 . The scaled interface depth of
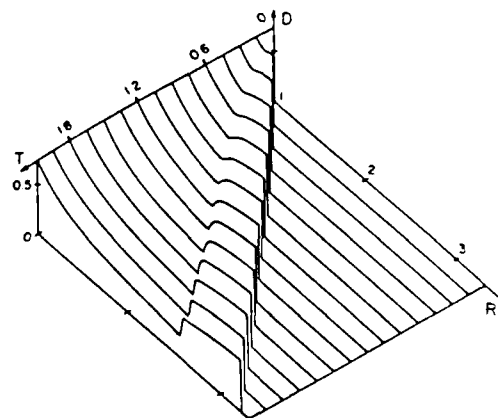
Figure 7 . Isometric projection of scaled interface depth (D) as a function of scaled range (R) and time (T). Taken from Garvine (1984).

the modelled river plume is shown, but this can also be interpreted as the interface height of a cold thunderstorm outflow. The most prominent feature of the flow is the clear emergence of a ridge, at first indistinct, but later quite distinct with a sharp dip (dubbed the "trailing front", in contrast to the "leading front"). This trailing front became so steep that Garvine treated it numerically as a second front with its own jump conditions. The width of the ridge or ring feature increases with time, and the interface height within the ring is about 20% greater at the leading front than at the trailing front.

45

As the fluid expands radially, the fluid at the leading edge of the current begins to accelerate outward. However, the acceleration of the fluid just behind the front is limited by the front itself, and these disturbances will propagate back away from the front. The first waves to be reflected off the leading front (minus family) have low initial wave speed $(u - c)$, since c is relatively high in the deeper flow near the front. They are later overtaken by reflected waves from further upstream in the ring, nearer the steady spreading regime. This overtaking is in the form of wave coalescence, a necessary condition for the formation of an interior front. The reflected waves continue to accumulate within the ring at the trailing front, causing the trailing edge of the ring to deepen.

The volume of the ring feature, proportional to the product of the mean radius and the ring width and depth, continually increases with time as a result of inflow into the ring through the trailing front. In the case of no entrainment, it had increased by a factor of 6 by the time the leading front had reached a distance of about 10 times the source radius. With entrainment, the results are qualitatively the same, but the increase in volume is not as marked because fluid in lost at both fronts. This basically refutes the argument that the frontal ring in axisymmetric outflows is a vortex tube that undergoes stretching as the flow expands.

In a parallel, two dimensional flow released from a line source, both plus and minus families of characteristics would be straight lines, corresponding to internal waves of *zero* amplitude. All properties of the flow except for the position of the front would be uniform in time and space. No changes in the flow state would occur, and to an observer moving with the flow at the frontal speed, the flow would appear steady. Neither the trailing front nor the radial ring would form.

4.3. Summary

The gust front at the leading edge of the cold outflow from a small, axisymmetric thunderstorm (e.g., Figure 5) is fundamentally different from its more straight line counterpart, either from a very large circular storm or a line storm (e.g., Figure 4). The rapid build up of fluid at the gust front edge only occurs in small, axisymmetric outflows where the radial expansion of the flow is large. This fluid in the leading "vortex" ring is extremely turbulent, and contains violent updrafts and downdrafts; it represents a very significant part of the microburst hazard. Moreover, the fluid ring is quite stable and can persist long after the primary divergent outflow has dissipated. The idealized outflow from a small isolated cell with no leading vortex front (Figure 1) essentially never occurs.

5. FATAL MICROBURST AIRCRAFT ACCIDENTS

In the preceding two sections, I have discussed the important hazardous low altitude downdrafts in thunderstorm outflows: 1) the precipitation driven downdraft, coincident with the reflectivity core, and 2) the downdrafts associated with the gust front at the leading edge of the outflow. I suggest that both of these types of downdrafts were involved in each of the fatal U.S. microburst aircraft accidents: JFK 1975, New Orleans 1982, and DFW 1985.

The most recent of these accidents was the crash of Delta Flight 191 at Dallas/Ft. Worth airport on August 2, 1985. There was a digital flight data recorder on board the aircraft, so it was possible to recover unambiguously the three dimensional wind field through which the aircraft flew (Wingrove and Bach 1987). I will focus attention on the DFW accident since the data are far less ambiguous than those available from the other two accidents.

5.1. Hypothesized Scenarios for DFW Accident

Several conceptual models and hypotheses have been offered to explain the meteorological events giving rise to the measured winds, especially the short wavelength "vortices" or rapid oscillations in wind components and temperature encountered during the last 20 s of the flight. These conceptual models all include a recently developed thunderstorm outflow with a radius of 2 km, at the following locations relative to the north end of runway 17L:

0.15 km west	3.5 km north	Fujita (1986)
0.5 km west	3.6 km north	Caracena et al. (198?)
0.6 km east	3.5 km north	Proctor (1988)

Hypotheses for the vortices include:

Fujita (1986): Three concentric downdraft outflows. Caracena (1987): Old vortices formed around downdraft and injected into outflow; Linden and Simpson (1986) and Droegemeier and Babcock (1989): Finite amplitude Kelvin-Helmholtz billows; Wolfson (1990): Cylindrical solitary waves.

These hypotheses are all quite plausible mechanisms for creating vortices under some circumstances. The question is, can they really account for the observed wind shear pattern encountered by Delta 191 at DFW? One way to test these hypotheses is to try to simulate the suggested scenarios with numerical models.

With the help of Drs. John Anderson and Jerry Straka at the University of Wisconsin, an axisymmetric numerical experiment was performed with Anderson's (1990) model to test Fujita's "three concentric downdrafts" hypothesis for the DFW vortices. We modelled this as a single pulsating cylindrical downdraft. The horizontal and vertical grid resolution was 75 m, the time step 0.5 s, the domain 300 grid points wide by 100 high, and the eddy diffusion coefficient 40 m^2/s. The environmental lapse rate was dry adiabatic (300 K) up to 5 km agl, and stable above (4 K/km). The cooling source was Gaussian in shape, with a radius of 1.5 km, and a depth of 4 km, centered 3.75 km above the surface. The cooling function for each experiment is shown in Figure 8 (a). A 6 min pulsing frequency was chosen because it was the shortest period for which distinct features remained resolvable in the outflow and because rainfall data frequently show surges with approximately this time scale.

The first two cycles of the pulsing experiment (12 min) essentially created the surface outflow. The cold air pulse created by the cooling cycle that peaked at 13.5 min can be followed as it falls into the pre-existing outflow and moves toward the front [Figure 8 (b)]. By 20 min, a distinct subfrontal feature has formed, and it is clear from the time evolution that it propagates relative to the surrounding current toward the front. By 22 min into the simulation, another sharpening pulse of cold air from the cooling maximum at 19.5 min can be seen beginning to move out into the current. Each pulse has a horizontal circulation associated with it that is less intense than, but in the same sense as the circulation associated with the gravity current front. By 26 min,
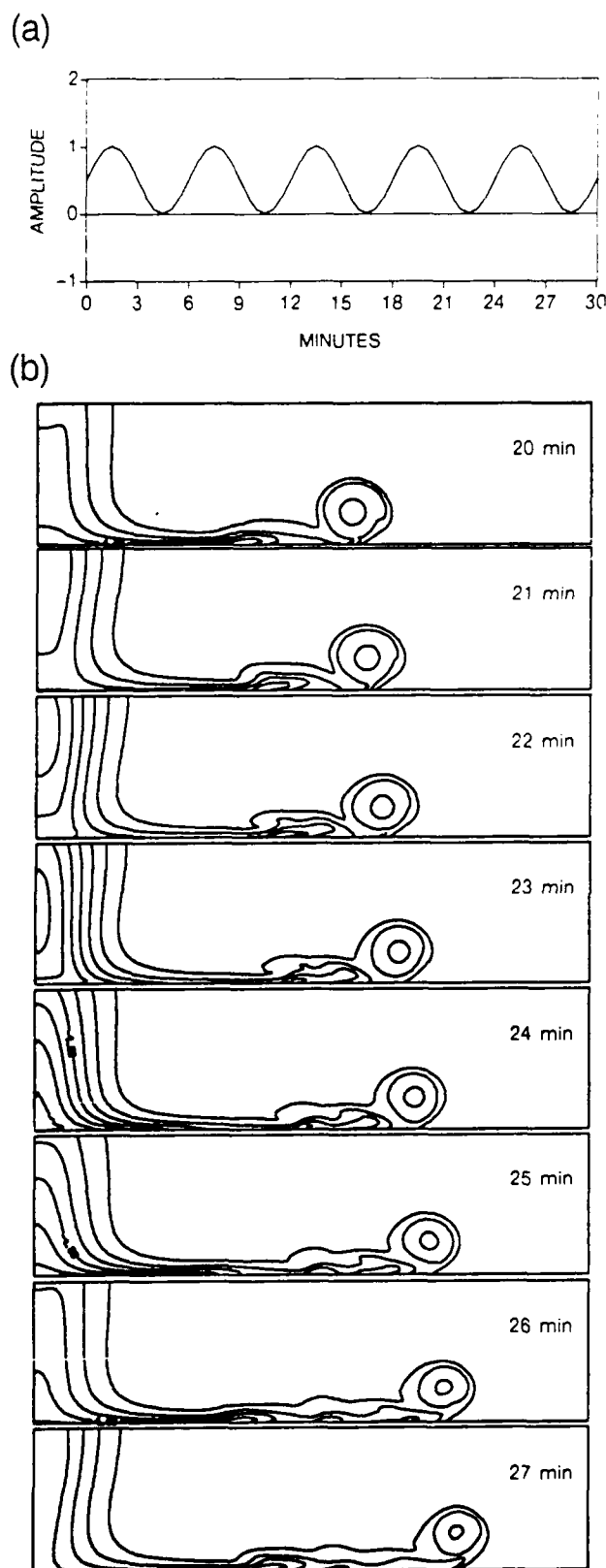
(a)

(b)

Figure 8 .   (a) The shape of the cooling function for pulsating flow rate experiment. Base cooling rate was –0.05 °C/s. (b) Flow resulting from pulsed forcing is shown every min from 20 to 27 min into the simulation. Potential temperature is contoured every 1 °C; coldest contour is –7 °C at 23 and 24 min. Domain shown is 12 km wide and 3 km high.

three distinct subfrontal features are indeed present in the outflow, but they are spaced at roughly 2 km intervals, and the nearest of them is roughly 4 km away from the downdraft. In the DFW observations, the vortices were next to the downdraft with a spacing of at most 0.5 km. Thus it appears that Fujita's hypothesis is untenable.

Wolfson (1990) has investigated the other hypotheses put forth to explain the observed vortices in the DFW data, and found none of them to be correct. Proctor (1988) showed that his numerical model of a single microburst thunderstorm could simulate some of the features in the DFW data, but it exhibited nothing resembling the rapid oscillations in the vertical velocity and temperature thought to be due to the "vortices". What, then, did cause the wind pattern encountered by Delta 191?

5.2.   A New Hypothesis

I suggest that Delta 191 actually encountered *two* thunderstorm outflows during the last 90 s of its flight. One storm was located 1 km west and 3.4 km north of runway 17L, and had a 2 km radius. The second storm was 6 min older, and was located 7.2 km north and 2.1 km east of the runway, and had a 4.75 km radius to the leading edge updraft. The embedded vortices encountered by Delta 191 were essentially an old gust front or "rotor" from this storm to the northeast. The hypothesized scenario is shown in Figure 9 .

To prove that this could indeed be the resolution of the "vortices" mystery, a numerical simulation was again performed with the help of Straka and Anderson. A neutral boundary layer axisymmetric model simulation was used for the older, distant storm (11 min simulation), and the same model with a 300 m deep stable layer, 4 K colder than the environment, was used to simulate the newer, closer storm (5 min simulation; see Figure 9). Otherwise, both models were identical with the following characteristics. The horizontal and vertical grid resolution was chosen to be 20 m. The time step was 0.1 s, the domain was 500 grid points wide by 350 high, and the eddy diffusion coefficient was 40 m^2/s. The environmental lapse rate of potential temperature was based on the profile of potential temperature measured by Delta 191. The cooling source was Gaussian in shape, with a radius of 1.0 km, and a depth of 4 km, centered at 3.5 km agl. The cooling rate was chosen so that the downdraft would be approximately 11 K colder than the neutral layer at the surface.

As can be seen in Figure 10 , the distant storm provides the oscillations in vertical velocity and temperature, and a sizable downdraft and increase in tailwind. The closer, younger storm provides the strong downdraft and tailwind, plus the crosswind blowing from west to east. The plotted dataset from Delta 191 ends at the last wind measurements, but the temperature was available for a short time afterward; it does increase just after 300 s in rough agreement with the numerical simulations.

Admittedly, not every wiggle is simulated through these two axisymmetric storm models at these times in these locations. However, a certain spatial compression and skewing of the wind features would be expected to result from the interaction of the two outflows. This comparison shows that the vortices encountered by Delta 191 were part of the actual wind pattern inside the gust front from an axisymmetric thunderstorm. In these early stages of thunderstorm out-

flow, the gust front portion of an outflow is at least as hazardous as the more laminar central downdraft.

The Stephenville radar 140 km away showed the DFW "cell" to have achieved VIP level 3 at least by 2256 GMT. By the time the accident occurred at 2305-2306, VIP level 4 was observed. I suggest both downdrafts encountered by Delta 191 came from this same radar cell; perhaps at higher resolution the individual cell components could have been identified. The same radar "cell" (different downdraft within) produced 35 m/s winds over the airport 20 min after the crash, indicating that it was indeed a multicell storm. The NSSL lightning detector observed a lightning strike about 15 min before the accident north-northeast of DFW. At this same time, observers also reported a cumulonimbus cloud north-northeast of the airport. Caracena et al. (1986) suggest that the outflow from a cell 20 km north-northeast of the airport contributed to the forcing for the DFW cell. This storm formed 20-30 min before the accident, and was visible on the Stephenville radar display. I think another, closer storm must have formed because of the observed strength of the vortices (gust front) and the cold temperature of the air. However, the evidence of older storms to the northeast clearly confirms the preferential development of new convection towards the southwest, triggered by old outflows.

Observations of the onboard weather radar of another flight airborne at the time of the crash indicated a "solid red contour (the highest contoured reflectivity) with no visible reflectivity gradients on a plan view scan. He notes having seen a green hook shaped echo (the lowest contoured reflectivity) protruding from a microburst cell over DFW airport seconds before another crew member sighted the fireball produced by Delta 191." (Caracena et al. 1986). This green thin line echo is the signature of a gust front, but it could not be the gust front from the new cell that Delta 191 encountered for two reasons. First, the gust front (leading vortex ring) would not have separated from that storm for another 2 min at least (refer to wind pattern of "new storm" in Figure 9), and second, even if the gust front had separated it would have been concentric with the cell, not "protruding". Yet this protruding gust front separated from its parent storm is exactly what would have been seen if something like the scenario in Figure 9 is correct. This provides additional support to the argument that Delta 191 encountered two outflows during its last 90 s of flight.

5.3.   Other Fatal U.S. Microburst Accidents

The next most recent microburst aircraft accident was the crash of Pan American Flight 759 at New Orleans International airport on July 9, 1982. Not nearly as much information is available on this crash; unambiguous recon-
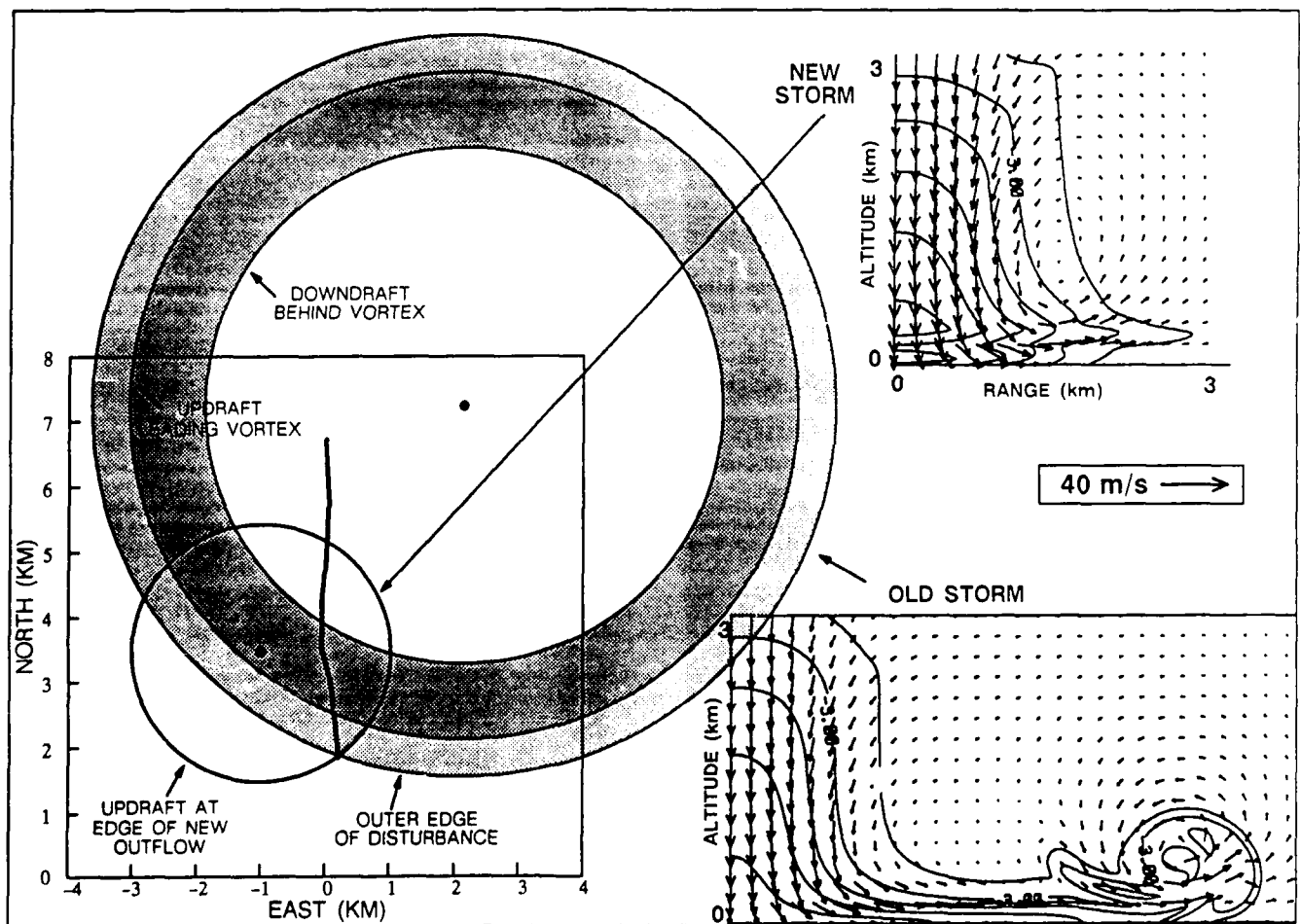

Figure 9 .   Proposed meteorological scenario during the crash of Delta 191 at DFW. The spots indicate thunderstorm downdraft centers. The thick black line represents the last 90 s of the Delta 191 flight. The north end of runway 17L is located at (0,0). Cross-sectional wind fields from the new and old storm are shown on the right. Potential temperature is contoured every 2°C from -1°C.
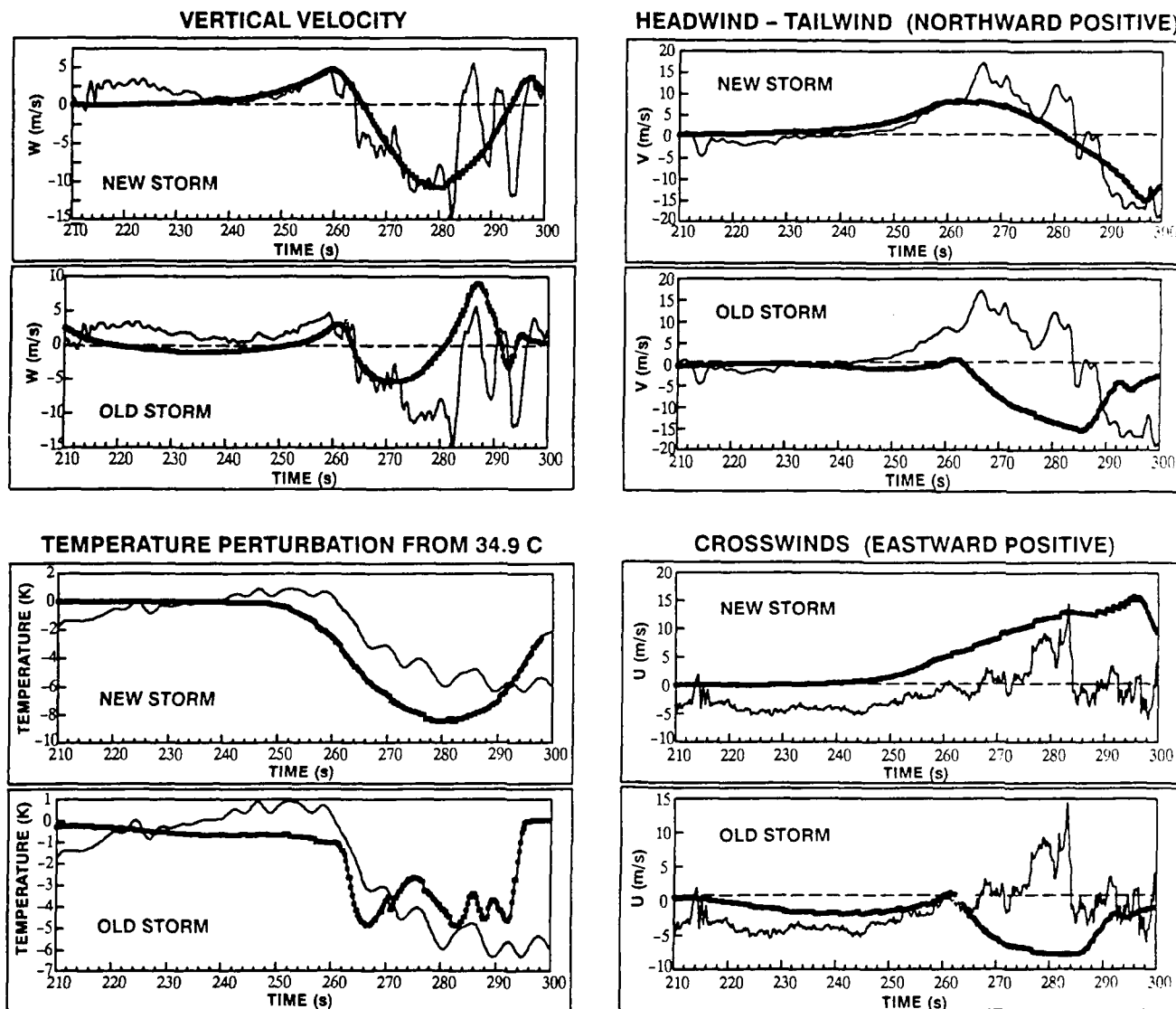
VERTICAL VELOCITY

HEADWIND – TAILWIND (NORTHWARD POSITIVE)

TEMPERATURE PERTURBATION FROM 34.9 C

CROSSWINDS (EASTWARD POSITIVE)

Figure 10 . Vertical velocity, north–south (headwind–tailwind) wind component, temperature perturbation, and east–west (crosswind) component from axisymmetric numerical model data (thick line), compared with Delta 191 data recovered by Wingrove and Bach (1987; thin line). For each variable, the top panel shows the model data from the closer, younger thunderstorm outflow, and the bottom panel shows the model data from the distant older outflow.

struction of the wind field was not possible. However, from Fujita's (1983) analysis, it is fairly definite that a newly formed thunderstorm downdraft and outflow occurred almost directly over the runway. It also appears that this downdraft landed just behind a gust front that had recently crossed the airport. The significance of encountering an old gust front just when the aircraft was emerging from the new downdraft is not known, but by analogy with the DFW case, this could well have contributed to the overall hazard.

Finally, we can reexamine the very first accident ever attributed to microburst wind shear, the crash of Eastern Flight 66 at JFK airport in New York on June 24, 1975. This was the accident that led to the development of the new burst terminology. Was this new downburst (later redefined as a microburst) anything other that a thunderstorm downdraft? I suggest that the presence of the sea breeze front made a fundamental difference on the evolution of the outflow pushing southward and eastward from scattered thunderstorms over the land. The winds from the sea breeze, perhaps augmented by the environmental winds, opposed the southward

advancement of the thunderstorm air. Along this boundary an arc cloud developed that was visible in the satellite imagery (Fujita 1976); this indicated convergence and an updraft strong enough to raise surface air to the condensation level. As in the other two microburst accidents, the thunderstorm downdraft landed just behind a gust front. In this case, the increased flow from two preceding downdrafts, in almost the same place as the third, accident-causing downdraft, added to the circulation about the leading edge of the outflow and probably enhanced the wind shear.

5.4. Summary

The hazardous low altitude wind shear events that have caused the fatal aircraft accidents attributed to microbursts were apparently the *combination* of a precipitation driven downdraft from a thunderstorm landing within the outflow of another thunderstorm, very near or essentially on top of the leading gust front. The "fresher" that gust front, the greater the aircraft hazard. In an isolated storm, the gust front has moved far enough from the main storm

downdraft by the time it has built into a strong horizontal vortex to physically separate the two hazardous regions. The most dangerous combination appears to include a strong downdraft about 2 min after reaching the surface, landing on top of the leading vortex of a circular gust front formed no more than about 10 min previously. In this way, the turbulent hazard of the gust front is brought into the same area as the performance decreasing downdraft and divergent wind shear of the precipitation driven thunderstorm downdraft.

6. CONCLUSIONS

The primary conclusion of this work is that the fatal aircraft accidents attributed to microbursts, including the first accident for which the microburst terminology was developed, all involved the *combination* of a precipitation driven downdraft and the narrow, low altitude downdraft and turbulent region associated with a gust front.

The first part of predicting microbursts, then, is predicting the strength of the precipitation driven thunderstorm downdraft. The second, previously unrecognized part of predicting microbursts involves tracking the gust fronts from older thunderstorm outflows. These often initiate new convection, so the possibility of a new downdraft forming along a gust front is not unlikely. The presence of a relatively fresh, turbulent gust front appears to greatly increase the aviation hazard of flying through a newly formed thunderstorm outflow.

REFERENCES

Addis, R.P., 1984: A numerical model of surface outflows from convective storms. *Boundary-Layer Meteor.*, 28, 121-160.

Anderson, J.R., 1990: Numerical simulation of thunderstorm microburst outflows. Submitted to *Mon. Wea. Rev.*

Biron, P.J., and M.A. Isaminger, 1989: An analysis of microburst characteristics related to automatic detection from Huntsville, AL and Denver, CO. Preprints, *24th Conference on Radar Meteorology*, Tallahassee, Amer. Meteor. Soc., 269-273.

Burrows, D.A., and L.F. Osborne, 1986: Precipitation loading in wet microbursts. Preprints, *23rd Conference on Radar Meteorology*, Snowmass, Amer. Meteor. Soc., J97-J100.

Caracena, F., R. Ortiz, J. Augustine, 1986: The crash of Delta Flight 191 at Dallas-Fort Worth International Airport on 2 August 1985: Multiscale analysis of weather conditions. *NOAA Tech. Rep. ERL 430-ESG 2*, 33pp.

Droegemeier, K.K. and M.R. Babcock, 1989: Numerical simulation of microburst downdrafts: Application to on-board and look-ahead sensor technology. *AIAA 27th Aerospace Sciences Meeting*, AIAA-89-0821, Reno, 12 pp.

Evans, J., and D. Turnbull, 1989: Development of an automated windshear detection system using Doppler weather radar. *Proc. IEEE*, 77, 1661-1673.

Fawbush, E.J., and R. C. Miller, 1954: A basis for forecasting peak wind gusts in non-frontal thunderstorms. *Bull. Amer. Meteor. Soc.*, 35, 14-19.

Frost, W., and R.L. Bowles, 1984: Wind shear terms in the equations of aircraft motion. *J. Aircraft*, 21, 866-872.

Fujita, T.T., 1976: Spearhead echo and downburst near the approach end of a John F. Kennedy airport runway, New York City. *SMRP Res. Pap. 137*, University of Chicago, Ill., 51 pp.

Fujita, T.T., 1983: Microburst wind shear at New Orleans International Airport, Kenner, Louisiana on July 9, 1982. *SMRP Res. Pap. 199*, University of Chicago, Ill., 39 pp.

Fujita, T.T., 1984: Andrews AFB microburst: Six minutes after the touchdown of Air Force One. *SMRP Res. Pap. 205*, University of Chicago, Ill., 38 pp.

Fujita, T.T., 1985: *The Downburst - Microburst and Macroburst*: Satellite and Mesometeorology Project, Department of the Geophysical Sciences, The University of Chicago, Ill., 122 pp.

Fujita, T.T., 1986: *DFW Microburst*. Satellite and Mesometeorology Project, Department of the Geophysical Sciences, The University of Chicago, Ill., 154 pp.

Fujita, T.T., and H. R. Byers, 1977: Spearhead echo and downburst in the crash of an airliner. *Mon. Wea. Rev.*, 105, 129-146

Garvine, R.W., 1984: Radial spreading of buoyant, surface plumes in coastal waters. *J. Geophys. Res.*, 89, No. C2, 1989-1996.

Goff, R.C., 1976: Vertical structure of thunderstorm outflows. *Mon. Wea. Rev.*, 104, 1429-1440.

Kingsmill, D.E., R.M. Wakimoto, and W.C. Lee, 1989: Kinematic and dynamic analysis of microburst producing thunderstorm. Preprints, *24th Conference on Radar Meteorology*, Tallahassee, Amer. Meteor. Soc., 146-149.

Knupp, K.R., 1987: Downdrafts within High Plains cumulonimbi. Part I. General kinematic structure. *J. Atmos. Sci.*, 44, 987-1008.

Krueger, S.K., and R.M. Wakimoto, 1985: Numerical simulation of dry microbursts. Preprints, *14th Conference on Severe Local Storms*, Indianapolis, Amer. Meteor. Soc., 163-166.

Laynor, W.G., 1986: Summary of windshear accidents and views about prevention. *Wind Shear - SAE SP-681*, No. 861697, 1-12

Linden, P.F., and J.E. Simpson, 1986: Gravity-driven flows in a turbulent fluid. *J. Fluid Mech.*, 172, 481-497.

Proctor, F.H., 1989: Numerical simulations of an isolated microburst Part II: Sensitivity experiments. *J. Atmos. Sci.*, 46, 2143-2165.

Rudich, R.D., 1986: Weather-involved U.S. air carrier accidents 1962-1984: A compendium and brief summary. *AIAA 24th Aerospace Sciences Meeting*, AIAA-86-0327, Reno, 7 pp.

Simpson, J.E., 1987: *Gravity Currents in the Environment and the Laboratory*. Ellis Horwood Ltd., 244 pp.

Smith, R.K., 1988: Travelling waves and bores in the lower atmosphere: The "Morning Glory" and related phenomena. *Earth-Sci. Rev.*, 25, 267-290.

Srivastava, R.C., 1985: A simple model of evaporatively driven downdraft: Application to a microburst downdraft. *J. Atmos. Sci.*, 42, 1004-1023.

Targ, R., and R.L. Bowles, 1988: Windshear avoidance: Requirements and proposed system for airborne lidar detection. *Airborne and Spaceborne Lasers for Terrestrial Geophysical Sensing, SPIE Vol. 889*, 54-64.

Wakimoto, R.M., and V.N. Bringi, 1988: Dual polarization observations of microbursts associated with intense convection: The 20 July storm during the MIST project. *Mon. Wea. Rev.*, 116, 1521-1539.

Wakimoto, R.M., C.J. Kessinger, and D.E. Kingsmill, 1989: Visual and dual-Doppler analysis of low-reflectivity microbursts. Preprints, *24th Conference on Radar Meteorology*, Tallahassee, Amer. Meteor. Soc., 77-80.

Wilson, J.W., R.D. Roberts, C. Kessinger, and J. McCarthy, 1984: Microburst wind structure and evaluation of Doppler radar for airport wind shear detection. *J. Climate Appl. Meteor.*, 23, 898-915

Wingrove, R.C., and R.E. Bach, 1987: Severe winds in the DFW microburst measured from two aircraft. *AIAA Guidance, Navigation and Control Conference*, AIAA-87-2340, 477-482

Wolfson, M.M., 1990: *Understanding and Predicting Microbursts*. Ph.D. thesis, Massachusetts Institute of Technology, 303 pp.

Zorpette, G., 1986: The menacing microburst. *IEEE Spectrum*, 23, 50-56.